# The influence of environment on galaxy formation

**Riccardo Brunino**

The University of Nottingham

Thesis submitted to the University of Nottingham
for the degree of Doctor of Philosophy, January 2012

**Supervisor:** Dr. Frazer Pearce

**Examiners:** Prof. Stefano Borgani
Dr. Simon Dye

# Abstract

The dynamical evolution of the matter content of the universe is modelled throughout this study as that of self and mutually gravitating Lagrangian fluids in the so called ΛCDM-*Concordance* cosmological framework which leads to the *Hierarchical Clustering* paradigm for the formation of cosmic structures. As a numerical tool for investigating galaxy formation scenarios in this context, we employed GADGET2 (see Springel 2005) and the more recent GADGET3 (see Springel *et al.* 2008): we describe the numerical solvers implemented in the code and test their behaviour in both gravitational and hydrodynamical setups of relevance for cosmological calculations (Tasker *et al.* 2008). Using the outputs of the MILLENNIUM simulation and the relative Semi Analytical galaxy catalogues produced by Croton *et al.* 2006, we developed an algorithm aimed at the identification of large spherical underdense regions in the simulated Large Scale Structure (LSS), at $z = 0$. Focusing on this peculiar environment, we found a confirmation in numerical simulations for the observations by Trujillo, Carretero & Patiri (2006). The Tidal Torque Theory can predict the spatial distribution of the orientation of both the angular momentum vector of Milky Way size galaxies located on the surface of large spherical *voids*, and of their host DM halos. We re–simulated the 5 GIMIC regions (Crain *et al.* 2009) following the gravitational evolution of the CDM component only. We then applied a Semi Analytical Model (SAM) of galaxy formation (De Lucia & Blaizot 2007) obtaining the galaxy catalogues and merger histories for the 5 different volumes simulated. It is not yet well understood if and how the LSS environment can influence the Star Formation (SF) histories of galaxies. Starting from the stellar mass content of semi–analytical galaxies at $z = 0$, we defined characteristic epochs for their build up and, as a preliminary study, investigated how these distribute as a function of different LSS environments.

# Acknowledgements

The author thanks Dr. Frazer Pearce for his constant supervision.
We would like to thank Volker Springel for providing us with GADGET3 and for fruitful discussions.
We would also like to thank the VIRGO CONSORTIUM for letting us take part in the GIMIC project by sharing the Initial Conditions.
Special thanks to Klaus Dolag for kindly sharing with us a (out-of-date) version of the suite of codes needed to produce merger trees.
Gabriella De Lucia is warmly thanked for accepting to use her SAM on our raw outputs. I would also like to thank her for the professional interest in this work, for the collaborative spirit and for enlightening discussions.
Just to mention a few, the author would like to thank:
Giuseppe Murante, Pierluigi Monaco, Rob Crain, Peter Coles, Franco Vazza and Claudio Gheller for useful discussions and support.

I would like to thank my family for inconditionate support.

# Acknowledgements 

I declare this thesis to be entirely my own work unless explicitly stated.

The contents of Chapter 3 were my contribution to a project that resulted in a refereed published work:

Tasker E.J., Brunino R., Mitchell N.L., Michelsen D., Hopton S., Pearce F.R., Bryan G.L., Theuns T., 2008. MNRAS, **390**, 1267. *A test suite for quantitative comparison of hydrodynamic codes in astrophysics.*

The contents of Chapter 4 have been published as two refereed works:

Brunino R., Trujillo I., Pearce F.R., Thomas P.A., 2007. MNRAS, **375**, 184. *The orientation of galaxy dark matter haloes around cosmic voids*

and

Colberg J.M., Pearce F., Foster C., Platen E., Brunino R., Neyrinck M., Basilakos S., Fairall A., Feldman H., Gottlober S., Hahn O., Hoyle F., Muller V., Nelson L., Plionis M., Porciani C., Shandarin S., Vogeley M.S., van de Weygaert R., 2008. MNRAS, **387**, 933. *The Aspen-Amsterdam void finder comparison project.*

# Contents

**List of Figures** **v**

**List of Tables** **ix**

**The influence of Environment on Galaxy Formation**

**1 Theoretical Framework** **2**

1.1 Standard Cosmological Model . . . . . 2

1.2 Standard paradigm of structure formation . . . . . 5

1.2.1 More about the hierarchical clustering model . . . . . 6

1.3 Dynamical features . . . . . 7

1.3.1 Dark Matter . . . . . 7

1.3.2 Intra Cluster Medium . . . . . 9

1.4 Linear Jeans theory . . . . . 10

1.5 Thesis Outline . . . . . 13

**2 Numerical Algorithms** **14**

2.1 Gravity Calculation . . . . . 15

2.1.1 Direct Summation . . . . . 17

2.1.2 Oct-Tree . . . . . 17

2.1.3 Particle Mesh . . . . . 19

2.1.4 GADGET2 . . . . . 20

2.2 SPH . . . . . 21

2.2.1 GADGET2-SPH . . . . . 25

2.3 Time integration . . . . . 28

**3 Testing the solvers** **31**

3.1 Sod shock tube test . . . . . 32

3.1.1 ICs . . . 33
3.1.2 Runs and Results . . . 35
3.2 Sedov test . . . 42
3.2.1 Sedov setup . . . 42
3.2.2 Sedov Results . . . 43
3.3 King halos . . . 54
3.3.1 Initial conditions . . . 55
3.3.2 The static King halo . . . 56
3.3.3 The translating King halo . . . 57
3.4 Comparison . . . 59

**4 Orientation of Halos around voids 61**
4.1 Abstract . . . 61
4.2 Introduction . . . 62
4.3 Numerical simulation . . . 65
4.3.1 N–body simulation . . . 65
4.3.2 Void and halo samples . . . 66
4.3.3 Void finder comparison . . . 67
4.3.4 Halo shapes and spins . . . 69
4.4 Results . . . 71
4.5 Discussion . . . 76

**5 GIMIC and SAMs 79**
5.1 The GIMIC spheres . . . 80
5.1.1 Initial conditions and numerical calculations . . . 81
5.1.2 Post Processing . . . 83
5.2 SAM model . . . 87
5.2.1 General physics . . . 87
5.2.2 Galaxy Mergers . . . 90
5.3 Preliminary Results . . . 91
5.4 Summary and Discussion . . . 100

**6 Conclusions 102**
6.1 Test suite . . . 103
6.2 Orientation . . . 104

6.3 GIMIC . . . . . 105
6.4 Perspectives . . . . . 107

**Appendices**

**A SPH: smoothing kernel and sphere** **109**

**Bibliography** **111**

# List of Figures


2.1 2-Dimensional representation of Barnes and Hut oct-tree, from Springel 2005 . . . . . 18

3.1 Sod shock test initial conditions. . . . . 33

3.2 Small glass: Gaussian fit of the distribution function of the nearest neighbour separations for all the particles in the computational volume at an early stage of *glass* generation. . . . . 34

3.3 Small glass: Gaussian fit of the distribution function of the nearest neighbour separations for all the particles in the computational volume at a later stage of *glass* generation. Comparing with the above figure it is possible to see that the system is lead towards an equilibrium configuration that maximises the inter-particle separation. . . . . 34

3.4 [1,0,0] setup: the black line is the theoretical solution, green is the $250,000$ particle setup, red is the $10^6$ particle setup. Analysis has been performed in a direction orthogonal to the initial contact interface (i.e. the *x*-axis in this case), for the chosen end–state $t = 0.12$. . . . . 37

3.5 Increased viscosity, [1,0,0] setup: the black line is the theoretical solution, green is the $250,000$ particle setup, red is the $10^6$ particle setup. Analysis has been performed in a direction orthogonal to the initial contact interface (i.e. the *x*-axis in this case), the chosen and-state $t = 0.12$ . . . . . 39

3.6 Increased viscosity, [1,1,1] setup: the black line is the theoretical solution, green is the $250,000$ particle setup, red is the $10^6$ particle setup. Analysis has been performed in a direction orthogonal to the initial contact interface (i.e. along the diagonal of the cubic computational box, in this case) for $t = 0.12$ . . . . . 41

3.7 Radially binned profiles (green lines) produced considering 500 radial bins, logarithmically spaced. The black lines show the theoretical Sedov solution at this time (t=0.1). . . . . 44

3.8 Sedov, 32 particle, spherical top-hat energy injection: column density projection map along the z-axis, for all particles in the box at $t = 0.1$. 45

3.9 Sedov: projection along the z - axis of particles in a slab through the center of the box (one mean interparticle separation thick) for different setups. . . . . 47

3.10 Density: radially binned density profiles for different setups. Blue lines are the corresponding RMS in each bin. . . . . 48

3.11 Pressure: radially binned pressure profiles for different setups. Blue lines are the corresponding RMS in each bin. . . . . 48

3.12 Velocity: radially binned profiles of the radial velocity component, in different setups. Blue lines are the corresponding RMS in each bin. . . 49

3.13 Energy: internal energy for all particles in the shock region. The formation of an overly energetic *plume* of particles is clearly visible. . . . 49

3.14 Entropy: computational entropy (Equation 3.1) for all particles close to the shock front. . . . . 50

3.15 Projection along the z-axis of the position of particles located in a slab, through the center of the box, of thickness comparable to the average SPH smoothing length. Over energetic particles are marked in yellow. 52

3.16 Reproducing the Sedov test discussed in Springel & Hernquist 2002, we obtain the correct answer. . . . . 54

3.17 Treecode result for the static King sphere. Left to right, radially binned profiles for density, temperature and computational entropy are shown. The black lines are the initial $t = 0$ values, while the red lines represent the profiles after 1 Gyr. . . . . 56

3.18 PM result for the static King sphere. Left to right, radially binned profiles for density, temperature and computational entropy are shown. The black lines are the initial $t = 0$ values, while the red lines represent the profiles after 1 Gyr. . . . . 56

3.19 King translating - TreePM. Left to right, the radial profiles for density, temperature and entropy are shown. Black lines represent the status of the King halo at $t = 0$, while red lines represent the final status. . . . . 58

3.20 Image subtractions of the density projections at the start and end of the translating cluster test, The projected density range is $[10^4, 10^{18.6}]\,\mathrm{M}_\odot$ $\mathrm{Mpc}^{-2}$. . . . . 58

4.1 A slice of thickness $5\,h^{-1}\,\mathrm{Mpc}$ through the centre of the region extracted from the Millennium simulation. The image shows the dark matter distribution in the central $40\,h^{-1}\,\mathrm{Mpc}$ region. Void galaxies (within any void, not just the largest one) are superimposed on the dark matter distribution as blue circles. The locations of the largest void (with dark matter particles inside the void marked green), its centre (red circle), and all void galaxies found. . . . . 68

4.2 Radially averaged dark matter density profiles of the largest void in each of the void catalogues found by the groups involved in the study of Colberg *et al.* 2008. For each void finder the profile extends out to the largest radius that can be studied, given the size of the volume. See main text for more details. . . . . 69

4.3 Space density of galaxies ($h^3$/Mpc$^3$/mag) as a function of dust corrected $M_B$ for galaxies in the volume under consideration and in the catalogues of those void finders which identify galaxies inside voids. For purposes of comparison, the luminosity function of the full simulation volume is also given. Each void finder luminosity function is corrected for the volume occupied by the relevant void sample. . . . . 70

4.4 Distributions of the local densities of the galaxies in the results of those void finders that identity void galaxies. The local density is expressed via $r_{14}$, which for each galaxy gives the radius of the sphere around the galaxy that contains $10^{14}\,h^{-1}\,\mathrm{M}_{\odot}$. For comparison purposes, the distribution of the full galaxy sample is also shown. . . . . 70

4.5 Probability density distribution of the cosine of the angles $\theta$ between the inertia axes (and angular momentum) and the vector joining the centre of the voids with the halo centres. The error bars on each bin is the Poissonian error and (to avoid confusion) are only plotted for the innermost shell bins. The null hypothesis (i.e. a sine distribution) is represented by the dashed line. . . . . 74

4.6 Same than in Fig. 4.5 but this time using only haloes which contain a disc–dominated galaxy at their centres. Note that using this halo subsample the angular momentum vector tends to lie parallel to the surface of the void. . . . . 75

5.1 The evolution of overdensity in the five spherical regions at intermediate resolution . . . . . 84

5.2 Schematic organisation of the merger tree in the Millennium Run. At each output time, FOF groups are identified which contain one or several (sub)halos. The merger tree connects these halos. The FOF groups play no direct role, except that the largest halo in a given FOF group is the one which may develop a cooling flow according to the physical model for galaxy formation implemented for the trees. To facilitate the latter, a number of pointers for each halo are defined. Each halo knows its descendant, and its most massive progenitor. Possible further progenitors can be retrieved by following the chain of 'next progenitors'. In a similar fashion, all halos in a given FOF group are linked together. Figure taken from Springel *et al.* 2005 . . . . . 86

5.3 Differential number density of halos as a function of mass at $z = 0$, normalized by the total enclosed mass of each region and multiplied by $M^2$ to reduce the dynamic range of the plot. . . . . 87

5.4 Galaxy merger tree. In this example, the merger tree of a Galaxy of Type 0 is shown: at $z = 0$ its stellar content sums up to $\simeq 1.27 \times 10^{11} M_{\odot}$ and this galaxy is central in a DM halo of $\simeq 2.74 \times 10^{13} M_{\odot}$. Colors: *black* is for T0 galaxies, *green* or T1 and *red* is for T2 Symbols: symbol size is proportional to the stellar content of the represented object. 92

5.5 Stellar mass content differential distribution function at $z = 0$. Clockwise from top left, the overall sample of galaxies containing more than $5 \times 10^8 M_\odot$ in the stellar component, the Type 0, Type1 and Type2 corresponding distributions. Lines are color coded black to cyan for growing overdensities . . . . . 94

5.6 CDFs for the *Infall* redshift for all T1 and T2 galaxies with $M_{st}^{z=0} \gtrsim 5 \times 10^8 M_\odot$ in the 5 GIMIC high resolution regions . . . . . 96

5.7 CDFs for *Formation* (left column) and *Assembly* (right column) redshifts, for the entire galaxy population (i.e. all galaxies with $M_{st}^{z=0} \gtrsim 5 \times 10^8 M_\odot$) in each high-resolution GIMIC region, considering the three galaxy types. For each GIMIC sphere, the corresponding number of galaxies is also indicated in the plot. Color coding as in Figure 5.3: *black* to *cyan* growing region overdensity . . . . . 97

5.8 CDFs for *Formation* (left column) and *Assembly* (right column) redshifts for Type 0 galaxies in the 5 GIMIC regions. Here, the overall sample has been divided in three bins in $M_{st}^{z=0}$, as indicated in each panel. The color coding of the curves goes from black to cyan for growing overdensities. The number of objects in each subsample is also shown. . . . . 99

# List of Tables

3.1 Sod shock setup parameters. . . . . 35

4.1 The strength of the alignments on the different shells. To measure the alignment of the inertia axes we have used the parameter p (p=1 in the null case), and c (Lee 2004) in the case of the angular momentum (c=0 in the null case). . . . . 75

5.1 Parameters for the five GIMIC regions. Columns 2-5 give the location (in Millennium Simulation coordinates) and the nominal comoving radius of the regions at $z = 1.5$. The following column show the number of dark matter particles within the zoomed region of the simulation.Adapted from Crain *et al.* (2009). . . . . 82

# The influence of Environment on Galaxy Formation

# Chapter 1

# Cosmological Framework

## 1.1 Standard Cosmological Model

Hubble's observation of the linear distance-velocity relation for galaxies came after the work of Friedmann, whose model had already foreseen the non-static nature of a Universe that obeys the Cosmological Principle and General Relativity (hereafter GR). Einstein's theory of gravitation generalizes the fundamental ideas of *Special Relativity*: starting from the assumption of the invariance of the speed of light $c$ under Lorentz transformation, Einstein also realized that it was necessary to

- abandon the idea of a gravitational potential related to the distribution of matter and whose gradient gives the gravitational field at any point;
- assume that our four-dimensional space-time is curved by the presence of matter;
- impose that free-falling objects describe geodesics in space-time.

These considerations lead to GR theory, in which gravitation is not formulated as a force or a field but as a curvature of a 4-D space-time sourced by matter. All isolated systems (i.e. bodies in free-fall and light rays) follow geodesics which are bent by space-time curvature. In other words their trajectories are affected by the distribution of matter around them. This is *phenomenologically* what gravity means.

By geometrical considerations it is possible to see that a suitable metric for such a Universe is that introduced by Friedmann-Lemaitre-Robertson-Walker (hereafter FLRW):

$$ds^2 = c^2dt^2 - a^2(t)\left[\frac{dr^2}{1-kr^2} + r^2(d\theta^2 + sin^2\theta d\phi^2)\right] \tag{1.1}$$

in which the square root of the term in square brackets represents the *physical* distance between two points (say *dl*), whereas $(r, \theta, \phi)$ are polar and *comoving*.

Consider Einstein's equation:

$$G_{ik} = R_{ik} - \frac{1}{2}g_{ik}R = \frac{8\pi G}{c^4}T_{ik} \tag{1.2}$$

with the symbols having their usual meanings, and assume an homogeneous and isotropic perfect fluid, choosing for the energy-momentum tensor the expression:

$$T_{ik} = (p + \rho c^2)U_iU_k - pg_{ik} \tag{1.3}$$

Solving this equation with the FLRW metric leads to:

$$\left(\frac{\dot{a}}{a}\right)^2 = \frac{8\pi G}{3}\rho + \frac{kc^2}{a^2} \tag{1.4}$$

$$\frac{\ddot{a}}{a} = -\frac{4\pi G}{3}(\rho + 3p). \tag{1.5}$$

Known as the Friedmann equations, they describe the time dependence of the expansion factor and can be looked as, respectively, an energy conservation and a sort of second law of Newtonian dynamics. Historically, in order to avoid an expanding universe Einstein added to his equation a constant term $\Lambda$, but after the observations of Hubble this *artifact* disappeared. Eventually this term reappeared in modern cosmology, where it is given a very peculiar and important meaning because it seems to account for current observational evidence indicating the expansion rate of the Universe.

As outlined above by looking at the FLRW metric, we see that objects in free-fall follow geodesics in space-time. Referring to GR, and thinking of galaxies as non relativistic objects, their motion is described by $dl \simeq 0$ and so the comoving distance does not change during the expansion. This shows that it is the behaviour of the scale factor ($a(t)$ in 1.1) that drives the observed flow of galaxies. Identifying $H$ with $\dot{a}/a$ we have theoretically reproduced the velocity field observed by Hubble, and obeyed the

Cosmological Principle. *Photons* also move along geodesics. In detail, their motion can be described by:

$$ds^2 = 0 \tag{1.6}$$

which means:

$$c^2dt^2 = dl^2 = a^2(t)\left[\frac{dr^2}{1-kr^2} + r^2(d\theta^2 + \sin^2\theta d\phi^2)\right] \tag{1.7}$$

which is the infinitesimal equation of motion that has to be integrated to get the distance travelled by a photon in a given time interval. Choosing a photon with constant ($\theta$,$\phi$) coordinates, that travels between $t_1$ and $t_2$, its change in comoving coordinates is given by:

$$\int_{r_1}^{r_2} \frac{dr}{\sqrt{1-kr^2}} = \int_{t_1}^{t_2} \frac{c}{a(t)}dt \tag{1.8}$$

which is called the *equation of propagation of light*.

In order to fully characterize the perfect fluid we have assumed, we also need an equation of state. Usually this is written:

$$p = w\rho c^2 \tag{1.9}$$

where the parameter *w*, describing the kind of perfect fluid, is chosen in the *Zel'dovic interval*: $0 < w < 1$. It can be easily shown that any universe with this kind of equation of state, which is a solution of the Friedmann equations, will present an initial singularity at $t = 0$ where the expansion parameter $a(t = 0) = 0$ and the density $\rho$ diverges. This initial unavoidable event is called the *Big Bang* and is a peculiar feature of the Standard Cosmological Model here outlined.

An important quantity that must be introduced is the *critical density*: the FLRW metric of equation (1.1) reduces to the Euclidean metric of a *flat* space-time taking $k = 0$. Considering equation (1.6) with this choice for $k$, and solving for $\rho$, gives the critical density:

$$\rho_c(t) = \frac{3c^2H^2(t)}{8\pi G} \tag{1.10}$$

that obviously depends on time, and nowadays takes the value

$$\rho_{0c} = 1.9 \times 10^{-29} \quad h^2 \quad g \quad cm^{-3} \tag{1.11}$$

A density larger than this would mean that our universe is *closed* (geometrically this corresponds to $k = 1$); on the other hand a lower density would be characteristic of an

*open* universe ($k = -1$). In the literature the value of the density with respect to the critical one is expressed by a parameter

$$\Omega(t) = \frac{\rho(t)}{\rho_c(t)} \tag{1.12}$$

In order to understand the geometrical shape of our universe and its future it is necessary to know the amount of *matter* and *energy* contained in it. By relating the equation of state (equation 1.9), referring to the value of the parameter *w* and constraining the expansion to be adiabatic it is possible to see that:

- for pressureless matter $w = 0$ and $\rho_m(a) \propto a^{-3}$
- for radiation $w = \frac{1}{3}$ and $\rho_r(a) \propto a^{-4}$

Going back in time, i.e. to smaller values of *a*, and looking at $\rho_m$ and $\rho_r$, there must have been an epoch in which the two densities coincided, named *the equivalence* period ($\tau_{eq}$), before which it was radiation that dominated the expansion, and after which the matter became predominant ($\tau_{eq}$ when $\rho_{DM}(\tau_{eq}) = \rho_{rad}(\tau_{eq})$).

In this framework is set another pillar of the Standard Cosmological Model: the *Big Bang Nucleosynthesis* (hereafter BBN). This model has undergone many observational tests that have confirmed all its prescriptions for the abundances of light elements in the universe.

## 1.2 Standard paradigm of structure formation

Clusters of galaxies are the largest virialized structures in the universe. There are many peculiar properties that make them very interesting from a cosmological point of view. It is possible to outline a widely accepted scenario for cosmic structure formation as follows:

- The Universe appears to be dominated by non baryonic *Dark Matter* (DM) that doesn't interact with radiation and seems to be collisionless. Recently, in order to account for observational evidence regarding the global expansion of our universe, additional models have been proposed for what is called *Dark Energy* that seems to drive the expansion on very large scales.

- The amount of baryonic matter is that predicted by Big Bang Nucleosynthesis and contributes about $1/6^{th}$ of the total amount of matter. Somewhat less than $10\%$ of this resides in the form of stars, galaxies and condensed material, the rest being diffuse.

- At the epoch of hydrogen recombination the universe could be considered homogeneous and isotropic on sufficiently large scales. Below this threshold there were small inhomogeneities, generated by quantum effects during an inflationary stage soon after the initial singularity. These fluctuations constitute a random *Gaussian* field. In this framework their is no characteristic scale for structure formation.

- These seeds grow by *gravitational instability*, and their evolution after recombination is driven by the gravity of the DM: the earliest structures formed are DM halos.

- Galaxies formed later when baryons collapsed dissipatively in the dark matter potential wells.

The model that best describes these views is that of *hierarchical clustering*, based on the assumption that non-relativistic Cold Dark Matter drives the process and that the density fluctuation spectrum was such that small structures were preferred. Hierarchically larger (more massive) structures formed by coalescence and merging of smaller ones.

### 1.2.1 More about the hierarchical clustering model

After equality ($\tau_{eq}$), the dark matter fluid (collisionless, without electromagnetic interactions and non relativistic) had a vanishing pressure. As a consequence it could concentrate in gravitational wells, deepen the potential and also amplify the perturbations. Being a causal mechanism it could operate only inside the Hubble radius so, even today, the Fourier Spectrum of CDM perturbations has a characteristic scale corresponding to the Hubble radius at "matter-radiation equality" . Problems in the determination of this quantity arise because soon the process lost linearity and what we

can observe are non linear structures: numerical simulations are required to make predictions. During the radiation dominated era the CDM perturbations inside the Hubble radius could not grow. Smaller wavelengths (looking at the Fourier spectrum) entered the Hubble radius first. As they entered earlier than longer wavelengths they were the first to be amplified and the first that became non linear. The smallest structures in the universe are therefore the oldest ones. As progressively smaller and smaller wavenumbers entered the horizon later, so perturbations on larger scales reached non-linearity at later times.

## 1.3 Dynamical features

The formation process of galaxy clusters is essentially driven by gravity. Hydrodynamical forces, radiative cooling, star formation, energy feedback and thermal conduction involve only the baryonic component and so have a smaller effect on the evolution. Observations indicate that galaxy clusters are younger than their hosted galaxies so they retain much more information about the cosmological parameters involved: their mass and abundance are very sensitive to the amplitude $\sigma_8$ of the power spectrum of primordial fluctuations $P(k)$ and to the density parameter $\Omega_0$. The formation epoch $z_{form}$ and evolutionary properties are almost exclusively connected with $\sigma_8$. Galaxy clusters have been successfully used to map the density and velocity fields of matter in the universe. In order to analyse the dynamical and kinematical properties of clusters of galaxies (to put constraints on cosmological parameters) it is necessary to distinguish between different constituents as we will now describe.

### 1.3.1 Dark Matter

Dark matter dominates the gravitational field of galaxy clusters. As such they can be considered as collisionless systems to a first approximation: the motion of each DM particle is determined by the mean gravitational field of the system because two-body interactions are negligible. Through the non-collisional Boltzmann equation (Vlasov equation) a full description of the dynamics of a collisionless system can be described. Solving this equation is very difficult and usually its momenta with respect to velocity

are taken:

- The zero order moment gives the continuity equation
- The first order moment gives the conservation of momentum: Jeans equation

This last relation describes the interplay between the gravitational potential gradient and the density and velocity fields of the system. A spherical, symmetric and static system has a radial gravitational potential gradient proportional to the ratio

$$M(< r)/r^2.$$

Isolating the mass inside $r$, the Jeans equation can be written :

$$M(< r) = -\frac{r\sigma_r^2(r)}{G}\left[\frac{d\log\rho}{d\log r} + \frac{d\log\sigma_r^2}{d\log r} + 2\beta(r)\right] \tag{1.13}$$

where $M(< r)$ is the total mass that generates the potential well, and $\beta(r)$ represents the anisotropy parameter of the velocity field:

$$\beta(r) = 1 - \frac{\sigma_t^2(r)}{\sigma_r^2(r)} \tag{1.14}$$

and the *local* quantities $\rho(r)$, $\sigma_t^2(r)$, $\sigma_r^2(r)$, $\beta(r)$ refer to any distribution of points in dynamical equilibrium within the potential($\sigma_t$ and $\sigma_r$ are, respectively, the tangential and the radial component of the velocity dispersion). The spatial and dynamical distribution of such a tracer must satisfy the Jeans equation in order to give the right *total mass* of the system.

Multiplying equation (1.13) by the radial coordinate $r$ and integrating over the whole space returns the *virial* theorem:

$$\langle v^2\rangle = \frac{GM}{r}. \tag{1.15}$$

If the virial theorem is applied to a finite region of radius $r_0$ (e.g. the central region of a cluster), the range of integration is modified and an additional term of superficial pressure ($\propto \rho(r_0)$) must be added. Forgetting this manipulation leads to an underestimation of the total mass. A rich galaxy cluster can have a total mass that exceeds $10^{15}M_\odot$. The amount of baryonic matter is a few times $10^{14}M_\odot$ and consists of two main components: hundreds of galaxies and a diffuse hot intracluster plasma (ICM). This second component is several times more massive than the whole galactic contribution.

### 1.3.2 Intra Cluster Medium

This is the collisional component: a hot plasma with a mass several times that of the galaxies ($M_{ICM} \simeq 10^{14} M_{\odot}$). If this gas is in thermodynamical equilibrium within the potential well of the cluster it must be completely ionized with a temperature of $\approx 10^8$K. Therefore galaxy clusters are strong X-ray sources of free-free emission, with typical luminosity $L_x \approx 10^{45}$ erg $s^{-1}$. The dynamical status of a collisional gas is described by the equation of hydrostatic equilibrium. Under the assumption of a static and spherically symmetric potential this equation is equivalent to the Jeans equation (1.13). Substituting the velocity dispersion term with the virial temperature: $kT/\mu m_p = \sigma^2$ and taking a zero velocity field anisotropy $\beta = 0$ (i.e. the isotropy is due to collisions) the hydrostatic equilibrium equation is written:

$$M(< r) = -\frac{rkT(r)}{G\mu m_p}\left[\frac{d\log\rho}{d\log r} + \frac{d\log T(r)}{d\log r}\right]. \tag{1.16}$$

The predictions of simulations for this component agree with observations. From recent, high resolution simulations it emerges that:

- The ICM distribution follows the DM density profile, but has a wider spatial distribution. This is an effect of the collisional nature of this component: during gas inflow into DM potential wells, an angular momentum and energy transfer takes place from the DM to the ICM. This mechanism results in a baryon fraction increasing with the radius.

- The ICM gas is supported by its thermal pressure and not by its velocity dispersion. Merging with substructures can slightly modify the situation but thermal pressure still dominates.

- The ICM distribution is, to first order, isothermal. Actually temperature decreases in the outer regions and at the virial radius it is a factor of 2 lower than in the center.

## 1.4 Linear Jeans theory

In the framework of the standard cosmological model, the cosmic structures we observe formed by gravitational amplification of primordial density fluctuations. To a first approximation, the early universe can be considered as a perfect, Newtonian, self-gravitating fluid. The behaviour of this system is described by the following equations:

conservation of mass (i.e. the *continuity* equation)

$$\frac{\partial \rho}{\partial t} + \vec{\nabla}(\rho \vec{v}) = 0; \tag{1.17}$$

conservation of momentum (i.e. *Euler's* equation)

$$\frac{\partial \vec{v}}{\partial t} + (\vec{v} \cdot \vec{\nabla})\vec{v} = -\frac{1}{\rho}\vec{\nabla} p - \vec{\nabla}\Phi; \tag{1.18}$$

together with an equation relating the gravitational potential $\Phi$ to its source (i.e. *Poisson's* equation) :

$$\nabla^2 \Phi = 4\pi G \rho; \tag{1.19}$$

an equation of state for the fluid (relating pressure,density and entropy, S)

$$p = p(\rho, S) \tag{1.20}$$

and finally an equation describing the temporal evolution of entropy. This last equation is simplified by assuming that we are only dealing with adiabatic systems:

$$\frac{dS}{dt} = 0 \tag{1.21}$$

For such a system the equation of state is also simplified:

$$p = p(\rho, S) \longrightarrow p = p(\rho). \tag{1.22}$$

The system of these equations admits the static solution of a homogeneous and isotropic

universe characterized by :

$$\rho = \rho_b = const \tag{1.23}$$

$$p = p_b = const \tag{1.24}$$

$$\vec{v} = 0 \tag{1.25}$$

$$\Phi = \Phi_b = const \tag{1.26}$$

$$S = const. \tag{1.27}$$

It should be noted that such a solution cannot be consistent: the Poisson equation does not work with a constant gravitational potential if $\rho \neq 0$. This can be seen as an undesirable consequence of a Newtonian description of a static and infinite universe. It is anyway useful to consider this unperturbed solution and to apply first order perturbation theory to study the evolution of such a system. The perturbed solution in an expanding universe (Einstein-de Sitter) has the following form in physical coordinates:

$$\rho = \rho_b(1+\delta) \tag{1.28}$$

$$p = p_b + \delta p_b \tag{1.29}$$

$$\vec{u} = H\vec{r} + \vec{v} \tag{1.30}$$

$$\Phi = \Phi_b + \phi \tag{1.31}$$

$$\tag{1.32}$$

where $\vec{u}$ includes the contribution of both an Hubble expansion term and of the *peculiar* velocity of the object and the density perturbation $\rho_b\delta \equiv \delta\rho$ is the source of the gravitational potential perturbation $\phi$. Consider a universe dominated by matter and inside the horizon; inserting these perturbed quantities into the set of equations (1.17 to 1.22) in physical coordinates and manipulating them to obtain the comoving expressions gives the system of three equations that describes the fluid behaviour:

$$\frac{\partial}{\partial t}\delta\rho + \frac{\rho_b}{a}\vec{\nabla}\vec{v} + 3H\delta\rho = 0 \tag{1.33}$$

$$\frac{\partial}{\partial t}\vec{v} + H\vec{v} = -\frac{v_s^2}{a}\vec{\nabla}\delta - \frac{\vec{\nabla}\phi}{a} \tag{1.34}$$

$$\frac{\nabla^2\phi}{a} = 4\pi G\rho_b\delta. \tag{1.35}$$

In order to simplify one moves to Fourier space and imposes plane wave solutions of the form:

$$f(\vec{x},t) = f_k(t)\exp(i\vec{k}\vec{x}) \tag{1.36}$$

where $\vec{x}$ is the comoving coordinate and $k = 2\pi/\lambda_{com}$. Referring to the density field perturbation it takes the shape:

$$\delta\rho = \delta\rho_k \exp(i\omega t) \tag{1.37}$$

and rewriting the dynamical equations:

$$\dot{\delta} + \frac{i\vec{k}\vec{v}_k}{a} = 0 \tag{1.38}$$

$$\dot{\vec{v_k}} + \frac{\dot{a}}{a}\vec{v}_k = -\frac{i\vec{k}}{a}(v_s^2\delta_k + \phi_k) \tag{1.39}$$

$$\phi_k = \frac{4\pi G\rho_b\delta_k a^2}{k^2} \tag{1.40}$$

it is possible to reduce the whole system description to a single differential equation in $\delta_k$. It can be shown that, for all perturbations, only the component parallel to the wave vector $\vec{k}$ is significant in the time evolution. The equation obtained is:

$$\ddot{\delta}_k + 2\frac{\dot{a}}{a}\dot{\delta}_k + \delta_k\left[\frac{k^2v_s^2}{a^2} - 4\pi G\rho_b\right] = 0 \tag{1.41}$$

Looking at the terms inside square brackets, the value assumed by the quantity

$$\lambda_J = \frac{2\pi}{k_J} = v_s a\left(\frac{\pi}{G\rho_b}\right)^{\frac{1}{2}} \tag{1.42}$$

allows a distinction between two kinds of solutions:

- $\lambda < \lambda_J$ gives two oscillating solutions (the pressure term dominates);
- $\lambda > \lambda_J$ are solutions with gravitational instability (gravity term dominates).

The explicit solution in the case of instability represents the growth of a density perturbation (i.e. the amplification of an initial fluctuation in the density field). Everything holds for a matter dominated universe (i.e. after the *time of equivalence*$= \tau_{eq}$) and until: $\delta \ll 1$. Looking at $\tau < \tau_{eq}$ means looking at a radiation dominated universe containing different species. The general relativistic derivation of the evolutionary

equation for a density perturbation in a matter-radiation fluid leads to a differential equation similar to equation (1.41):

$$\ddot{\delta}_k + 2\frac{\dot{a}}{a}\dot{\delta}_k + \delta_k \left[ k^2 v_s - \frac{32}{3}\pi G \rho_b \right] = 0 \tag{1.43}$$

where $k$ is now the physical wavelength and the factor $32/3$ accounts for all the possible sources of the potential well (relativistic pressure contribution). From these equations it is possible to predict the evolution of a *linear* density perturbation at any epoch and for any wavelength.

## 1.5 Thesis Outline

The remainder of this thesis is laid out as follows: in Chapter 2 I introduce the numerical algorithms I have used to complete the work described here. In Chapter 3 I describe some of the numerical testing I undertook in order to establish the accuracy of these numerical methods. In Chapter 4 I introduce a method for identifying a particular environment in the Large Scale Structure, galaxy voids, and examine the alignment of DM halos near these large underdense structures. In Chapter 5 I introduce a set of numerical models and use them to examine the dependence of galaxy formation on the larger scale environment. Finally, I conclude and make some suggestions for further work in Chapter 6.

# Chapter 2

# Numerical algorithms

Computational modelling of the formation and evolution of Large Scale Structure (hereafter LSS) in the Universe has traditionally been tackled as the modelling of the time evolution of a set of self gravitating fluids, either collisional (ideal gas hydrodynamics) or non-collisional (dark matter), within a volume expanding according to a preferred cosmological model.

Numerical models adopt two main approaches to the description of the kinematics of a fluid element:

- **Eulerian**: the motion of a fluid element is described with respect to an external (to the fluid) system of reference such as a fixed mesh, resulting in the spatial discretization of the continuum.
- **Lagrangian**: the motion of a fluid element is described with respect to the fluid element itself, for example sampling the fluid properties with tracers (such as particles), thus resorting to a discretization in mass of the continuum.

Both these traditional approaches have found their way into modern computational techniques, each of them presenting a number of benefits and unavoidable drawbacks (see Dolag *et al.* (2008) for a review). Here we are focusing on the Lagrangian approach, such as the one implemented in the widely disseminated GADGET2 code (Springel 2005).

To calculate the dynamical evolution of a self gravitating collisional fluid, it is necessary to calculate the resulting net force acting on each individual Lagrangian particle:

$$F = F_{grav} + F_{hydro} \tag{2.1}$$

The gravitational and the hydrodynamical contributions are calculated by means of very different algorithms.

## 2.1 Gravity calculation

For the most part of the life of the Universe, the formation and evolution of the LSS can be modelled by following the dynamics of a non-collisional, non-relativistic, self gravitating fluid (namely "Cold Dark Matter", CDM) in an expanding background space. A Lagrangian representation of this fluid resorts to *particles*, which can be thought as a finite sampling of CDM phase-space density.

The dynamics of these Lagrangian elements can then be derived by solving the *N-boby* problem for a system of particles having mass $m$, position $\vec{x}$ and momentum $\vec{p}$, and living in a Universe whose expansion is described by a scale factor $a = (1+z)^{-1}$ (where z is the redshift).

The continuum limit of such a discretization is described by the non-collisional Boltzmann equation (or Vlasov equation), assuming a phase space distribution function $f(\vec{x}, \vec{p}, t)$ :

$$\frac{\partial f}{\partial t} + \frac{\vec{p}}{ma^2}\vec{\nabla} f - m\vec{\nabla}\Phi\frac{\partial f}{\partial \vec{p}} = 0 \tag{2.2}$$

which needs to be coupled to the Poisson equation for the gravitational potential:

$$\vec{\nabla}^2\Phi(\vec{x}, t) = 4\pi \mathrm{G} a^2 \left[\rho(\vec{x}, t) - \bar{\rho}(t)\right] \tag{2.3}$$

where $\Phi$ is the *peculiar* gravitational potential and $\bar{\rho}(t)$ is the background density.
In other words, the description of the dynamics of this system of particles is given by the Hamiltonian:

$$H = \sum_i \frac{\vec{p}_i^2}{2\, m_i\, a(t)^2} + \frac{1}{2}\sum_{ij} \frac{m_i m_j\, \varphi(\vec{x}_i - \vec{x}_j)}{a(t)} \tag{2.4}$$

where $H = H(\vec{p}_1, \ldots, \vec{p}_N, \vec{x}_1, \ldots, \vec{x}_N, t)$ and the canonical momenta can be expressed as $\vec{p}_i = a^2 m_i \dot{\vec{x}}_i$.

In our discrete Lagrangian approach, the peculiar potential at position $\vec{x}$ can be written as:

$$\phi(\vec{x}) = \sum_i m_i \, \varphi(\vec{x} - \vec{x}_i) \tag{2.5}$$

Let's consider a Newtonian gravitational potential of the form given in equation (2.5), for a system of two point masses. The potential at the position of particle $i$ (relative position) due to particle $j$, is:

$$\phi(x_i) = -\frac{G m_j}{x_i - x_j} \tag{2.6}$$

which diverges for particle j at zero separation from particle i. In order to avoid this, and also to prevent spurious two body relaxations (Steinmetz & White 1997), a comoving *softening* length, $\epsilon$, is usually introduced, such that the expression given in equation (2.6) becomes:

$$\phi(x_i) = -\frac{G m_j}{[(x_i - x_j)^2 + \epsilon^2]^{\frac{1}{2}}} \tag{2.7}$$

which becomes equivalent to that of a Plummer sphere of size $\epsilon$, for null particle separations. The softening value is typically chosen to be roughly $1/40^{th}$ of the mean interparticle separation in the computational box (Power *et al.* 2003). Once the peculiar gravitational potential, at the particles positions, is known, it is then possible to describe the dynamics of the system by means of the comoving equations of motion (for each particle):

$$\frac{\mathrm{d}\vec{p}}{\mathrm{d}t} = -m\vec{\nabla}\Phi \tag{2.8}$$

and

$$\frac{\mathrm{d}\vec{x}}{\mathrm{d}t} = \frac{\vec{p}}{ma^2}. \tag{2.9}$$

which can be combined, once the peculiar velocity $\vec{v} = a\dot{\vec{x}}$ is introduced:

$$\frac{\mathrm{d}\vec{v}}{\mathrm{d}t} + \vec{v}\frac{\dot{a}}{a} = -\frac{\vec{\nabla}\Phi}{a}. \tag{2.10}$$

Different algorithmic choices are available for computing the gravitational potential of a large number of Lagrangian particles, such as the ones involved in a cosmological calculation.

### 2.1.1 Direct summation

In a Lagrangian representation of a self gravitating fluid, the most direct way of calculating the value of the gravitational potential at a particle position is given by:

$$\Phi(\vec{r}) = -\mathrm{G}\sum_{j}\frac{m_j}{\left(|\vec{r}-\vec{r}_j|^2+\epsilon^2\right)^{\frac{1}{2}}} \tag{2.11}$$

which provides as a solution of the N-Body problem the exact Newtonian potential. In this formulation it is possible to note the presence of the gravitational softening term $\epsilon$, already discussed in equation (2.7). In order to perform this accurate calculation of the potential, this algorithm needs to compute a sum over all particles for each individual particle. This results in a calculation scaling $\propto N^2$, where N is the number of particles, therefore bearing a very high computational cost for large numbers of fluid tracers. In cosmological calculations of galaxy formation the number of particles needed for sampling the fluid's phase space is typically very large and, furthermore, reasonable approximations of the exact Newtonian potential can be tolerated: thus *direct summation* is not used in cosmological simulations.

### 2.1.2 Multipole expansion: the oct-tree method

In order to overcome the $N^2$ bottleneck of direct summation, a widely used approach involves the use of a *multipole* expansion of the gravitational potential.

Despite the Universe being homogenous and isotropic on sufficiently large scales, the evolution of the LSS leads to an highly clustered matter distribution on scales well below the horizon. Gravity is a long range force and, in principle, the total gravitational potential evaluated at a particle's position should take into account the contribution from all the particles in the simulation box, as in the *direct summation* method. The clustered distribution of matter on the scales typical of the LSS, allows for a *multipole* approximation to be taken: the contribution to the *local* gravitational potential provided by a group of particles (a *clump*) which is sufficiently small and distant can be safely approximated as that of a *macro-particle* positioned at the center of mass of that distant matter clump. In other words, if the distant particles clump is seen, by the particle under consideration, to subtend a small enough angle, a multipole approximation of

the gravitational potential of such a matter distribution can be taken as the contribution to the local gravitational potential.

This approach is implemented by the so called *tree* algorithms, out of which the most commonly adopted in cosmological codes is the Barnes-Hut tree, as it was first introduced by Barnes & Hut (1986). This is an iterative method also known as an *oct-tree*: the whole computational box (of linear size $L$, called the *root*) is bisected through its center in all three spacial directions, resulting in eight smaller cubes of linear size $L/2$. At each successive iteration, each of these smaller cubes is divided into eight again and the algorithm continues to iterate until a level is reached in which the cubes are either empty or contain single particles (called the *leaves*). So, all *leaves* contain information about an individual particle while, at the upper levels toward the *root*, collective information for groups of particles are stored in the tree *nodes*. In order to evaluate the

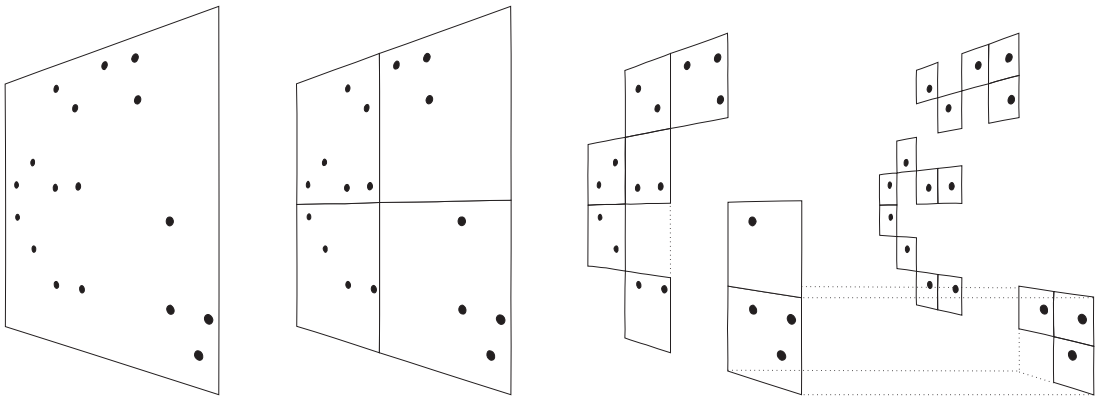

**Figure 2.1:** 2-Dimensional representation of Barnes and Hut oct-tree, from Springel 2005

gravitational potential at each particle position, the *tree* needs to be walked: starting at the root level, it is asked if a node's angular dimension, as seen from the particle position, is smaller than a fixed value (the *opening angle*). If this condition is met, the multipole approximation of the potential contributed by particles stored within that node can be taken. In the node's angular dimension is bigger than the opening angle, then it is opened and its branches are walked until another node meets the geometrical criterion, or the leaves are reached.

Building such a tree is not computationally expensive, while walking the tree takes a considerable computational time: nevertheless, estimating the gravitational poten-

tial using this algorithm requires on the order of $Nlog(N)$ operations, thus proving computationally efficient with respect to the direct summation approach.

In the oct-tree algorithm presented by Barnes & Hut (1986), the opening angle was defined with a geometrical criterion:

$$\alpha \approx \frac{d}{l} \tag{2.12}$$

where $d$ is the linear dimension of the node of interest and $l$ the distance from the current particle position.

### 2.1.3 Potential on a mesh: the PM method

In the Particle-Mesh approach, the gravitational potential is assumed to be a *field-quantity* and it is calculated on a computational mesh. These algorithms start by transferring the Lagrangian mass distribution onto a 3-dimensional mesh. This is done by smoothing particles' densities on the mesh. Once the mass distribution is loaded onto the mesh, the gravitational potential $\Phi$ can be calculated, in Cartesian coordinates, by convolving the mass density with a suitable Green's function $g(\vec{x})$:

$$\Phi(\vec{x}) = \int g(\vec{x} - \vec{x}')\rho(\vec{x}')\mathrm{d}\vec{x}'. \tag{2.13}$$

It is possible to show that, by choosing

$$g(\vec{x}) = -\mathrm{G}/|\vec{x}| \tag{2.14}$$

and moving to Fourier space, the Poisson equation ( 2.3) becomes a simple multiplication:

$$\hat{\Phi}(\vec{k}) = \hat{g}(\vec{k})\,\hat{\rho}(\vec{k}). \tag{2.15}$$

The Fourier transforms are fast to perform thanks to the widely used fast FFTW algorithms (see *www.fftw.org*), and the Green's function $\hat{g}(\vec{k})$ needs to be computed only once when the cubic mesh is initialized at the beginning of the simulation. Once the potential is obtained at the mesh points, the corresponding force can be calculated differentiating the potential. A final interpolation of the forces, from the mesh points back

to the particle positions, allows for the equation of motion of each Lagrangian particle to be solved.

This class of force calculation algorithms, typically employ on the order of $Nlog(N)$ operations to reach the solution, with $N$ being the number of mesh points. It is worth mentioning that the most relevant limitation of this method resides in its approximate handling of highly clustered distributions of particles: when a single mesh cell is filled with a large amount of Lagrangian tracers the force resolution obtained is poor. In order to overcome this shortcoming of the method, a very large mesh should be used (large $N$), at the price of reducing the computational efficiency of the fast Fourier transform algorithms.

### 2.1.4 GADGET2 gravity calculation

In GADGET2, the gravity calculation is performed with the hybrid *TreePM* approach. Following Springel (2005), the gravitational potential can be split in Fourier space such that

$$\Phi_{\vec{k}} = \Phi_{\vec{k}}^{\rm long} + \Phi_{\vec{k}}^{\rm short} \tag{2.16}$$

where

$$\Phi_{\vec{k}}^{\rm long} = \Phi_{\vec{k}} \exp(-\vec{k}^2 r_{\rm s}^2) \tag{2.17}$$

with $r_{\rm s}$ being the physical scale for the force-split. The long-range component of the potential ($PM$) is then calculated on a mesh, by means of FFT methods in a very efficient and accurate way. It is possible to obtain an expression for the short-range part of the potential, exploiting the fact that, for $r_{\rm s} \ll L$ with L being the box size, the short-range solution of the Poisson equation ( 2.3) in real space is given by:

$$\Phi^{\rm short}(\vec{x}) = -G \sum_i \frac{m_i}{\vec{r}_i} {\rm erfc}\left(\frac{\vec{r}_i}{2r_{\rm s}}\right). \tag{2.18}$$

which also provides a cutoff at short range for the $PM$ estimate of the gravitational potential and an *upper* limit (i.e. a long range cutoff) for the tree calculation of the potential. With this implementation, the tree needs to be walked only for a small spatial region of size $r_{\rm s} \ll L$ around each particle. Using this hybrid method, a very accurate estimate of the long range force is obtained while keeping the main advantages of tree algorithms and overcoming the resolution issues of the $PM$ approach.

In GADGET2, the adopted tree algorithm is very similar to the one presented in section (2.1.2) with the choice of considering only the monopole in the multipole expansion of the potential of a tree node. The estimate thus provided is less accurate with respect of a choice that takes into account higher multipole orders, but this is compensated by the limited range of the tree calculation and by the considerable gain in computational efficiency.

The criterion adopted in GADGET2 for walking the tree and making a decision on when a node needs to be opened or not, is not purely geometrical as the one presented in equation (2.12). Walking the tree, a node of mass $M$, linear size $l$, at distance $r$ from the particle under consideration, is considered for usage if:

$$\frac{GM}{r^2}\left(\frac{l}{r}\right)^2 \leq \alpha\,|\vec{a}| \tag{2.19}$$

where $|\vec{a}|$ is the size of the total acceleration obtained in the last timestep, and $\alpha$ is a tolerance parameter. In this criterion the dynamical state of the simulation is taken into account: the idea is to limit the absolute force error, introduced by the monopole approximation of the particle-node interaction, by a comparison of an estimate of the truncation error with the total expected force.

In the $PM$ part, the smoothing of the density onto the mesh and the force interpolation from the mesh points back onto the particle positions is done using the CIC (Cloud In Cell) approximation, which is a common choice for this kind of $PM$ algorithm.

## 2.2 Hydrodynamical calculation

Within the gravitational framework outlined in the previous sections (and also in 1.4), cosmological codes that include hydrodynamics also need to follow the time evolution of the baryonic matter in the universe. This is modelled as a self gravitating fluid whose gravity is described as in the CDM case (i.e. it is assumed to be safe to calculate $\vec{\nabla}\Phi$ as outlined in the previous section).

This baryonic ideal fluid, mainly composed by hydrogen end helium, undergoes collisional dynamics and in order to follow its evolution a set of hydrodynamical equations

needs to be solved. The *continuity* equation :

$$\frac{\mathrm{d}\rho}{\mathrm{d}t} + \rho\vec{\nabla}\vec{v} = 0 \tag{2.20}$$

describes the conservation of mass, while the *Euler* equation:

$$\frac{\mathrm{d}\vec{v}}{\mathrm{d}t} = -\frac{\vec{\nabla}P}{\rho} - \vec{\nabla}\Phi \tag{2.21}$$

describes the conservation of momentum, and the *first law* of thermodynamics:

$$\frac{\mathrm{d}u}{\mathrm{d}t} = -\frac{P}{\rho}\vec{\nabla}\cdot\vec{v} \tag{2.22}$$

describes the conservation of energy for a non radiative (i.e. adiabatic) fluid.

This set of equations needs to be *closed* by an equation that relates the pressure $P$ with the internal energy per unit mass $u$ of the ideal gas element. Assuming an ideal monoatomic gas, with adiabatic index $\gamma = 5/3$, the *equation of state* provides the required closure of the set of hydrodynamical equations:

$$P = (\gamma - 1)\rho u \tag{2.23}$$

As in the calculation of the gravitational potential, the hydrodynamical evolution of the ideal fluid needs to be expressed in an expanding background. This leads to the following form for the equation of hydrodynamics :

$$\frac{\partial\rho}{\partial t} + \frac{3\dot{a}}{a}\rho + \frac{1}{a}\vec{\nabla}\cdot(\rho\vec{v}) = 0 \tag{2.24}$$

$$\frac{\partial\vec{v}}{\partial t} + \frac{1}{a}(\vec{v}\cdot\vec{\nabla})\vec{v} + \frac{\dot{a}}{a}\vec{v} = -\frac{1}{a\rho}\vec{\nabla}P - \frac{1}{a}\vec{\nabla}\Phi, \tag{2.25}$$

$$\frac{\partial}{\partial t}(\rho u) + \frac{1}{a}\vec{v}\cdot\vec{\nabla}(\rho u) = -(\rho u + P)\left(\frac{1}{a}\vec{\nabla}\cdot\vec{v} + 3\frac{\dot{a}}{a}\right) \tag{2.26}$$

respectively, in which $a$ is the *scale factor* for the expansion of the Universe.

One Lagrangian approach to the solution of the hydrodynamical equations for an ideal fluid is called Smoothed Particle Hydrodynamics (hereafter SPH): in this technique, the Lagrangian fluid element is represented by a particle (all particles share the same mass value) and physical quantities characterizing its behaviour are obtained by a spatial smoothing with a kernel function over a finite adaptive volume. In other words,

physical quantities pertaining to a Lagrangian element of the fluid are convolved with a kernel function (e.g. a Gaussian or a spline window function) rather than a Dirac $\delta$ function centered at the particle position.

Following Monaghan (1992) and starting with the general expression for the smoothing of a quantity $A$ with a window function $W$:

$$\langle A(\vec{x})\rangle = \int W(\vec{x}-\vec{x}',h)A(\vec{x}')\mathrm{d}\vec{x}' \tag{2.27}$$

a normalization for the kernel function needs to be imposed, such that $\int W(\vec{x},h)\mathrm{d}\vec{x} = 1$ and $W(\vec{x},h) \to \delta_{Dirac}(\vec{x})$ for $h \to 0$. The characteristic parameter for the smoothing $h$ is called the *smoothing length*.

Moving from the continuum to the Lagrangian discretization represented by a set of $j$ particles (with equal mass $m_j$, and positions $\vec{x}_j$) it is possible to write for the $i$-th particle:

$$\langle A_i\rangle = \langle A(\vec{x}_i)\rangle = \sum_j \frac{m_j}{\rho_j} A_j W(\vec{x}_i - \vec{x}_j, h)\,, \tag{2.28}$$

in which the volume element for the integration in 2.27 is replaced by the particle based volume estimate $m_j/\rho_j$. It is also useful to calculate the spatial derivative of equation (2.28):

$$\vec{\nabla}\langle A_i\rangle = \sum_j \frac{m_j}{\rho_j} A_j \vec{\nabla}_i W(\vec{x}_i - \vec{x}_j, h), \tag{2.29}$$

where $\vec{\nabla}_i$ is the derivative taken along $\vec{x}_i$. It is possible to show that this derivative can also be expressed in the following pair-wise symmetric formulation:

$$\vec{\nabla}\langle A_i\rangle = \frac{1}{\rho_i}\sum_j m_j(A_j - A_i)\vec{\nabla}_i W(\vec{x}_i - \vec{x}_j, h). \tag{2.30}$$

which can also be rewritten in the useful form:

$$\vec{\nabla}\langle A_i\rangle = \rho_i \sum_j m_j \left(\frac{A_j}{\rho_j^2} + \frac{A_i}{\rho_i^2}\right)\vec{\nabla}_i W(\vec{x}_i - \vec{x}_j, h). \tag{2.31}$$

In general, if a kernel with compact support is adopted (i.e. $W(\vec{x},h)=0$ for $|\vec{x}|>h$), the sums over $j$ in the previous equations are limited to the particles lying in a sphere of radius $h$ centered on the $i$-th particle (i.e. its *neighbours*) (see Appendix A).

The kernel smoothed expression of the density of particle $i$, can then be obtained by replacing $A$=$\rho$:

$$\langle\rho_i\rangle = \sum_j m_j W(\vec{x}_i - \vec{x}_j, h), \tag{2.32}$$

which can be interpreted as the density estimate for particle $i$.

This Lagrangian approach inherently conserves mass (i.e. the continuity equation (2.20) is automatically fulfilled) and making use of the above formalism, the Euler equation (2.21) takes the form:

$$\frac{\mathrm{d}\vec{v}_i}{\mathrm{d}t} = -\sum_j m_j \left(\frac{P_j}{\rho_j^2} + \frac{P_i}{\rho_i^2} + \Pi_{ij}\right) \vec{\nabla}_i W(\vec{x}_i - \vec{x}_j, h). \tag{2.33}$$

The time variation of the mass–weighted internal energy of a particle (i.e. the first law of thermodynamics) can be expressed as:

$$\frac{\mathrm{d}u_i}{\mathrm{d}t} = \frac{1}{2}\sum_j m_j \left(\frac{P_j}{\rho_j^2} + \frac{P_i}{\rho_i^2} + \Pi_{ij}\right) (\vec{v}_j - \vec{v}_i)\, \vec{\nabla}_i W(\vec{x}_i - \vec{x}_j, h). \tag{2.34}$$

It has been shown by several authors (Hernquist & Katz 1989, for example) that taking the *geometric* mean, instead of the *arithmetic* mean, inside the pair-wise symmetric derivative leads to more stable numerical results. With this choice, equations (2.33) and (2.34) take the form:

$$\frac{\mathrm{d}\vec{v}_i}{\mathrm{d}t} = -\sum_{j=1}^{N} m_j \left(2\frac{\sqrt{P_i P_j}}{\rho_i \rho_j} + \Pi_{ij}\right) \nabla_i \overline{W}_{ij}\,. \tag{2.35}$$

and

$$\frac{\mathrm{d}u_i}{\mathrm{d}t} = \frac{1}{2}\sum_{j=1}^{N} m_j \left(2\frac{\sqrt{P_i P_j}}{\rho_i \rho_j} + \Pi_{ij}\right) (\vec{v}_j - \vec{v}_i)\cdot \nabla_i \overline{W}_{ij}\,, \tag{2.36}$$

In equations (2.35) and (2.36), the smoothing kernel has also been symmetrized, with respect to the pair-wise smoothing lengths: $\overline{W}_{ij} = W(|\vec{r}_{ij}|, [h_i + h_j]/2)$, which is a common choice.

In the SPH formulation of the hydrodynamical equations (equations 2.33 and 2.34, or 2.35 and 2.36), it is necessary to introduce an *artificial viscosity* term $\Pi_{ij}$: this is

necessary in order to follow the behaviour of a dissipative flow, which is able to identify sudden and steep density gradients such as shocks. This approximation presents several drawbacks, limiting by construction the predictive power of SPH in some situations.

The main advantage of such a Lagrangian approach resides in the fact that SPH is able to naturally follow a wide dynamical range of densities, providing at no cost a very high spatial resolution in overdense regions (i.e. more particles are placed in such places) making the overall scheme efficient in coping with the extreme dynamical ranges involved in numerical studies of galaxy formation.

### 2.2.1 SPH implementation in GADGET2

Following Springel (2005) and looking at equations ( 2.35) and ( 2.36), it is possible to point out that there is actually not any absolute need to distribute the pressure equally between a particle pair. It has been shown that, if the SPH estimate for the local velocity divergence is used in order to derive the energy equation, the following formulation can be obtained (see equation 2.36):

$$\frac{\mathrm{d}u_i}{\mathrm{d}t} = \sum_{j=1}^{N} m_j \left( \frac{P_i}{\rho_i^2} + \frac{1}{2}\Pi_{ij} \right) \vec{v}_{ij} \cdot \nabla_i \overline{W}_{ij} \,. \tag{2.37}$$

which has been shown to conserve energy just as well, while producing less scatter in entropy, as pointed out by Couchman, Thomas & Pearce (1995a).

The GADGET2 formulation of SPH introduces a more fundamental change in the overall numerical scheme by implementing a formulation of SPH in terms of the dynamical equations for the specific entropy rather than specific internal energy (Lucy, 1977; Benz, 1987; Hernquist, 1993). The specific entropy $s$ of a fluid element can be characterized in terms of an entropic function $A(s)$:

$$P = A(s)\rho^{\gamma} \tag{2.38}$$

where $\gamma$ is the adiabatic index, and this equation of state resembles that of a generic polytrope. Using equation (2.38) together with the equation of state of an ideal fluid (equation 2.23), the internal energy per unit mass can be expressed by

$$u = \frac{A(s)}{\gamma - 1}\rho^{\gamma - 1} \tag{2.39}$$

Rather than following the evolution of each particle's internal energy, it is possible to integrate the time variation of the entropic function $A(s)$. It is immediately obvious that for an inviscid fluid in a laminar regime:

$$\frac{\mathrm{d}A}{\mathrm{d}t} = 0. \tag{2.40}$$

As mentioned above, moving away from the inviscid fluid approximation requires the introduction of an *artificial viscosity* in SPH: shocks cause the entropic function $A(s)$ to vary with time even in the absence of other sources or sinks of entropy. For example, a suitable SPH discretization of equation (2.40) for a dissipative fluid is given by

$$\frac{\mathrm{d}A_i}{\mathrm{d}t} = \frac{1}{2}\frac{\gamma-1}{\rho_i^{\gamma-1}} \sum_{j=1}^{N} m_j \Pi_{ij} \vec{v}_{ij} \cdot \nabla_i \overline{W}_{ij}\,, \tag{2.41}$$

which shows that entropy is *only* generated by the artificial viscosity in shocks, for a dissipative fluid in the adiabatic approximation. This equation (2.41) is integrated in the GADGET2 implementation of SPH, in order to follow the thermodynamical evolution of a fluid element: this approach offers the possibility of tight control of each particles' specific entropy, guaranteeing that it can only grow in time in the adiabatic regime. In order to follow the dynamical evolution of an SPH particle, Springel & Hernquist (2002) show that it is possible to derive, from a discretized form of the Lagrangian of the fluid, an equation of motion for SPH particles that takes the form:

$$\frac{\mathrm{d}\vec{v}_i}{\mathrm{d}t} = -\sum_{j=1}^{N} m_j \left[ f_i \frac{P_i}{\rho_i^2} \nabla_i W_{ij}(h_i) + f_j \frac{P_j}{\rho_j^2} \nabla_i W_{ij}(h_j) \right], \tag{2.42}$$

where the coefficients $f_i$ are defined by

$$f_i = \left[ 1 + \frac{h_i}{3\rho_i} \frac{\partial \rho_i}{\partial h_i} \right]^{-1}, \tag{2.43}$$

and the abbreviation $W_{ij}(h) = W(|\vec{r}_i - \vec{r}_j|, h)$ has been used.

In order take into account entropy generation by microphysical processes in shocks, a corrective viscous force is also taken into account:

$$\left.\frac{\mathrm{d}\vec{v}_i}{\mathrm{d}t}\right|_{\mathrm{visc}} = -\sum_{j=1}^{N} m_j \Pi_{ij} \nabla_i \overline{W}_{ij}\,, \tag{2.44}$$

with $\Pi_{ij} \geq 0$ is non-zero only when particles approach each other in physical space.

The form for the artificial viscosity $\Pi_{ij}$ adopted by GADGET2 is a modified version of the widely employed parametrization introduced by Gingold & Monaghan (1983) and by Balsara (1995), that reads:

$$\Pi_{ij} = \begin{cases} \left[-\alpha c_{ij}\mu_{ij} + \beta\mu_{ij}^2\right]/\rho_{ij} & \text{if } \vec{v}_{ij}\cdot\vec{r}_{ij} < 0 \\ 0 & \text{otherwise,} \end{cases} \tag{2.45}$$

where

$$\mu_{ij} = \frac{h_{ij}\,\vec{v}_{ij}\cdot\vec{r}_{ij}}{|\vec{r}_{ij}|^2}. \tag{2.46}$$

Here $h_{ij}$ and $\rho_{ij}$ are the arithmetic means of the corresponding quantities for the two particles $i$ and $j$, with $c_{ij}$ giving the mean sound speed. The strength of the viscosity is regulated by the parameters $\alpha$ and $\beta$, with typical values in the range $\alpha \simeq 0.5 - 1.0$ and the common choice of $\beta = 2\,\alpha$.

In GADGET2, following Monaghan (1997), the notion of *signal velocity*, $v_{ij}^{\rm sig}$, between two particles is introduced. This leads to a modified form for the artificial viscosity:

$$\Pi_{ij} = -\frac{\alpha}{2} w_{ij} v_{ij}^{\rm sig}/\rho_{ij} \tag{2.47}$$

while a simple form for the signal velocity can expressed as

$$v_{ij}^{\rm sig} = c_i + c_j - 3w_{ij} \tag{2.48}$$

where $w_{ij} = \vec{v}_{ij}\cdot\vec{r}_{ij}/|\vec{r}_{ij}|$ is the relative velocity of the two particles projected onto the separation vector, for particles approaching each other (i.e. for $\vec{v}_{ij}\cdot\vec{r}_{ij} < 0$), $w_{ij} = 0$ otherwise. This leads to an explicit formulation of the viscosity parametrization implemented in GADGET2:

$$\Pi_{ij} = -\frac{\alpha}{2}\frac{\left[c_i + c_j - 3w_{ij}\right] w_{ij}}{\rho_{ij}} \tag{2.49}$$

Springel (2005) also notes that the effect of this viscosity parametrization in the equation of motion is analogous to an excess pressure of the form:

$$P_{\rm visc} \simeq \frac{\alpha}{2}\gamma\left[\frac{w_{ij}}{c_{ij}} + \frac{3}{2}\left(\frac{w_{ij}}{c_{ij}}\right)^2\right] P_{\rm therm} \tag{2.50}$$

that depends only on a Mach-number like quantity $w/c$, and not explicitly on the particle separation or smoothing length as in the standard Balsara parametrization ($P_{\rm visc} \simeq \frac{1}{2}\rho_{ij}^2\Pi_{ij}$)

## 2.3 Time evolution

The accuracy in the time evolution of a fluid, described by the Hamiltonian in equation (2.4), strongly depends on both the time step size and the integration scheme chosen to advance in time the solution of an equation of motion like equation (2.10).

The choice of the time step size is non trivial, but the simple criterion often used is

$$\Delta t = \alpha\sqrt{\epsilon/|\vec{a}|} \tag{2.51}$$

which takes into account the dynamical state of the system, being $|a|$ the acceleration obtained at the previous time step, $\epsilon$ a length scale (typically linked to the gravitational softening) and $\alpha$ a tolerance parameter. In order to update in time the characteristic dynamical variables of a particle, first order ordinary differential equations (ODEs) like equation (2.8) and equation (2.9) need to be solved . There are many *explicit* or *implicit* (iterative) solvers that suite this need, among which a frequent choice is the so called *leap-frog* integrator in which the first order derivatives are shifted in time by $\Delta(t)/2$ with respect to the corresponding position or momentum.

Following Springel (2005) and Quinn *et al.* (1997), it is worth noticing that for an N-body system:

$$H = H_{\rm kin} + H_{\rm pot} \tag{2.52}$$

like in equation (2.4) and that each of the two contributions can be computed exactly. This allows us to define the following *drift* and *kick* operators:

$$D_t(\Delta t) : \begin{cases} \vec{p}_i & \mapsto & \vec{p}_i \\ \vec{x}_i & \mapsto & \vec{x}_i + \frac{\vec{p}_i}{m_i}\int_t^{t+\Delta t}\frac{\mathrm{d}t}{a^2} \end{cases} \tag{2.53}$$

$$K_t(\Delta t) : \begin{cases} \vec{x}_i & \mapsto & \vec{x}_i \\ \vec{p}_i & \mapsto & \vec{p}_i + \vec{f}_i\int_t^{t+\Delta t}\frac{\mathrm{d}t}{a} \end{cases} \tag{2.54}$$

where $\vec{f}_i = -\sum_j m_i m_j \frac{\partial\phi(\vec{x}_{ij})}{\partial\vec{x}_i}$ is the force on particle $i$.

By means of these operators, it is possible to define two variants of the leap-frog time integration scheme, which are second order accurate in the time integration. Defining the time evolution operator $U(\Delta t)$ for an interval $\Delta t$, it is possible to write

$$U(\Delta t) = D\left(\frac{\Delta t}{2}\right) K(\Delta t)\, D\left(\frac{\Delta t}{2}\right), \tag{2.55}$$

or

$$U(\Delta t) = K\left(\frac{\Delta t}{2}\right) D(\Delta t)\, K\left(\frac{\Delta t}{2}\right) \tag{2.56}$$

which correspond to the *drift-kick-drift* (DKD) and *kick-drift-kick* (KDK) leapfrog integrators. The corresponding expressions in terms of the explicit dynamical variables are:

$$\vec{x}_{n+1/2} = \vec{x}_n + \vec{v}_n \Delta t/2 \tag{2.57}$$

$$\vec{v}_{n+1} = \vec{v}_n + \vec{f}(\vec{x}_{n+1/2})\Delta t \tag{2.58}$$

$$\vec{x}_{n+1} = \vec{x}_{n+1/2} + \vec{v}_{n+1}\Delta t/2. \tag{2.59}$$

and

$$\vec{v}_{n+1/2} = \vec{v}_n + \vec{f}(\vec{x}_n)\Delta t/2 \tag{2.60}$$

$$\vec{x}_{n+1} = \vec{x}_n + \vec{v}_{n+1/2}\Delta t \tag{2.61}$$

$$\vec{v}_{n+1} = \vec{v}_{n+1/2} + \vec{f}(\vec{x}_{n+1})\Delta t/2 \tag{2.62}$$

where $\mathrm{n}$ is the last completed time step. This time integration scheme is adopted in GADGET2 because of its *symplectic* properties that make it remarkably stable to perturbations to the Hamiltonian of the system, therefore leading to better conservation of both energy and momentum (see Springel, 2005, for a detailed discussion).

In cosmological calculations of galaxy formation, the simulation code needs to cope with a very large dynamical range, spanning from very dense galactic cores through shock fronts to much lower density regions of the ICM (containing a large amount of mass). In this context, advancing all particles with a fixed time step ends up in a potential waste of computational resources since the long range gravitational forces are subject to very small variations while contributions to a particle's acceleration coming from its small surrounding region (the one accounted for by the tree calculation) can have considerable variations. For these reasons, adaptive and individual time steps are adopted in GADGET2 and the KDK scheme is to be preferred since the Kick operator

is required to be applied only for a limited number of particles, the vast majority being Drifted and Kicked more rarely.

The above considerations apply to both CDM non-collisional particles and to SPH particles, as long as their mutual and self gravitational interaction is considered. SPH particles require additional criteria for time stepping since the inclusion of the artificial viscosity modifies their equation of motion (equation 2.50). In the *signal velocity* approach adopted in GADGET2, the Courant-like hydrodynamical timestep criterion for particle $i$ is expressed by:

$$\Delta t_i^{(\mathrm{hyd})} = \frac{C_{\mathrm{courant}}\, h_i}{\max_j(v_{ij}^{\mathrm{sig}})} \tag{2.63}$$

where $v_{ij}^{\mathrm{sig}} = c_i + c_j - 3w_{ij}$ is the signal velocity as defined in equation (2.48) and its maximum value is taken among the $j$ neighbours of particle $i$ (*gather* approach). $C_{\mathrm{courant}}$ is the Courant factor and, typically, $C_{\mathrm{courant}} = 0.15$.

# Chapter 3

# Modelling and testing

As mentioned at the beginning of Chapter 2, the most widely used techniques in modelling the formation of the LSS in the Universe are the *Lagrangian* and the *Eulerian* approaches. Implementations of these techniques within the numerical tools used in the community can widely differ. With the purpose of testing and comparing the results produced by these numerical tools, several *code comparison* projects have been carried out. For example:

- The Santa Barbara Cluster comparison project (Frenk *et al.*, 1999): this is the *mother* of code comparison projects in which a large number of codes calculated the evolution of a cluster of galaxies, starting from the same initial condition and comparing the results at a given epoch.

- Cosmic code comparison (Heitmann *et al.*, 2008): the most widely used cosmological codes test their gravitational solvers on identical setups.

- Hydrodynamics code comparison (Agertz *et al.*, 2007): both Lagrangian and Eulerian codes test their hydrodynamical solvers on a suite of tests.

- Amsterdam void finder comparison study (Colberg *et al.*, 2008): a comparison of many current void finders on the same region of the Millennium simulation.

- Haloes going Mad (Knebe *et al.*, 2011): a comparison of widely used structure finders on a variety of tests.

- The Aquila project (Scannapieco *et al.*, 2011): a comparison of several cosmological galaxy formation codes when trying to form the same galaxy, from the same cosmological initial conditions.

In a published paper (Tasker *et al.*, 2008), we set out for a code comparison project aimed at testing and comparing two Eulerian codes and two Lagrangian codes on simple physical setups in which both the initial and the final states could be *analytically* described. Our focus was on trying to determine what accuracy in the calculation is needed in Eulerian and Lagrangian codes to behave in a *quantitatively* similar way with respect to known analytical solutions, i.e. we set out to determine which numerical *resolution* is needed to do so.

The codes considered for this purpose are:

- **Eulerian**: ENZO (Bryan & Norman 1997; O'Shea *et al.* 2004) and FLASH (Fryxell *et al.* 2000)
- **Lagrangian**: GADGET2 (Springel 2005; Springel & Hernquist 2002) and HYDRA (Couchman, Thomas & Pearce 1995b; Pearce & Couchman 1997)

In this chapter we discuss a suite of tests for both the gravitational and the hydrodynamical solvers implemented in the GADGET2 simulation code. These tests were our contribution to the comparison study that was presented by Tasker *et al.* (2008).

## 3.1 Sod - shock tube test

It is of great relevance for hydrodynamical codes in astrophysics to be able to capture shocks in order to model several highly energetic phenomena taking place in the Universe that result in strong shock fronts propagating at considerable Mach numbers through a diffuse medium. Among such phenomena, in the numerical modelling of galaxy formation it is important to follow *winds* produced by supernovae explosions or active galactic nuclei (AGN) activity, the collision of interstellar media occurring in galaxy mergers or shocks originated by the infall of diffuse or clumped material, following the LSS and flowing onto galaxy clusters (i.e. *accretion* shocks).

**Figure 3.1:** Sod shock test initial conditions.

The Sod shock tube test (Sod, 1978) allows us to test the code's behaviour against an analytical solution (the solution of the Riemann problem, obtained by the use of the Rankine-Hugoniot conditions). The setup is simple: two fluids with different densities are at rest and separated by a membrane that is then removed. With a proper choice of the initial density gradient between these two regions, a sharp shock interface forms when the membrane separating the two fluids is removed. The time evolution of quantities of interest, along a direction orthogonal to the initial contact interface, can be described analytically. This allows a quantitative assessment of the code's behaviour.

### 3.1.1 Initial conditions

The traditional setup for the Sod test is usually one-dimensional, assumed to model the fluids behaviour orthogonal to the shock front. We have chosen to perform a full three-dimensional model of the fluids' behaviour, in order to better reproduce the systems of interest in complex calculations of galaxy formation scenarios. In order to build the initial conditions pictured in Figure 3.1, two *glass*-like particle distributions have been generated using the dedicated GADGET2 capability. As described in White (1996), an amorphous distribution of particles can be generated by running the code with gravity's sign *inverted*. Given that all particles are assigned the same mass and enabling periodic boundary conditions, this *repulsive* force acts to lead the system towards an equilibrium configuration in which the mean inter-particle separation is maximized. This configuration is obtained avoiding the introduction of artificial *characteristic* lengths such as the grid spacing of a computational mesh. Two such glass distributions have been generated, respectively with $1.6 \times 10^6$ (big) and $4 \times 10^4$ (small) particles, and slabs have been cut out of these 3D computational volumes in a suitable way in order to create both the setups pictured above (each containing $10^6$ particles) in which, respectively, the membrane separating the two fluids is oriented at $90^\circ$ to the x-axis of the

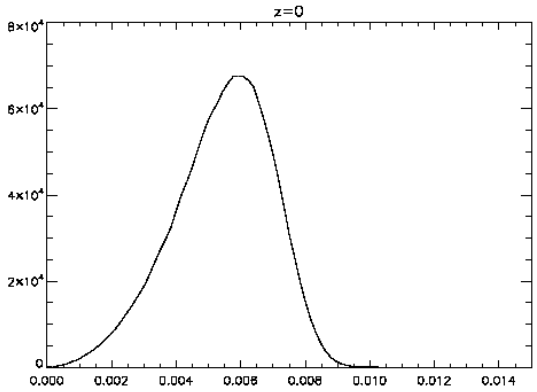


**Figure 3.2:** Small glass: Gaussian fit of the distribution function of the nearest neighbour separations for all the particles in the computational volume at an early stage of *glass* generation.

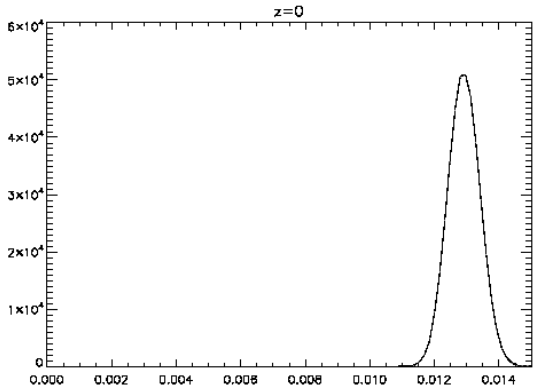


**Figure 3.3:** Small glass: Gaussian fit of the distribution function of the nearest neighbour separations for all the particles in the computational volume at a later stage of *glass* generation. Comparing with the above figure it is possible to see that the system is lead towards an equilibrium configuration that maximises the inter-particle separation.

box ([1,0,0] plane) and at 45° to each of the $x, y$ and $z$ axes ([1,1,1] plane). These two different orientations for the shock propagation will also highlight possible directional dependencies of the hydrodynamical solver. In order to also assess resolution effects on the code's behaviour, we have also generated the above setups for a computational box containing $250,000$ particles.

### 3.1.2 Runs and Results

In this test, fluids are modelled as perfect fluids with a polytropic index $\gamma = \frac{5}{3}$, moreover periodic boundaries on the cubic computational box have been enabled.

**Table 3.1:** Sod shock setup parameters.

| State | Right | Left |
|---|---|---|
| $\rho$ | 4 | 1 |
| p | 1 | 0.1795 |
| v | 0 | 0 |

The choice of the values of the physical quantities for the initial states is that of Table 3.1 and the results have been analyzed at $t = 0.12$, just prior to the wrapped shock fronts overlapping in the inclined case.

In the SPH integration, we have adopted the standard 32 neighbours for the smoothing of physical quantities (i.e. particle density), running the code in CGS units. All the following plots are consistent with this system of units.

The shock front and the contact discontinuity move from the high density region into the low density one (i.e. right to left in the following figures), while a rarefaction wave moves in the opposite direction.

The membrane initially separating the two fluids is positioned at $x = 0$, and:

- at $t = 0$, the particles representing the high density fluid have positive $x-$values while the low density particles have negative $x-$values.
- Each profile has been produced orthogonally to the initial discontinuity surface, by averaging particles' physical quantities within each bin, for a total of 200 equally sized bins.
- The computational box is cubic, centered at $(0, 0, 0)$ and with linear size $L = 1$.
- At $t = 0.12$, looking at the density panels in the following figures and moving from positive to negative values of the $x-$coordinate three characteristic *jumps* can be identified: respectively the *rarefaction wave* (RW, or sound wave SW), the *contact discontinuity* (CD) and the *shock discontinuity* (SD).

- The *entropy* profile has been produced defining the *computational* entropy *s* as:

$$s = \frac{T}{\rho^{\gamma-1}} \tag{3.1}$$

- We set the strength of the artificial viscosity parameter $\alpha = 1$, as discussed in equation (2.44) above.

- The *energy* panel is actually showing the behaviour of particles' internal energy per unit mass, as calculated by GADGET2.

- The *velocity* panel, shows the modulus of the projected linear velocity of particles along the direction of analysis (i.e. perpendicular to the initial CD orientation).

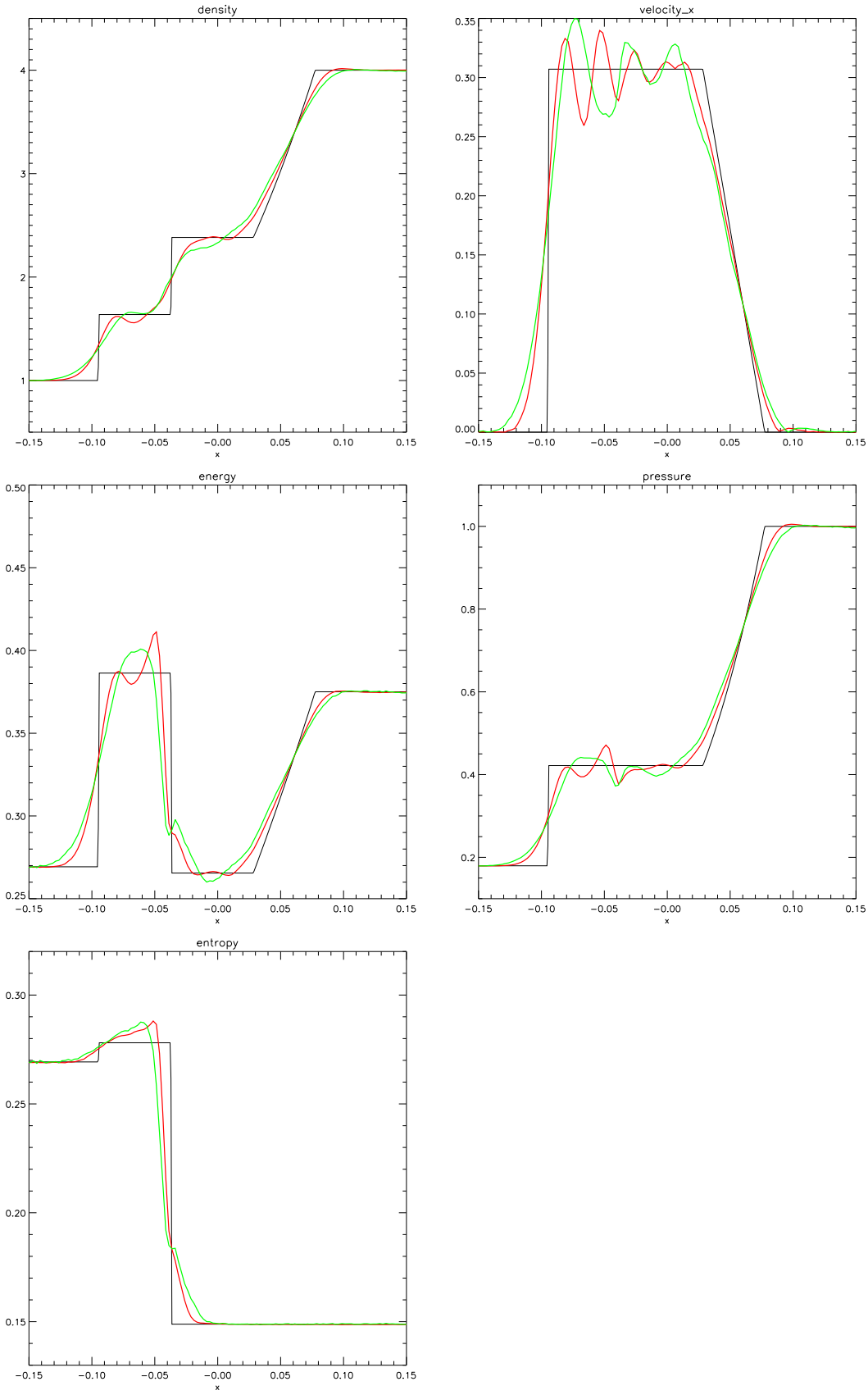


**Figure 3.4:** [1,0,0] setup: the black line is the theoretical solution, green is the $250,000$ particle setup, red is the $10^6$ particle setup. Analysis has been performed in a direction orthogonal to the initial contact interface (i.e. the $x$-axis in this case), for the chosen end–state $t = 0.12$.

Considering Figure 3.4 and focusing on the red line, it is possible to see how the GADGET2 implementation of SPH successfully passes the test. This should be no surprise as the Sod test forms a standard test case for astrophysical fluid codes (see for instance Springel, 2005 for a 1-D, high resolution, very finely tuned Sod test). The analytical solution is reasonably well recovered, while it is possible to identify several features peculiar to SPH solvers.

The SW propagation is well recovered in all profiles, with negligible departures with respect to the analytical solution. On the other hand the CD is poorly handled by the code: after the removal of the membrane separating the two fluids ($t = 0.$), two very different particle distributions suddenly appear next to each other: SPH smoothing between particles belonging to such different distributions give rise to the appreciable ringing in the velocity profile, which is clearly reflected in a considerable overshoot in both the energy and entropy profiles. A very characteristic feature of SPH is the appearance of the so called *pressure blip* in the pressure profile, at the CD position. This is due to the generation of spurious pressure forces as discussed in section (2.2.1), and outlined in equation (2.50) above.

The SD position is well recovered even if a considerable smoothing of this discontinuity can be noticed in all profiles. A considerable post-shock ringing can also be noticed in the velocity profile. Lagrangian techniques capable of solving the equations of hydrodynamics need the introduction of an *artificial viscosity* term in order to model the behaviour of dissipative phenomena. This is necessary in order to prevent particle interpenetration, which is, by definition, not an issue in the Lagrangian modelling of non-dissipative phenomena. SPH introduces an artificial viscosity parameter which is conventionally set to unity but in our setup this value does not appear to be sufficiently effective at capturing and modelling shock discontinuities.

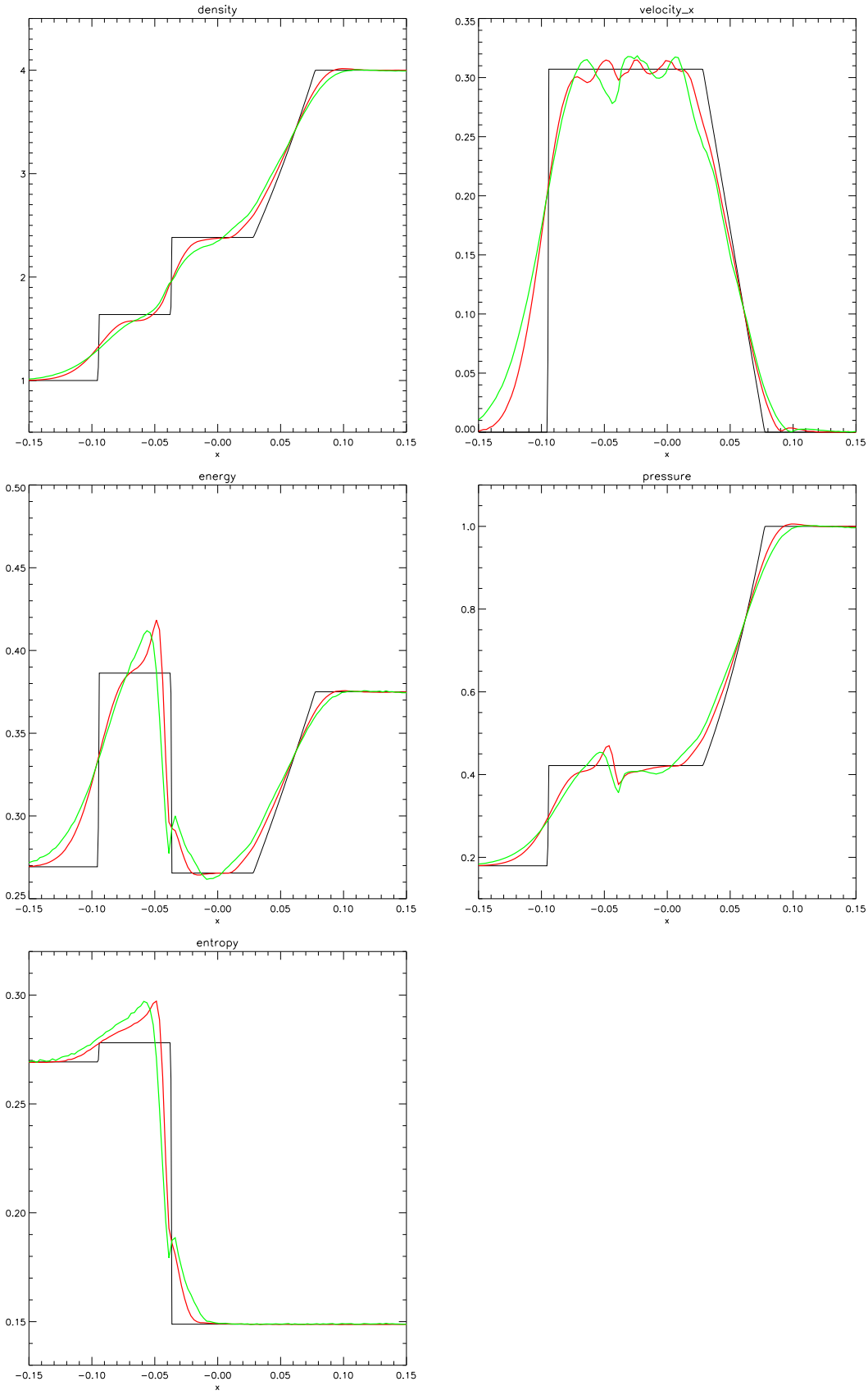


**Figure 3.5:** Increased viscosity, [1,0,0] setup: the black line is the theoretical solution, green is the $250,000$ particle setup, red is the $10^6$ particle setup. Analysis has been performed in a direction orthogonal to the initial contact interface (i.e. the $x$-axis in this case), the chosen and-state $t = 0.12$

.

Setting the artificial viscosity parameter $\alpha = 2$ (i.e. double its standard value) leads to a considerable reduction of the ringing in the velocity profiles, as it can be seen by comparing Figure 3.5 with Figure 3.4. On the other hand, the SD jump is still poorly recovered in all other profiles: this choice for the artificial viscosity parameter smooths the discontinuity even more, with respect to the standard value.

By comparing the green and the red lines, it is possible to appreciate the effects of varying the resolution on this SPH calculation. Reducing the number of particles (green lines) leads to a poorer sampling of the fluids: the SPH smoothing volumes are larger in this case and this acts both in smearing out the pressure blip and in reducing the energy overshoot at the CD location. On the other hand, the SW and, most importantly, the SD are even more smoothed. The post shock ringing in the velocity profiles appears not to depend on resolution.

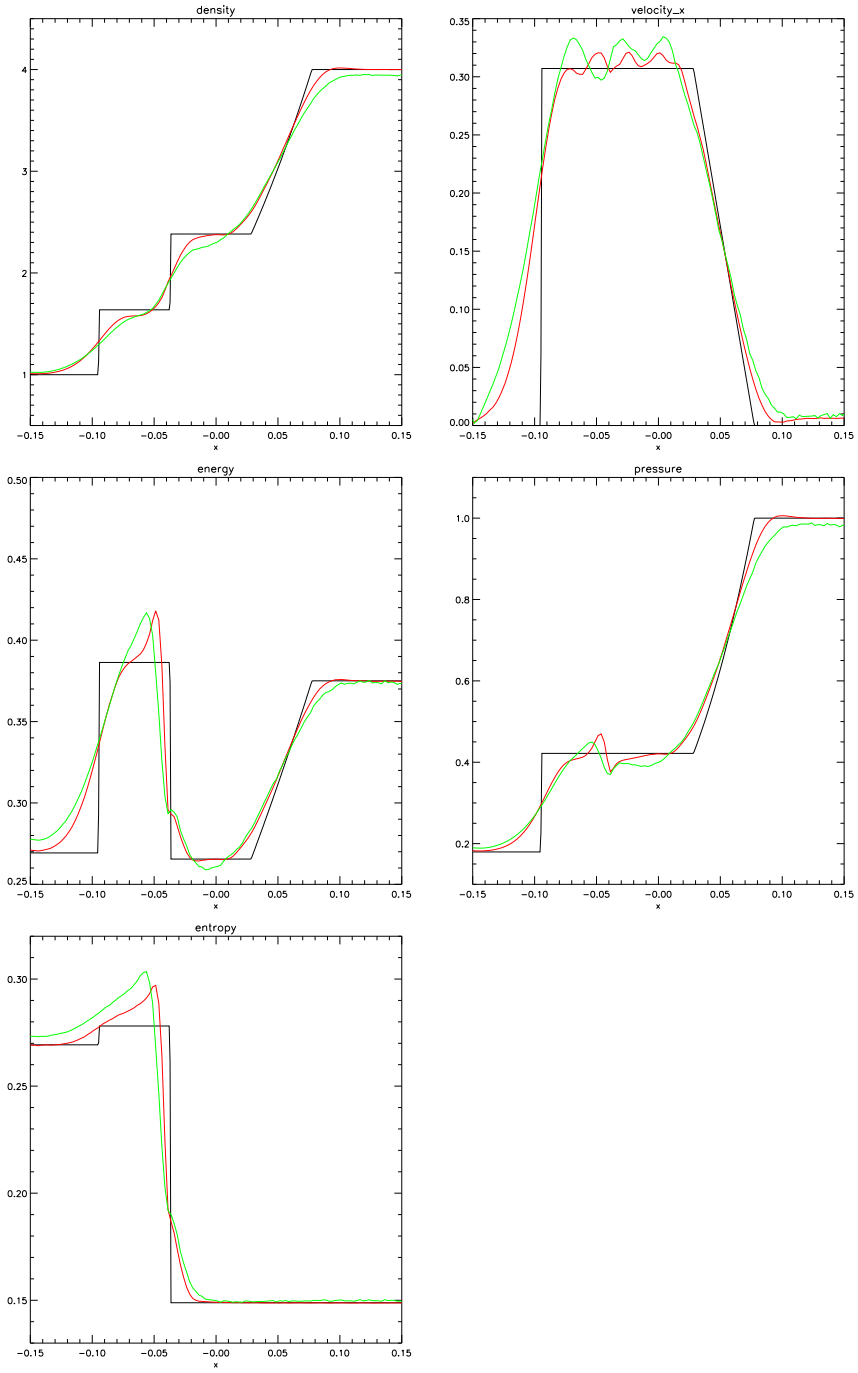


**Figure 3.6:** Increased viscosity, [1,1,1] setup: the black line is the theoretical solution, green is the $250,000$ particle setup, red is the $10^6$ particle setup. Analysis has been performed in a direction orthogonal to the initial contact interface (i.e. along the diagonal of the cubic computational box, in this case) for $t = 0.12$

Comparing Figure 3.5 with Figure 3.6, no clear orientation dependency can be noticed in the GADGET2 solution of the Sod test. This is expected, since SPH does not introduce any directionality and only depends solely on the relative distance of the Lagrangian particles it uses as tracers.

## 3.2 Sedov blast wave test

In this fully hydrodynamical test (no gravitational interaction is taken into account), a considerable amount of energy is deposited in a very small region at the center of a cubic computational volume, resulting in an intense explosion propagating through an homogenous background medium. This test can be considered as representative of the very energetic explosions occurring in supernovae events.

In the Lagrangian modelling, due to the introduction of *artificial viscosity* briefly discussed in the previous section, the spherical shock front sweeps up particles as it propagates through an unperturbed medium. This allows SPH to concentrate resolution elements on the shock front itself, this being the densest region.

Sedov (1959) obtained an analytic solution for the propagation of the shock front due to a point source explosion. The shock front's radius is given by:

$$r(t) = \left( \frac{E_0}{\alpha \rho_0} \right)^{1/5} t^{2/5} \tag{3.2}$$

where $E_0$ is the initial energy injected, $\rho_0$ is the background density and $\alpha = 0.49$ for an ideal gas with $\gamma = 5/3$.

In absence of radiative cooling and gravitational interaction the problem is unitless.

### 3.2.1 Sedov test setup

We considered a shock propagating in a box of linear size $L = 10$, caused by the injection of an energy $E_0 = 10^5$ in a very small spatial region at the center of the box (ideally this should be a point-like injection). We choose a density $\rho = 1$ for the unperturbed ideal gas, with $\gamma = \frac{5}{3}$. The chosen value for $E_0$ results in an *extreme* shock: this has been explicitly chosen in order to stress the hydrodynamic solver.

Also in this case we started with $10^6$ SPH particles in a relaxed *glass*-like distribution, injecting the energy within a top-hat sphere containing the central 32 particles. The SPH integration has been performed smoothing on the 32 nearest neighbours for each SPH particle.

It is worth mentioning a time step issue we noticed from the outset: these calculations

have been performed allowing for the use of adaptive timesteps for individual particles, as is common practice in galaxy formation calculations. In GADGET2 it is possible to specify a range in which the timesteps are allowed to vary: with a standard choice (see equation 3.3), and given the very high energy input, we observed particle interpenetration effects. In order to limit this, we had to almost force a fixed, very small, time step for all particles. We also decide to adopt $\alpha = 2$ for the artificial viscosity parameter.

This issue has subsequently been well documented for GADGET2. Saitoh & Makino (2009) pointed out that, for codes allowing individual particle timesteps, particles with overlapping SPH smoothing lengths should not be allowed timesteps more than a factor of 4 apart. Such a timestep range limiter is not a part of the standard Gadget2 distribution but is required in the presence of strong shocks such as the one imposed here. Recently, several groups (Durier & Dalla Vecchia, 2012, Reed et al 2011) have implemented the so called Saitoh switch into various forms of Gadget. Durier & Dalla Vecchia (2012) explicitly show the issues related to a Sedov blast test almost identical to the one used here.

### 3.2.2 Runs and Results

In Figure 3.7 the radial profiles of the hydrodynamical quantities of interest are shown:

- GADGET2 successfully recovers the position of the spherical shock front.
- The shock front is smoothed out in the radial direction, this being a direct effect of the SPH smoothing between particles lying within the shock front and particles belonging to the unperturbed background medium.
- The shock front is reproduced in the calculation as a spherical shell, rather than a spherical surface. This is caused both by the SPH artificial viscosity that limits (by construction) the compressibility of the fluid and by the finite discrete sampling of the medium. The net result is the underestimation of the density peak and the systematic (but small) underestimate of the pressure profile.
- The velocity profile shows considerable ringing in the post shock region, overestimating on average the theoretical prediction: this is essentially due to the fact

that in the Gadget2 implementation of SPH particles are sorted in an *entropy-related* quantity at first (see equation 2.38), and then the kinematics are calculated. This allows the conservation of both entropy and internal energy to a great extent, but leaves the short range kinematics disordered.

- The internal energy radial profile is recovered very well: the slight underestimate inside the shock region is caused by the broadening of the shock front.

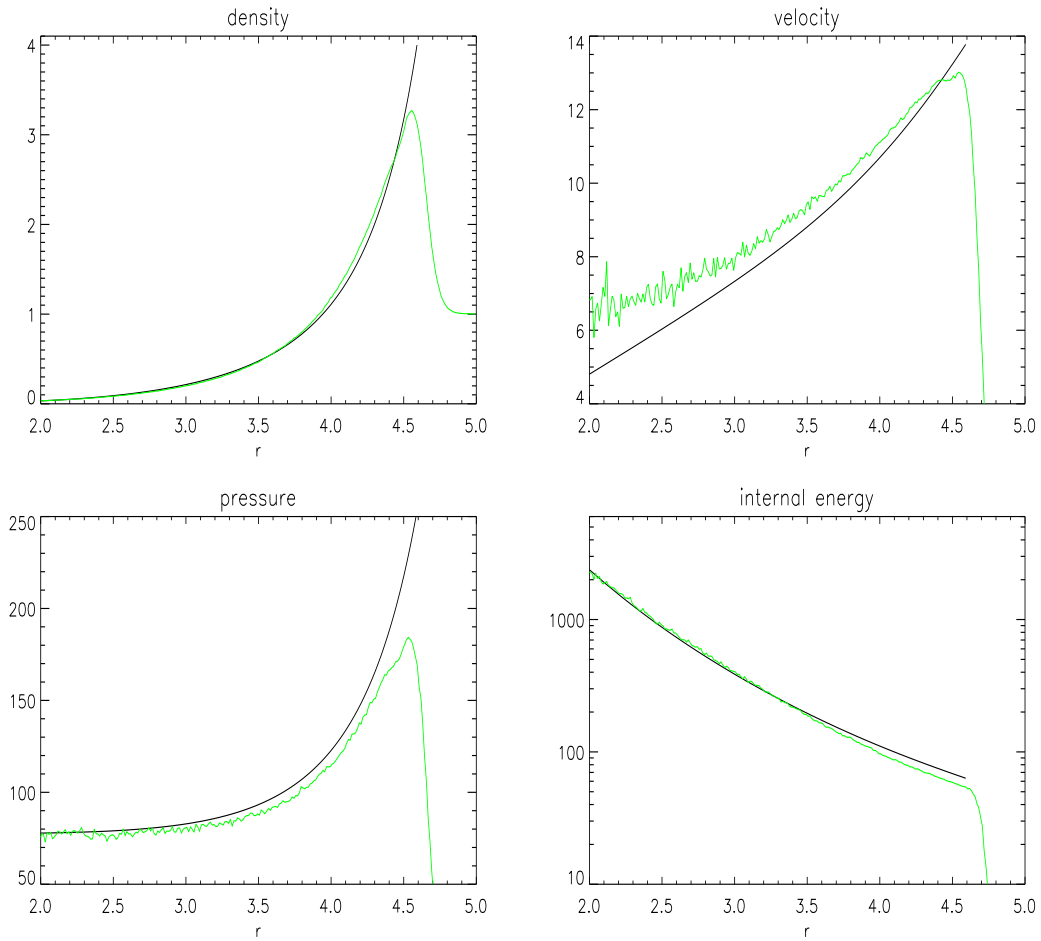


**Figure 3.7:** Radially binned profiles (green lines) produced considering 500 radial bins, logarithmically spaced. The black lines show the theoretical Sedov solution at this time (t=0.1).

A visual impression of the end state of this setup is provided in the Figure 3.8.

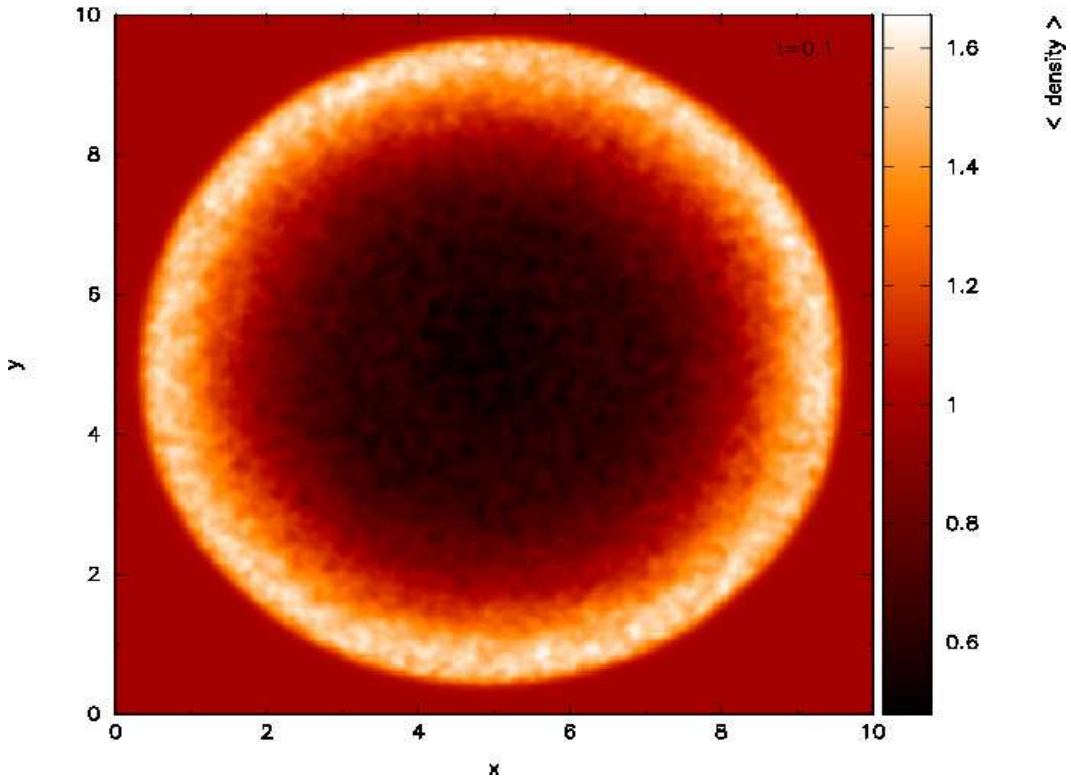


**Figure 3.8:** Sedov, 32 particle, spherical top-hat energy injection: column density projection map along the z-axis, for all particles in the box at $t = 0.1$.

In Figure 3.8, GADGET2 is shown to recover the spherical shape of the shock front well but the grainy appearance of the shock front suggests the presence of a *noisy* density distribution: this is a hint that particles in the shock front might not be *uniformly* distributed in physical space, within the shock shell region.

In order to investigate further the details of this issue, we decided to vary the energy injection method:

- CP/32 neighbours: in this setup we injected $E_0$ in the most central particle and integrate the SPH quantities on the nearest 32 neighbours.
- TH/64 neighbours: in this setup, the injection was distributed within a top-hat profile on the central 64 particles. Consistently we performed the SPH integration over the nearest 64 neighbours for each particle.
- GUASS/64 neighbours: in all the other setups, the small region of energy injection has very sharp *edges* (i.e. energy jumps many orders of magnitude among neighbouring particles). We smooth the injection energy with a Gaussian profile, truncated at 10 percent of the peak value: this mitigates the *sharpness* of the injection region but, as a drawback, the volume within which the energy is injected is spatially broadened.

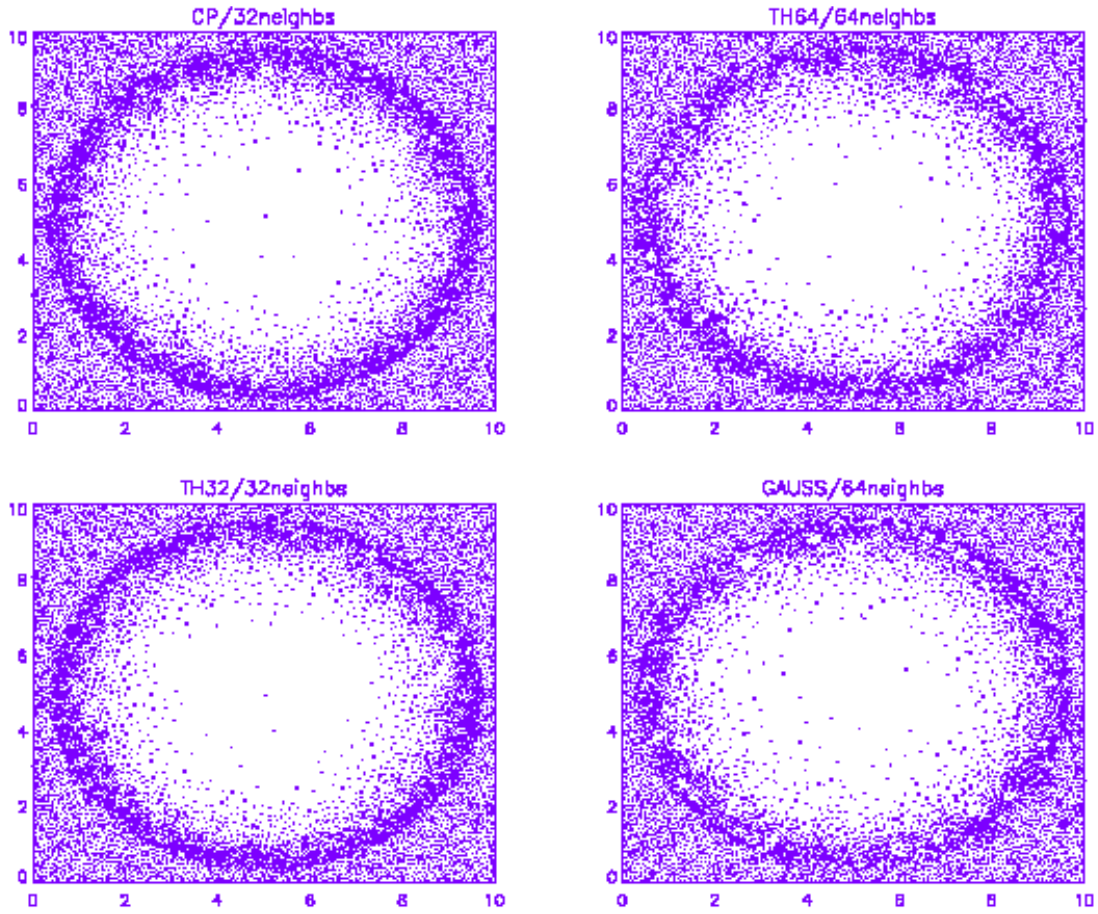


**Figure 3.9:** Sedov: projection along the z - axis of particles in a slab through the center of the box (one mean interparticle separation thick) for different setups.

In Figure 3.9, for each of the aforementioned setups, the z-axis projection of the particle positions in a slab through the center of the volume is shown. Moving from top to bottom and left to right, it is possible to appreciate how the shock front shell is broadened as the volume of the region of injection is increased. The shock front is also broadened as the volume over which the SPH is smoothed is increased (i.e. increasing number of neighbours). The *grainy* aspect noticed in Figure 3.8 is also present in the other setups: there are particles in the shock region that have an empty small spherical region around them, resembling *bubble*-like structures in the shock front. The persistence of these structures is not surprising given that the lack of a timestep limiter in all the runs.

The corresponding radial profiles for density, velocity and pressure are presented in the following figures:

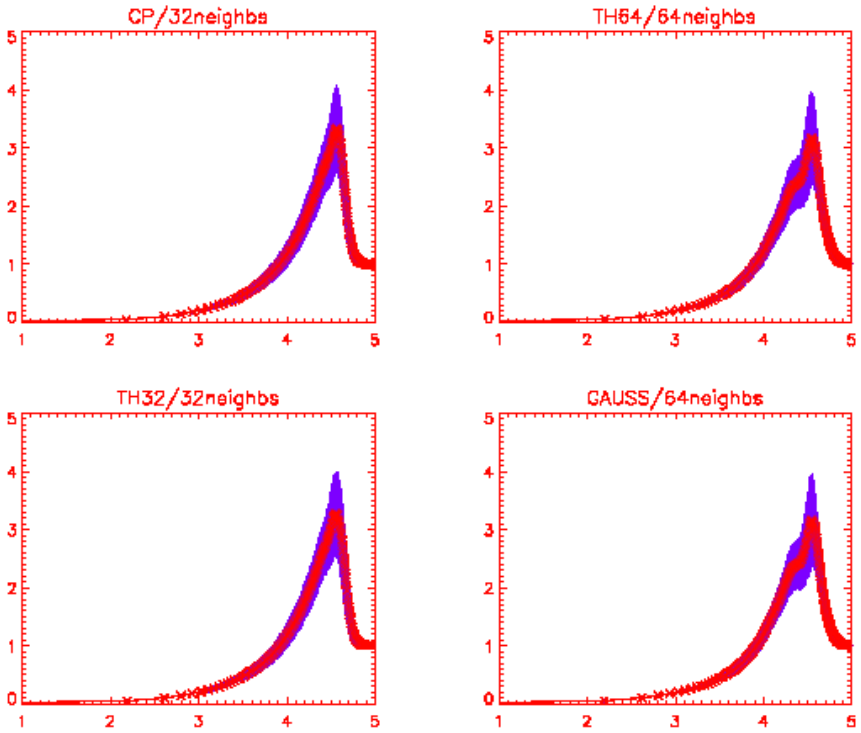


**Figure 3.10:** Density: radially binned density profiles for different setups. Blue lines are the corresponding RMS in each bin.

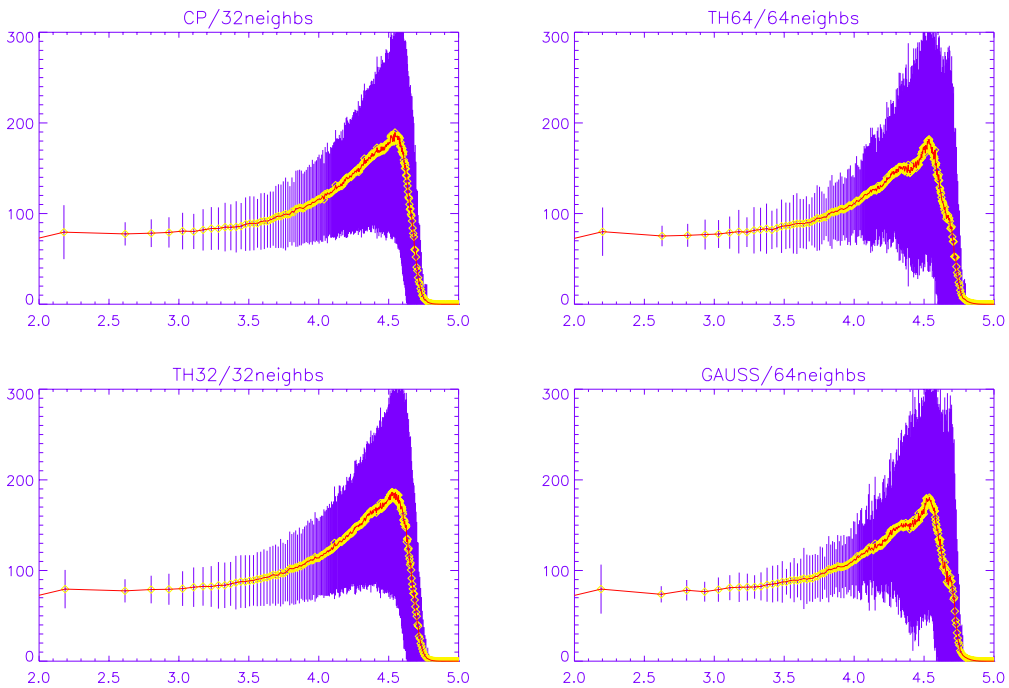


**Figure 3.11:** Pressure: radially binned pressure profiles for different setups. Blue lines are the corresponding RMS in each bin.

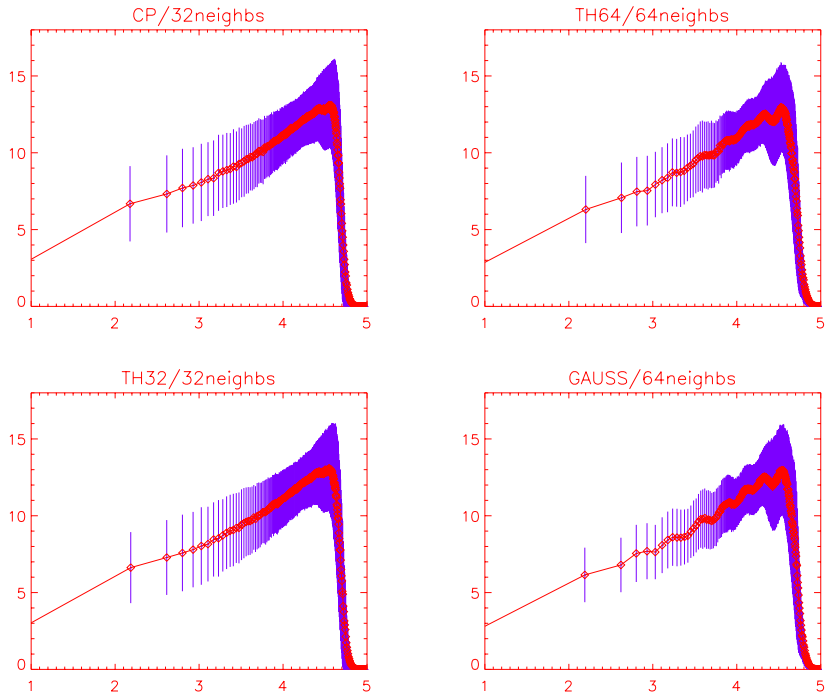


**Figure 3.12:** Velocity: radially binned profiles of the radial velocity component, in different setups. Blue lines are the corresponding RMS in each bin.

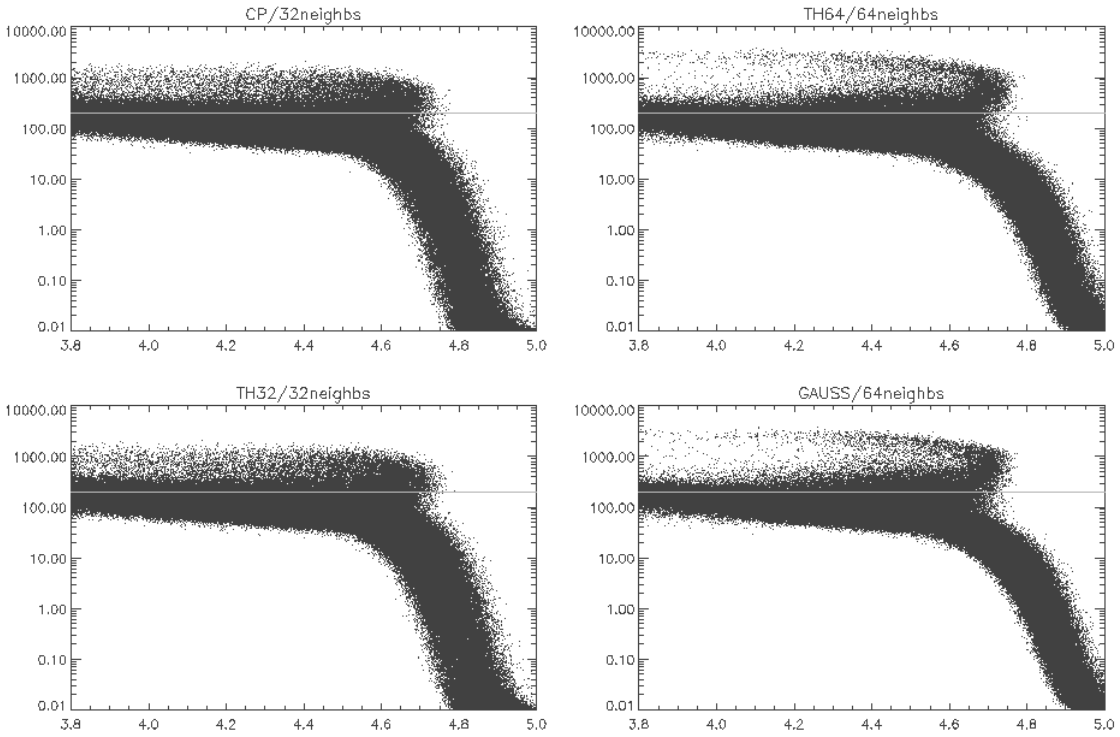


**Figure 3.13:** Energy: internal energy for all particles in the shock region. The formation of an overly energetic *plume* of particles is clearly visible.

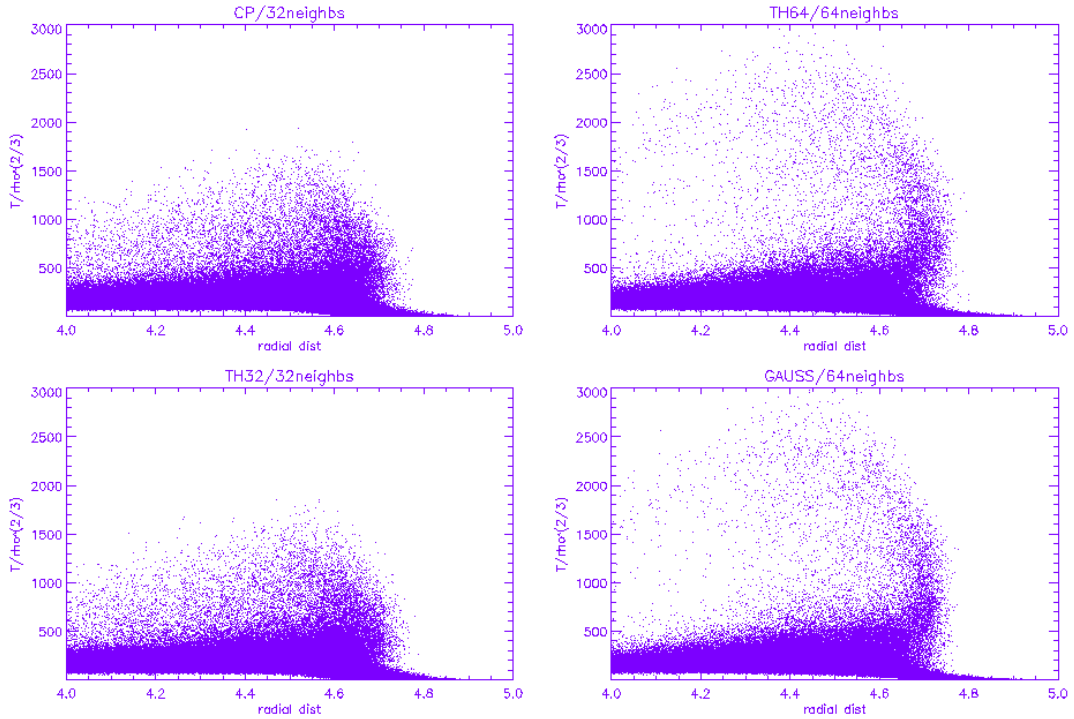


**Figure 3.14:** Entropy: computational entropy (Equation 3.1) for all particles close to the shock front.

Varying the energy injection method, the most noticeable features appear right behind the theoretical radial position of the shock front: as noticed in Figure 3.9 the thickening of the shell containing the shock front and the increase of the SPH smoothing volumes drive the formation of *bubble*-like structures. This corresponds to a progressive underestimate in the binned radial density profiles right behind (i.e. at smaller radius) the shock front, as it can be noticed in Figure 3.10. The increased broadening ahead (larger radius) of the shock front is also responsible for the progressive underestimation of the peak density. These two features are reflected in the binned radial pressure profiles (Figure 3.11), which become progressively more disordered across the shock front.

At the same radial position, in Figure 3.12 it is also possible to notice the appearance of fluctuations in the radial velocity profiles. This reflects a progressively larger disorder in the velocity field in the immediate post-shocked regions.

The most evident feature clearly emerges when looking at the internal energy of the particles: a plume of over energetic particles appears immediately after the shock front (Figure 3.13). This becomes even clearer when looking at each particle's computational entropy as defined in equation 3.1. For a close-up of the shock region see

Figure 3.14. In the GADGET2 implementation of SPH, a gas particle cannot loose its internal entropy so the over energetic particles remain well above the theoretically predicted value a long time after they have been shocked (see equation 2.41). This is again a direct consequence of the large range in timesteps allowed at the same physical location by GADGET2. These problems are particularly evident in test cases such as the one here, where very strong shocks are present.

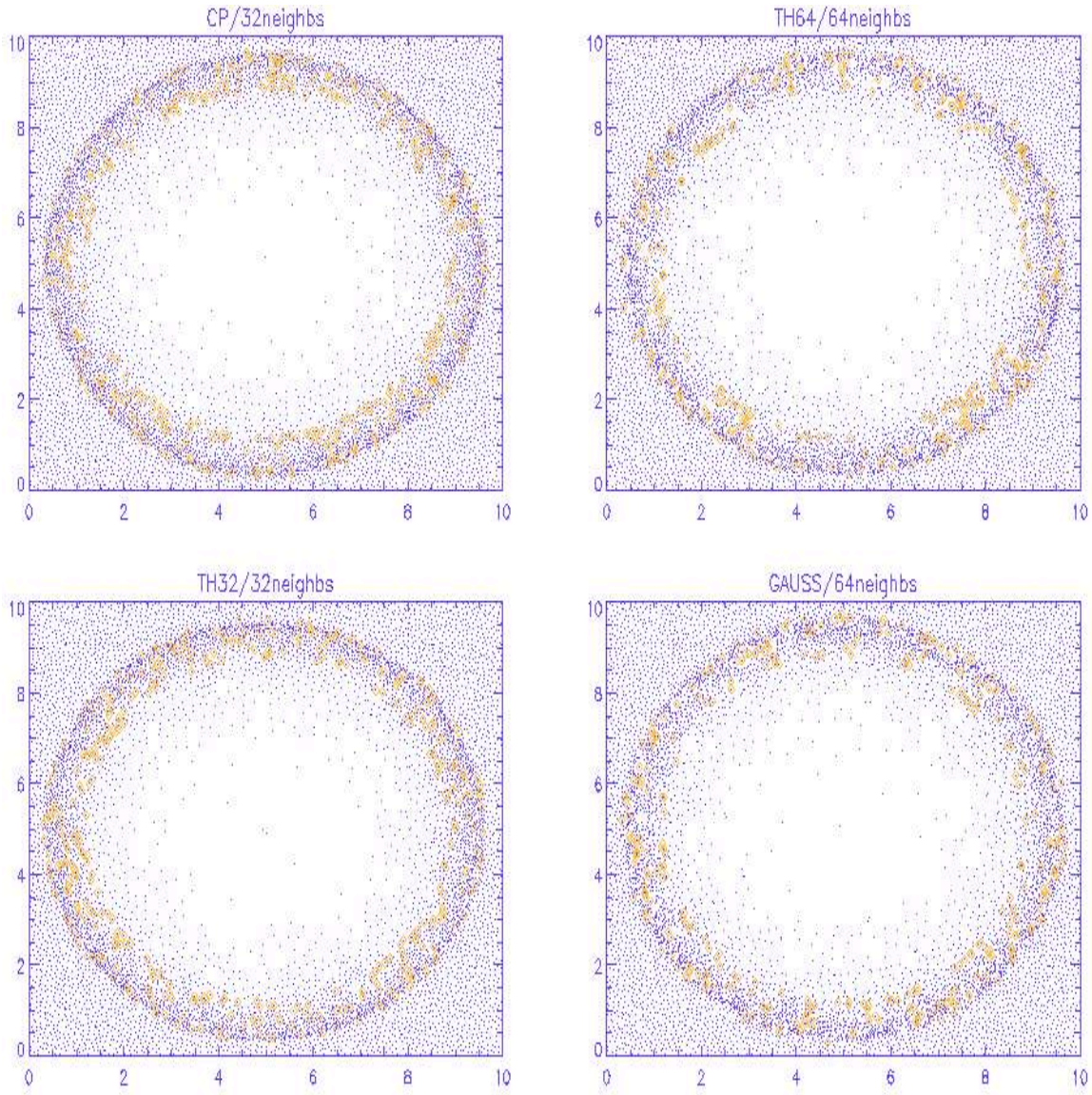


**Figure 3.15:** Projection along the z-axis of the position of particles located in a slab, through the center of the box, of thickness comparable to the average SPH smoothing length. Over energetic particles are marked in yellow.

In Figure 3.15, particles belonging to the over energetic *plume* have been marked in yellow. The reason why these particles become over energetic resides in the hydrodynamical time stepping scheme implemented in Gadget2: SPH particles are assigned a time step value which is a function of the signal velocity ($v_{sig}$, see equation 3.3).

For particles in the homogeneous medium, not immediately close to the initial energy injection, a relatively big timestep size is assigned by the algorithm: these particles becomes *SPH-idle*, while the *drift* (D) operator is applied to them (see section 2.3). In our setup, given the very high energy input, the blast wave propagates at very high

speed (high Mach number) compared to the drifting time of idle particles in the surrounding medium. When the SPH particles of interest become *active* and the *kick* (K) operator is applied to them, they end up finding themselves within the shocked region, thus suddenly acquiring a very high amount of energy.

If the maximum allowed time step size is large, compared to the characteristic propagation time of the blast wave, the *awakened* particles might find themselves well behind the shock front, leading to the particle interpenetration observed in Section 3.2.1. Alternatively, if the maximum allowed timestep size is small, the *awakened* particles find themselves within the shock front, driving the formation of bubbles described above.

Our discussion of these findings with the GADGET3 developers, led to the development of a *wake-up* mechanism which is currently implemented in GADGET3 code.

In GADGET2 the hydrodynamical timestep is assigned as in equation 3.3:

$$\Delta t_i^{(\mathrm{hyd})} = \frac{C_{\mathrm{courant}}\, h_i}{\mathrm{max}_j(v_{ij}^{\mathrm{sig}})} \tag{3.3}$$

where $\mathrm{max}_j(v_{ij}^{\mathrm{sig}})$ is the maximum value of $v^{sig}$ among the $j$ neighbours of particle $i$. In this *gather* approach (see Hernquist & Katz 1989 for a definition of *gather* and *scatter* implementations of SPH), particle $i$ is assigned with a timestep that is inversely proportional to the largest $v_j^{sig}$ among its neighbours.

In the *wake-up* mechanism, this approach is reversed to a *scatter* implementation of the time step assignment: centering on particle $i$ (let's assume it is SPH active and located in the shock front), if $v_i^{sig} > v_j^{sig}$ for all of its $j$ neighbours, then the assignment $v_j^{sig} = v_i^{sig}$ is made. In this way, all SPH neighbours of particle $i$ will be assigned a smaller timestep (much smaller than the one adopted by SPH particles lying in the unperturbed medium) and their status moved from SPH "idle" to SPH "active". In order to obtain a strict conservation of momentum and energy, the newly "awakened" particles are drifted (D) back to their previous time step, and the *kick* K operator is applied with the new $\Delta t_j^{(hyd)}$.

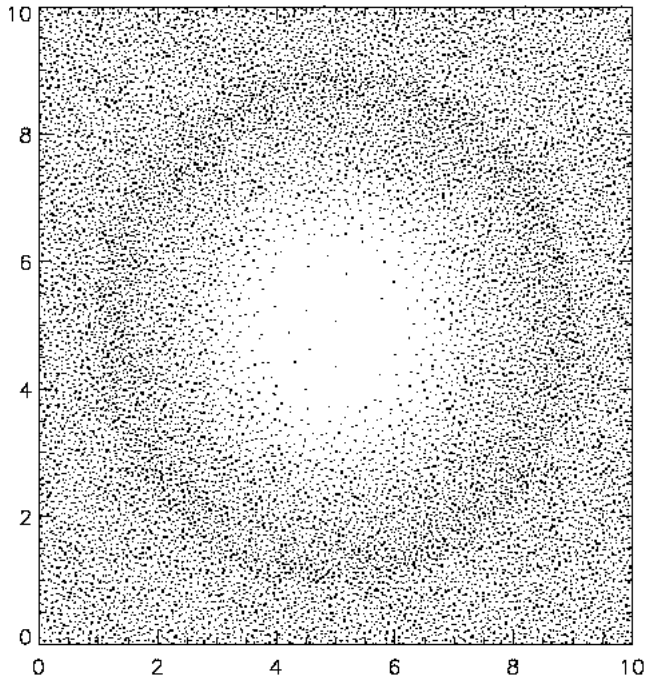


**Figure 3.16:** Reproducing the Sedov test discussed in Springel & Hernquist 2002, we obtain the correct answer.

## 3.3 Static and translating King spheres

Adding self-gravity, where every fluid element is affected by every other, dramatically complicates the situation and it is not possible to design a test with an exact analytical solution anymore. Since it is still essential for the purpose of this comparison that our problems remain well-posed, we select situations in which the correct behaviour of the system is known, even if it cannot be mathematically expressed. To do this, we perform two tests; the first of these concerns a static gas profile in equilibrium. Gravity acts to try and collapse the gas, while pressure pushes it outwards. While these forces remain perfectly balanced, the gas remains at rest. This situation is analogous to a relaxed galaxy cluster and requires the code to resolve the gas density over many orders of magnitude. The second test involves the same cluster translating through the simulation box. By using periodic boundary conditions, the cluster's velocity is chosen such that it should return to its original position after 1 Gyr. With no external forces, the cluster should remain in hydrostatic equilibrium and retain its profile during the translation.

### 3.3.1 Initial conditions

The model we used for the galaxy cluster is the King model King (1966), which was chosen because it possesses a finite radial cut-off, and is therefore a well defined problem. Its form is based on the distribution function:

$$f(\epsilon) = \begin{cases} \rho_c (2\pi\sigma^2)^{-3/2} \left( e^{\epsilon/\sigma^2} - 1 \right) & \epsilon \geq 0, \\ 0 & \epsilon < 0 \end{cases} \tag{3.4}$$

where $\epsilon = \Psi - \frac{1}{2}v^2$, is the coordinate change for the shifted energy, $\rho_c$ is the central density and $\sigma$ is related to (but not equal to) the velocity dispersion. The resulting density distribution of this cluster vanishes at the *tidal radius*, $r_t$. Integrating over all velocities yields a density distribution:

$$\rho\left(\Psi\right) = \rho_c \left[ e^{\frac{\Psi}{\sigma^2}} \operatorname{erf}\left( \sqrt{\frac{\Psi}{\sigma^2}} \right) - \sqrt{\frac{4\Psi}{\pi\sigma^2}} \left( 1 + \frac{2\Psi}{3\sigma^2} \right) \right]. \tag{3.5}$$

Putting this into the Poisson equation (Equation 2.3) results in a second order ODE which can be solved numerically.

This model has three independent parameters, the mass of the cluster, the tidal radius and the concentration $c = \log_{10}(r_t/r_0)$, where $r_0$ is the central or *King radius*. For this problem, we selected a concentration of 3, $r_t = 1\,\mathrm{Mpc}$ and a cluster mass of $10^{14}\,\mathrm{M}_\odot$. This results in a King radius of $1\,\mathrm{kpc}$. Therefore, to successfully maintain hydrostatic equilibrium, the code must be able to model the cluster out to $1\,\mathrm{Mpc}$ while resolving the $1\,\mathrm{kpc}$ core. This makes it a particularly challenging test. The two key requirements for success in this test are to be able to resolve the core and to have an accurate gravitational solver. Although the King model does not have an analytical solution, a one-dimensional numerical solution for the cluster's profile can be achieved from a simple numerical integration.

We setup the King profile using 100,000 particles, radially perturbing a glass to the desired density profile within a periodic 3 Mpc box.

### 3.3.2 The static King halo

We evolved the *static* King halo both testing the *gravitational tree* algorithm (see section 2.1.2) and the Particle-Mesh (PM) gravity solver (see section 2.1.3) as implemented in the GADGET2 code, and described in section 2.1.4.

In testing the tree algorithm we switched off the PM calculation within GADGET2 and we adopted the standard value $\alpha = 0.6$ in the "opening criteria" as in equation (2.19). Independently, we also tested the accuracy of the PM gravity solver by reducing the tree calculation range to a value close to zero ($r_s \simeq 0$, with $r_s$ described in section 2.1.4).

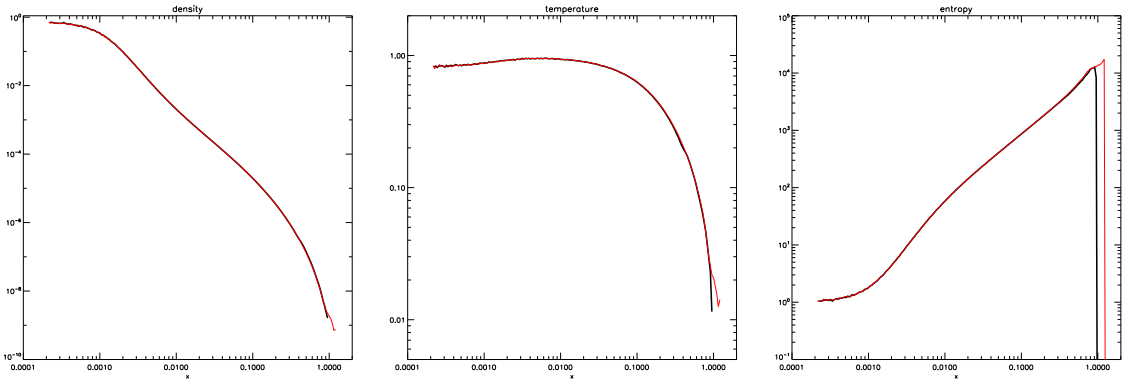


**Figure 3.17:** Treecode result for the static King sphere. Left to right, radially binned profiles for density, temperature and computational entropy are shown. The black lines are the initial $t = 0$ values, while the red lines represent the profiles after 1 Gyr.

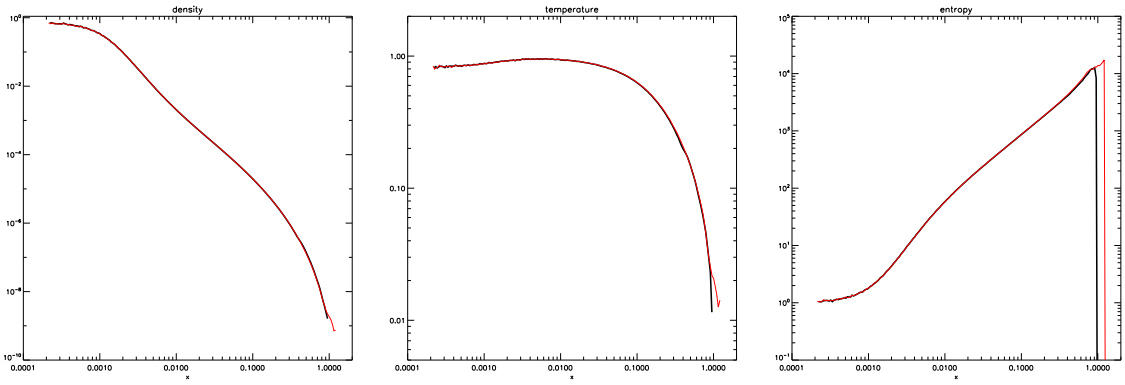


**Figure 3.18:** PM result for the static King sphere. Left to right, radially binned profiles for density, temperature and computational entropy are shown. The black lines are the initial $t = 0$ values, while the red lines represent the profiles after 1 Gyr.

As shown in Figures 3.17 and 3.18, GADGET2 is successful at keeping the cluster in equilibrium and resolving the core well: the initial profiles are matched over seven orders of magnitude, down to densities of $10^{-10}$. In both tests, negligible deviations from the static King profile appear after 1 Gyr: at the lowest density edge of the cluster, small deviations ($\sim 15\%$) from the profile are seen as the cluster edge diffuses into the background and the model starts to run out of particles.

In testing GADGET2's tree code, we encountered a problem in this static test. Although the radial profiles were very stable, the cluster as a whole tended to drift around over time. This is due to the difficulty of very accurately determining the lowest order term in the gravitational force expansion for a treecode. Each individual term includes a small error, with these errors largely but not exactly uncorrelated. Under these conditions the total momentum of the system is not guaranteed to be conserved exactly and a "random walk" occurs. As the configuration is designed to be entirely static the direction of the residual force is highly correlated from one step to the next and despite recovering the correct value to one part in $10^8$ this still leads to a net drift. It is possible to circumvent this, as shown above, by dramatically reducing the opening angle for the tree but this rapidly negates the advantage of using a tree in the first place. For more normal simulations this tiny zeroth order force error is of course negligible as the random motion of the particles disorders the direction of the drift error as time progresses.

### 3.3.3 The translating King halo

Using the stable cluster developed above we can test the Galilean invariance of the code by giving a velocity relative to the static simulation volume. This is a commonly encountered situation for cosmological simulations where large objects often move at many hundreds of kilometers per second relative to the background. For this test the cluster was given a bulk velocity such that, in 1 Gyr, it moved around the simulation box once, returning to its original starting position. Since there are no external forces acting on the cluster, the end profile should be identical to the initial one. In this test we employed the standard hybrid TreePM gravity solver. The radial profiles for the end state ($t = 1Gyr$) have been calculated centering on the King halo center at $t = 0$.

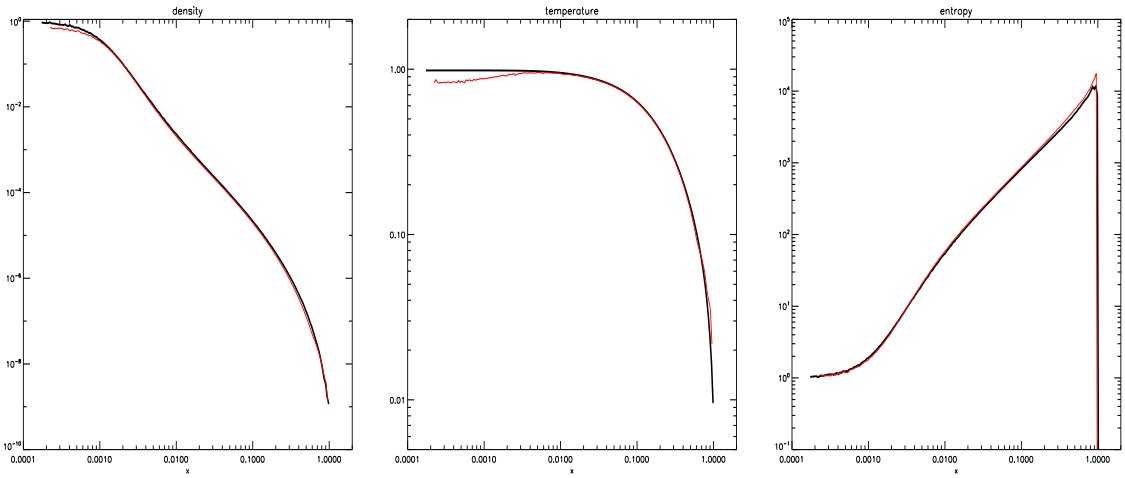


**Figure 3.19:** King translating - TreePM. Left to right, the radial profiles for density, temperature and entropy are shown. Black lines represent the status of the King halo at $t = 0$, while red lines represent the final status.

The code maintains the density profile of the cluster extremely well, with the only deviations appearing in the core, and essentially due to a small offset in returning to the initial position of the halo. Figure 3.20 shows the residue remaining if the initial

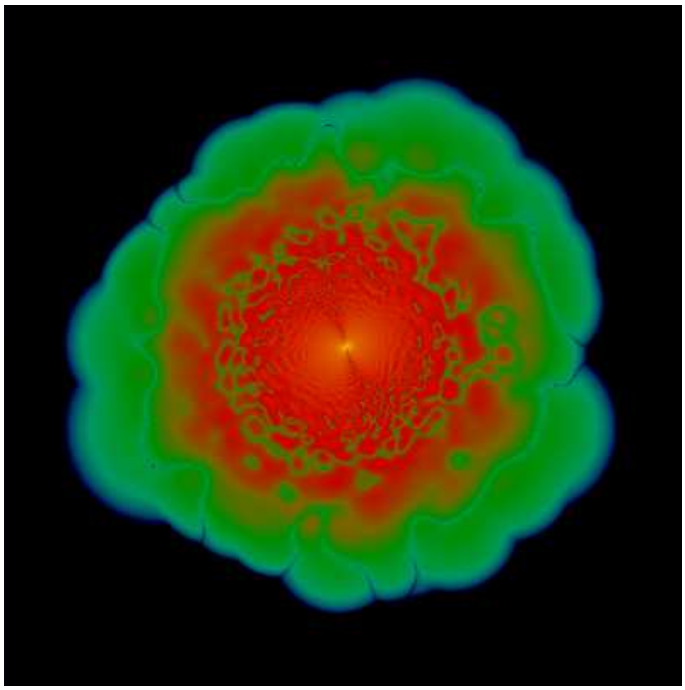

**Figure 3.20:** Image subtractions of the density projections at the start and end of the translating cluster test, The projected density range is $[10^4, 10^{18.6}]\,\mathrm{M}_\odot\ \mathrm{Mpc}^{-2}$.

configuration is subtracted from the final one. This $25\,\mathrm{kpc}$ offset is compatible with the code's accuracy.

## 3.4 Comparing the solvers

As briefly outlined at the beginning of the chapter, the results presented here were embedded in the wider scope of a comparison between Lagrangian (discretising in mass) and Eulerian (discretising in space) modeling techniques (for a detailed discussion see Tasker *et al.*, 2008).

A widely used Lagrangian modeling approach, the Smoothed Particle Hydrodynamics (SPH), has been presented into some detail in section 2.2. Eulerian techniques rely on a computational mesh that fills the simulation volume: physical quantities, characterising the fluid element contained within a mesh cell, are opportunely associated to a point in space (e.g. the center of the cell) and fluxes across the cell surfaces are then computed with a class of algorithms, known as *Riemann solvers*, which provide very fast and accurate solutions, while keeping the errors under tight control.

Therefore, in the Eulerian approach, the size of the cell in the computational mesh is the *resolution* element. In general, the cell size needed to accurately follow the fluid behaviour is small enough to make it almost computationally impossible to fill the whole simulation volume with a unique, very *finely grained*, computational mesh.

Starting with a *coarse* enough grid, the idea is to place *nested* subgrids in the regions of interest, eventually iterating this procedure building a hierarchy of *refinement* levels. The technique that implements this idea is known as *Adaptive Mesh Refinement*: if a certain condition is met within a mesh cell, the space contained within the cells itself is further discretized lying a finer computational mesh and this can happen iteratively.

While in SPH the discretization in mass provides higher resolution in the denser regions of space, the criterion that can trigger higher resolution in AMR calculation is somewhat arbitrary and, in general, allows to place refinements (i.e. to focus with higher resolution) in regions where sudden changes are taking place.

In comparing the behaviour of Eulerian and Lagrangian codes on the suite of tests presented in this chapter we have determined that, in order to reproduce the theoretical behaviour with the same accuracy, both families of solvers need to place the same amount of resolution elements in the regions of interest. Due to the inherent characteristics of the two methods, this is more conveniently achieved by SPH codes when the focus is placed on regions of higher density or in configurations in which a very wide

dynamic range is present. This is often the case in large scale cosmological calculation, and that is one of the main reasons for the success of SPH in this field of research. On the other hand, AMR codes are far more flexible and efficient in tracking sudden and steep changes in arbitrary physical quantities while the inbuilt Riemann solver algorithms makes them a lot more efficient in capturing and modeling sharp shock discontinuities.

The lesson learned with this comparison project is that it is possible to quantitatively establish a level of accuracy that allows a firmly grounded comparison between Eulerian and Lagrangian codes: this results in a rule of thumb saying that an equal amount of resolution elements needs to be placed in the region of interest in order to evaluate the accuracy of the solving algorithms.
Furthermore, the two approaches are somehow complementary in providing trustable solutions in different situations this leading to the recommendation to choose the appropriate tool for the calculation of interest.

Careful, controlled testing such as that detailed in this chapter underpins the entirety of numerical astrophysics. The concepts and ideas developed here are employed throughout the rest of this thesis

# Chapter 4

# The orientation of galaxy dark matter halos around cosmic voids

## 4.1 Abstract

In this chapter we focus on one particular environment, that of voids, underdense regions in the underlying dark matter density field. We develop a method for locating such regions and, in the spirit of the last chapter, demonstrate the accuracy of our method by comparison to a large selection of other void finders available in the literature. We then use our void sample to examine the effect these structures have upon the alignment of galaxies located close to the void walls. After first extracting a set of such voids we use the Millennium N–body simulation to explore how the shape and angular momentum of galaxy dark matter haloes surrounding the largest cosmological voids are oriented. We find that the major and intermediate axes of the haloes tend to lie parallel to the surface of the voids, whereas the minor axis points preferentially in the radial direction. We have quantified the strength of these alignments at different radial distances from the void centres. The effect of these orientations is still detected at distances as large as 2.2 $R_{void}$ from the void centre. Taking a subsample of haloes expected to contain disc–dominated galaxies at their centres we detect, at the 99.9% confidence level, a signal that the angular momentum of those haloes tends to lie parallel to the surface of the voids. Contrary to the alignments of the inertia axes, this signal is only detected in shells at the void surface ($1<R<1.07$ $R_{void}$) and disappears at larger

distances. This signal, together with the similar alignment observed using real spiral galaxies (Trujillo, Carretero & Patiri 2006), strongly supports the prediction of the Tidal Torque theory that both dark matter haloes and baryonic matter have acquired, conjointly, their angular momentum before the moment of turnaround.

## 4.2 Introduction

The angular momentum of a galaxy plays a central role in determining its evolution and final type. However, understanding the origin and properties of the galactic angular momentum has been one of the key problems in astrophysics in the last five decades. The current 'standard' theory for the origin of the angular momentum, within the cosmological framework of hierarchical structure formation, is the tidal–torque theory (hereafter TTT). This theory is based on early ideas from Hoyle, 1951, that suggested that the angular momentum of a galaxy arises from the tidal field of neighbouring galaxies. This idea was further developed and quantified by Peebles (1969); Doroshkevich (1970) and White (1984).

The TTT suggests that most of the angular momentum is gained gradually by the protohaloes during the linear regime of the growth of density fluctuations, due to tidal torques from neighbouring fluctuations. Angular momentum grows linearly with time at this early epoch and saturates when the halo decouples from the expanding background at the moment of turnaround. It is assumed that during this phase the baryonic component follows the dark matter distribution and consequently gains a similar specific angular momentum to that of the halo. A subsequent large collapse factor of the baryonic matter to the centre of the halo will explain the centrifugally supported nature of the galactic discs (Fall & Efstathiou 1980).

To first order, the angular momentum of the haloes results from the misalignment between the principal axes of the inertia momentum tensor ($I_{ij}$) of the matter being torqued and the principal axes of the shear or tidal tensor ($T_{ij}$=-$\partial^2\phi/\partial x_i \partial x_j$) generated by neighbouring density fluctuations. The leading term of the torque is given by $L_i \propto T_{jk}(I_{jj}-I_{kk})$, where $i$, $j$, and $k$ are cyclic permutations of 1, 2 and 3. Several aspects of this picture have been confirmed by a number of studies of the angular mo-

mentum properties of dark matter haloes both analytically (Heavens & Peacock 1988; Catelan & Theuns 1996) and in N–body simulations (Barnes & Efstathiou 1987; Sugerman, Summers & Kamionkowski 2000; Lee & Pen 2000; Porciani, Dekel & Hoffman 2002a,b).

If $\mathbf{I}$ and $\mathbf{T}$ were uncorrelated (as frequently has been assumed under the argument that the former is local and the latter is dominated by the distribution of the large–scale structure) the direction of the angular momentum in the linear regime should be aligned with the intermediate axis of $\mathbf{I}$ (the direction that maximizes the difference between $\mathrm{I}_{jj}$ and $\mathrm{I}_{kk}$). However, Porciani, Dekel & Hoffman (2002b) have found in their simulations that there is a strong correlation between the $\mathbf{I}$ and $\mathbf{T}$ tensors, in the sense that their minor, major and intermediate principal axes tend to be aligned at the protohalo stage. The strong correlation between $\mathbf{I}$ and $\mathbf{T}$ should produce an angular momentum vector of the haloes that is perpendicular to the minor axis of the sheet they are embedded in (i.e. perpendicular to the direction of the maximum compression of the large–scale structure at that point). However, this last correlation, at least at redshift zero, is expected to be very weak (or totally erased) by non–linear effects (such as exchange of angular momentum between haloes) at late times.

From the observational point of view, Trujillo, Carretero & Patiri (2006) have found that the rotation axes of spiral galaxies located on the shells of the largest cosmic voids lie preferentially parallel to the void surface (in agreement with the expectation for the angular momentum of haloes given in the previous picture). The observational relation could be explained then as a consequence of the spin of the baryonic matter still retaining memory of the angular momentum properties of the haloes at the moment of turnaround (Navarro, Abadi & Steinmetz 2004). It is key, consequently, to explore whether the signal is also found in the haloes of cosmological N–body simulations when we mimic the observational technique. If so, this will strongly support our current understanding of how haloes and baryonic matter have acquired, conjointly, their angular momentum.

Together with the orientation of the angular momentum, the alignment of the shape of the galaxy dark matter haloes ($\mathrm{M}<10^{13}h^{-1}\mathrm{M}_{\odot}$) with their surrounding large–scale structure can have important observational consequences. In fact, the shapes of dark

matter haloes can affect the coherence of tidal streams (Sackett 1999), can be related to galactic warps (Ostriker & Binney 1989; Debattista & Sellwood 1999; López-Corredoira, Betancort-Rijo & Beckman 2002) or can affect the distribution of the orbits of satellite galaxies (Holmberg 1969; Zaritsky *et al.* 1997; Sales & Lambas 2004; Agustsson & Brainerd 2006; Yang *et al.* 2006). In addition, infall of material into the haloes is not isotropic but is expected to be through the filaments where the haloes are embedded. Consequently, the orientation of the dark matter haloes within these structures can affect the characteristics of the galaxy properties previously mentioned.

The alignment of massive (group and cluster) haloes ($M>10^{13}h^{-1}M_{\odot}$) with their surrounding large–scale structure has been explored in detail (Splinter *et al.* 1997; Onuora & Thomas 2000; Faltenbacher *et al.* 2002; Kasun & Evrard 2005; Hopkins, Bahcall & Bode 2005; Basilakos *et al.* 2006). These works indicate that the major axes of neighbouring galaxy clusters are aligned. A result that is in agreement with the "Binggeli effect" (Binggeli 1982). The origin of these alignments is still under debate and could be associated to infall of material (van Haarlem & van de Weygaert 1993) and/or tidal fields (Bond, Kofman & Pogosyan 1996). Due to the lack of resolution in previous simulations, it is only now that an exploration of the alignment of the galaxy dark matter haloes has become possible (Bailin & Steinmetz 2005, hereafter BS06; Altay, Colberg & Croft 2006, hereafter ACC06; Patiri *et al.* 2006b, hereafter PA06; Aragon-Calvo *et al.* 2006). These works suggest that the major axis of the haloes lies along the filaments. The quantification of the strength of these alignments is key to studies of strong and weak lensing where the intrinsic distribution and alignment of galaxy shapes plays an important role in interpreting the signal (see e.g. Heavens, Refregier & Heymans 2000; Croft & Metzler 2000; Heymans *et al.* 2006).

The aim of this chapter is to characterise the alignment of both the shape and angular momentum of galaxy dark matter haloes with their surrounding large–scale structure to an unprecedented statistical level using the Millennium simulation (Springel *et al.* 2005). In particular, we will focus our attention on haloes surrounding the largest cosmological voids. Contrary to filaments (which are strongly affected by redshift–space distortion), large cosmological voids are a feature easy to characterise from the observational point of view (Trujillo, Carretero & Patiri 2006). In addition, another

important advantage of the void scheme is that (because of the radial growth of the voids) the vector joining the centre of the void with the galaxy (halo) is a good approximation to the direction of the maximum compression of the large–scale structure at that point.

This naturally generates a framework for exploring the alignments of the shape and angular momentum of the haloes with their surrounding matter distribution. Consequently, our work mimics the observational framework to provide an easy interpretation of current and future observations. The large volume sampled by the Millennium simulation combined with the excellent spatial resolution allows us to conduct this project. This unprecendented statistical power is absolutely crucial if we want to explore signals expected to be very weak like the alignment of halo angular momentum and the large–scale structure.

This chapter is structured as follows: the next section provides a description of the Millennium simulation itself, the void and halo samples used, and details of how the shapes and spins were measured. Following that, Section 4.4 describes our results and we discuss our findings in Section 4.5.

## 4.3 Numerical simulation

### 4.3.1 N–body simulation

The main simulation we have used for this study is the *Millennium Simulation* of Springel et al (2005). This employs $2160^3$ dark matter particles each of mass $8.6 \times 10^8 h^{-1}\mathrm{M}_\odot$ within a comoving box of side $500h^{-1}\mathrm{Mpc}$. This simulation was performed in a $\Lambda$CDM universe with cosmological parameters: $\Omega_\Lambda = 0.75, \Omega_M = 0.25, \Omega_b = 0.045, h = 0.73, n = 1$, and $\sigma_8 = 0.9$, where the Hubble constant is characterised as $100h\mathrm{kms}^{-1}\mathrm{Mpc}^{-1}$. These cosmological parameters are consistent with recent combined analyses from *WMAP* data (Spergel *et al.* 2003) and the 2dF galaxy redshift survey (Colless *et al.* 2001), although the value for $\sigma_8$ is a little higher than would perhaps have been desirable in retrospect. The spatial resolution is $5h^{-1}\mathrm{kpc}$ everywhere inside the simulation volume.

### 4.3.2 Void and halo samples

To explore the effect of the large–scale structure on the orientation of the dark matter haloes, we use a technique similar to the one adopted in analysing the orientation of disc galaxies in real observations (Trujillo, Carretero & Patiri 2006). To this aim we need, first, to find and characterise the radius of the large voids in the simulation. To speed up the process of finding the voids, we used as an initial guess for the position of the void centres the position of the most underdense particles in the box. To do this, for every dark matter particle in the Millennium Simulation we have estimated the local density by using a standard (Monaghan & Lattanzio 1985; Hernquist & Katz 1989) smoothing kernel averaging over 32 neighbours. We produced a list of the most underdense particles and then radially sorted surrounding particles in distance from these points. In this way the radius of a volume underdense by a factor of 10, centred on the most underdense particle, was calculated. All particles with densities less than 0.035 of the cosmic mean and further than $2h^{-1}\mathrm{Mpc}$ away from an even less dense particle were tried as prospective centres. After cleaning this catalogue by removing those positions that lay within a larger void and limiting the size to be larger than $5h^{-1}\mathrm{Mpc}$ in radius, this technique produced 3024 potential void centre candidates. We estimate that this catalogue of potential void centres is greater than $99\%$ complete, given that we tried over 200,000 random centres but only found 2 additional voids in the last 50,000 (i.e. voids with central densities close to our limit of 0.035).

Once a list of initial positions for searching for voids in the simulation had been created, we used these positions to search for the maximum spheres that are empty of haloes with mass larger than a given value. To conduct this search we follow an algorithm based on a modification of the one presented in Patiri *et al.* (2006a). The haloes were identified using a minimal spanning tree that links together particles with density exceeding 900 times the background density (Thomas *et al.* 1998). This is to focus on the core properties. In our case, we have used all haloes with masses larger than $8.6\times10^{11}h^{-1}\mathrm{M}_{\odot}$ (i.e. those haloes with more than 1000 particles). Using this mass cut we are selecting haloes that contain galaxies with stellar masses similar to the ones used in the observational data. To characterise the final position of the void centres and their radii, we populate a sphere of radius R=5 $\mathrm{h}^{-1}$ Mpc, centered on each initial

position, with 2000 random points. For every point in this sphere, we estimate the position of the closest 4 haloes lying in geometrically "independent" octants. Then we built the sphere defined by these 4 haloes. This is repeated for all the 2000 random points. As a characterization (position and radius) of the void we choose the biggest empty spherical region generated in the previous step. It is important to stress that the position of the void defined in this way normally does not match the position of the initial guess.

To match the observations we select only those voids whose radius (as measured by the largest sphere that is empty of haloes greater than a given mass) is larger than 10 $h^{-1}$ Mpc. This cut produces 2932 voids in our box with a median radius of 14 $h^{-1}$ Mpc. To explore the alignments of the haloes we have concentrated only on haloes with masses $8.6\times10^{11}h^{-1}\mathrm{M}_{\odot}$ <M< $8.6\times10^{12}h^{-1}\mathrm{M}_{\odot}$(i.e. we restrict the sample to galaxy–sized haloes) and located within shells beyond the surface of the voids.

In addition, we have also created a subsample of haloes which contain a disc–dominated galaxy at their centre. These haloes are expected to have had a relatively 'quiet' life and have suffered smaller non–linear effects after turnaround such that their spin properties should remain matched to those of the baryonic matter. To select these haloes we have used the semianalytic galaxy catalogue of Croton *et al.* (2006). We have created the subsample by selecting the brightest dominant galaxy within 200 $h^{-1}$ kpc of our halo centre. We then select those haloes where the semianalytic code indicates that there is a galaxy brighter than $\mathrm{M}_K$<-23 mag that has a bulge–to–total (B/T) ratio 0<B/T<0.4 (i.e. a Milky–Way like disc galaxy).

### 4.3.3 Void finder comparison

In order to test the veracity of our void detection and extraction algorithm we took part in a large void finder comparison study undertaken by Colberg *et al.* (2008). In order to demonstrate that our finder is indeed working we show the relevant plots below.

Colberg *et al.* (2008) used the Millennium simulation (Springel *et al.* 2005) and a matched $z = 0$ galaxy catalogue, created using a semi–analytical galaxy formation model (Croton *et al.* 2006). Within the Millennium simulation volume they located

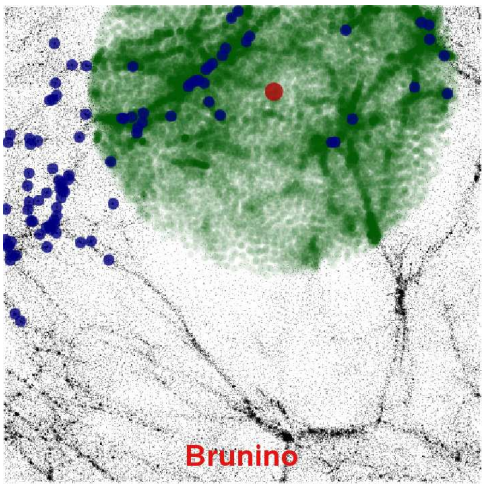


**Figure 4.1:** A slice of thickness $5\,h^{-1}$ Mpc through the centre of the region extracted from the Millennium simulation. The image shows the dark matter distribution in the central $40\,h^{-1}$ Mpc region. Void galaxies (within any void, not just the largest one) are superimposed on the dark matter distribution as blue circles. The locations of the largest void (with dark matter particles inside the void marked green), its centre (red circle), and all void galaxies found.

a $60\,h^{-1}$ Mpc region centred on a large void and extracted the coordinates of the 12,528,667 dark matter particles contained within it. This subvolume had a mean density which is lower than the cosmic mean, corresponding to an overdensity $\delta = \rho/\bar{\rho} - 1 = -0.28$.

They also extracted a list of the 17,604 galaxies together with their BVRIK dust corrected magnitudes (down to B=-10) that are present in the semianalytic catalogue of Croton *et al.* (2006) within this volume and the 4,006 dark matter halos present in the subfind catalogue (a clean spherical overdensity based catalogue) with masses greater than $10^{11}\,h^{-1}\,\mathrm{M}_{\odot}$.

Figure 4.1 shows a $5\,h^{-1}$ Mpc thick slice through the dark matter distribution in the central $40\,h^{-1}$ Mpc region. Void galaxies (within any void, not just the largest one) are superimposed on the dark matter distribution as blue circles. The locations of the largest void (with dark matter particles inside the void marked green), its centre (red circle), and all void galaxies found. The largest dark matter halo in this region only has a mass of $1.75 \times 10^{12}\,h^{-1}\,\mathrm{M}_{\odot}$, so filaments in these images correspond only to the least massive filaments in standard slices through the dark matter distribution as seen in, for example, Springel *et al.* (2005). Furthermore, the slice contains a total of 145,194 dark matter particles, equivalent to an overdensity of $\delta = -0.77$.

It is clear from the following figures that our void finder obtains results essentially

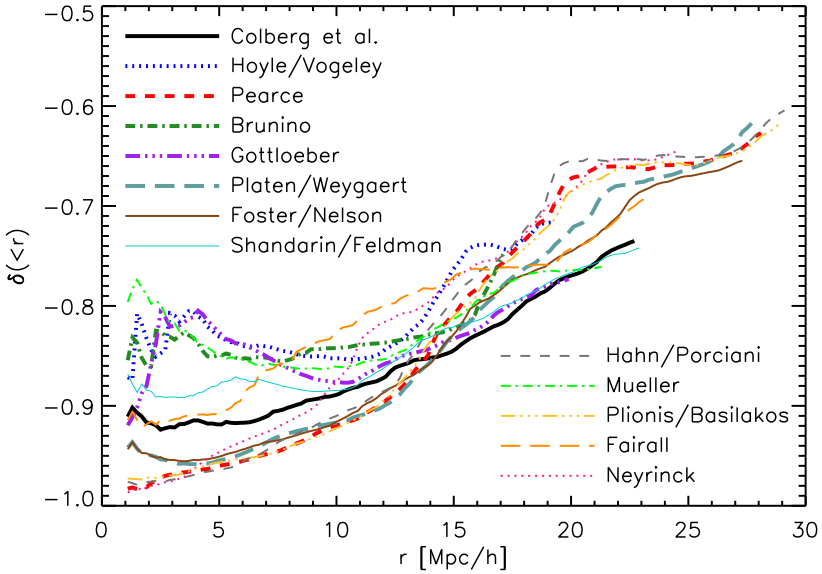


**Figure 4.2:** Radially averaged dark matter density profiles of the largest void in each of the void catalogues found by the groups involved in the study of Colberg *et al.* 2008. For each void finder the profile extends out to the largest radius that can be studied, given the size of the volume. See main text for more details.

indistinguishable from other finders available in the literature.

### 4.3.4 Halo shapes and spins

To characterise the orientation of the haloes we have determined the orientation of their principal axes and their angular momentum vectors. The principal axes of the halo mass distribution are measured by diagonalising the inertia tensor,

$$I_{ij} = \frac{1}{N_p} \sum_{k=1}^{N_p} m_k x_{k,i} x_{k,j} \tag{4.1}$$

where the sum is over all the particles in the halo $N_p$, and the coordinates are defined with respect to the centre of mass of the halo of mass $M_h$. The resulting eigenvalues $M_h a^2/5$, $M_h b^2/5$, and $M_h c^2/5$ are sorted by size, in descending order. The eigenvectors give the directions of the principal axes.

The angular momentum vector of the halo is given by:

$$\mathbf{L} = \sum_k m_k \mathbf{r_k} \times \mathbf{v_k} \tag{4.2}$$

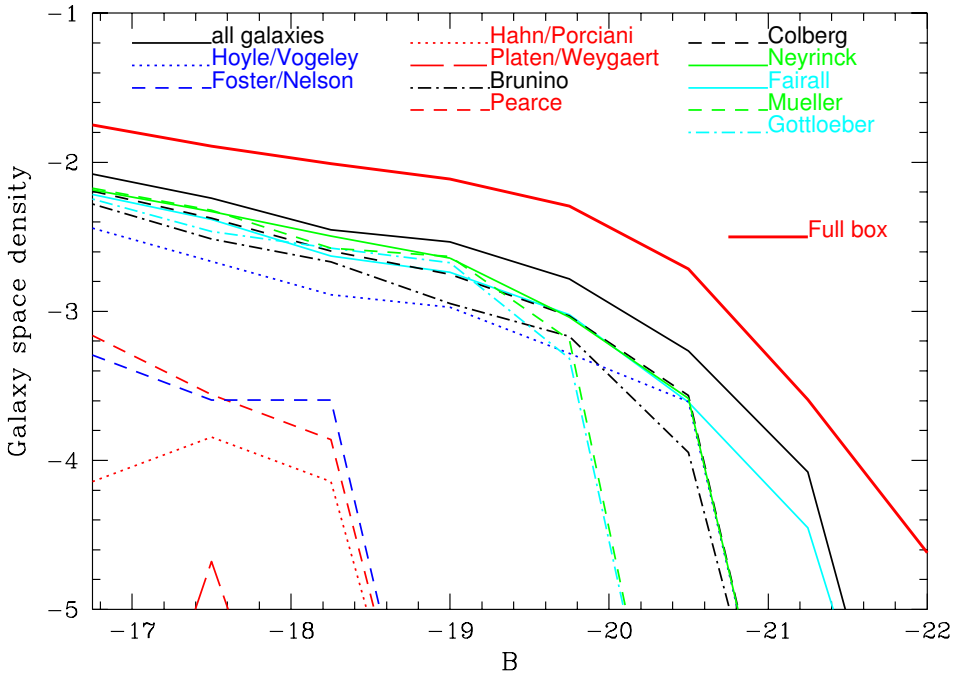


**Figure 4.3:** Space density of galaxies ($h^3$/Mpc$^3$/mag) as a function of dust corrected $M_B$ for galaxies in the volume under consideration and in the catalogues of those void finders which identify galaxies inside voids. For purposes of comparison, the luminosity function of the full simulation volume is also given. Each void finder luminosity function is corrected for the volume occupied by the relevant void sample.

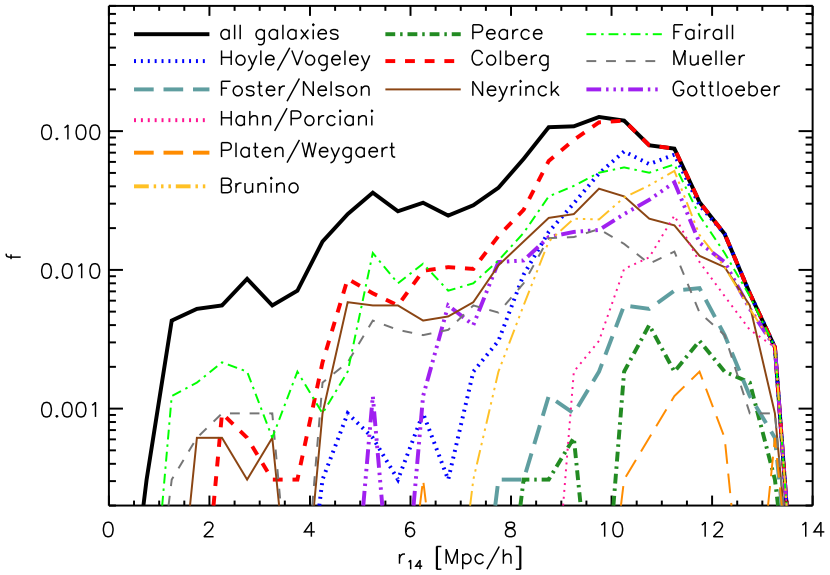


**Figure 4.4:** Distributions of the local densities of the galaxies in the results of those void finders that identity void galaxies. The local density is expressed via $r_{14}$, which for each galaxy gives the radius of the sphere around the galaxy that contains $10^{14}\,h^{-1}\,\mathrm{M}_\odot$. For comparison purposes, the distribution of the full galaxy sample is also shown.

where the sum is again over all the particles in the halo and $\mathbf{r_k}$ and $\mathbf{v_k}$ are the position and velocity of each particle relative to the centre of mass of the halo.

The uncertainty in the position of the inertia axes and of the angular momentum has been evaluated by comparing these quantities in the same haloes in two different runs that differ by a factor of 20 in resolution. We found that we can measure the orientation of the angular momentum vector with an uncertainty (as provided by the full width half maximum of the distribution) of $\sim$14$^\circ$ when the number of particles in the (low resolution) halo is larger than 1000. The uncertainties in the inertia axes are 13$^\circ$ for the semimajor and semiminor axes and 20$^\circ$ for the intermediate axis.

Once the angular momentum and the inertia vectors are evaluated, we estimate the cosine of the angle between those vectors and the vector joining the centre of the void with the centre of the halo $\mathbf{R}$:

$$\mu = \cos\theta = \left(\frac{\mathbf{R}\cdot\mathbf{V}}{|\mathbf{R}||\mathbf{V}|}\right) \tag{4.3}$$

## 4.4 Results

Fig. 4.5 shows the probability density distribution P($\cos\theta$) of the cosine of the angles between the inertia axes (and the angular momentum) and the vector joining the centre of the void to the centre of the halo. We show the results for two different shells: the shell located at the surface of the void with a width of 5% of the radius (i.e. 1 $R_{void}$<R<1.05 $R_{void}$), and a shell located well beyond the surface of the void at 1.2 $R_{void}$<R<1.4 $R_{void}$. We do this to highlight the effect of moving farther away from the void surface. The dashed line in this figure corresponds to the probability distribution of randomly distributed angles (i.e. P($\cos\theta$)=1).

To the best of our knowledge there is no theoretical prediction for the probability density distribution of the angles between the inertia axes and the vector joining the centre of the void to the centre of the halo. For this reason, we have used the following simple analytical expression motivated by the planar symmetry of the problem to quantify the strength of the signal:

$$P(\mu)d\mu \propto \frac{pd\mu}{(1+(p^2-1)\mu)^{3/2}} \tag{4.4}$$

If p=1, we obtain the null hypothesis (i.e. P($\cos\theta$)=1). Values of p>1 imply that the inertial axis tends to be aligned with the surface of the shell, whereas p<1 implies that the axis tends to be perpendicular to the void surface. This simple analytical expression produces good fits to the observed distribution with reduced $\tilde{\chi}^2 \lesssim 1$ in most of the cases. The results of our fits are summarized in Table 4.1.

We find significant alignments of the inertia axes within the shells of the voids. The major axes of the dark matter haloes tends to lie parallel to the surface of the voids (i.e. there is an excess of haloes with large values of $\theta$). For the minor axis the alignment is contrary to the major axis, there is an excess of haloes with the minor axis oriented in the radial direction of the voids. The intermediate axis also tends to lie parallel to the surface of the voids, although the signal is not as strong as in the case of the major axis. As expected, the signal declines in all the cases as the distance from the centre of the voids is increased, although this decline is slow: we still detect a weak signal of alignments of the major and minor axes at distances as large as $\sim$2.2 $R_{void}$ from the void centre. The distribution of angular momentum vectors, however, is compatible with a random orientation.

To test the reliability of our results we have repeated our analysis locating the centres of the voids at random positions within the whole volume of the simulation. As expected, we recovered for all the cases a signal which is compatible with the null hypothesis. To run this test we have used exactly the same number of random centres as the number of voids we have. The number of haloes and their distances to the centres of these 'fake' voids are similar in this control experiment to the real case.

As stated in the introduction, any signal of alignment in the angular momentum of the haloes is expected to be erased after the turnaround by non-linear effects. For this reason, if this signal is still present nowadays it should be found in haloes which have had the 'quietest' lives since turnaround. To explore this, we have repeated the same analysis as before but this time using the subsample of haloes with a disc-dominated galaxy at their centre. The results are shown in Fig. 4.6 and the strength of the signal is quantified in Table 4.1.

Contrary to the result obtained using the full sample of haloes, the angular momentum vectors of the haloes with a disc–dominated galaxy at their centre tend to lie parallel to the surface of the void. To test the reliability of this signal we have run different statistical tests: the departure of the average (Avni & Bahcall 1980) of $\cos\theta$ from 0.5 (i.e. the expected value in the null hypothesis case) and the Kolmogorov–Smirnov (K-S) test. Both tests reject the null hypothesis at the 99.8% level. Our results are robust to changes in the ratio B/T ranges selected (i.e. we still find a significant signal for the alignment of the angular momentum including haloes with galaxies with B/T$<$0.6). In addition, we have also checked that including those haloes contained in our list of voids with R$<$10 $h^{-1}$ Mpc do not alter (within the error bars) our results. This is as expected beacause almost all of our initial void centres produce voids larger than 10 $h^{-1}$ Mpc in radius.

It is worth noting that the maximum signal is found when we select a shell of width 1 $R_{void}$<R<1.07 $R_{void}$. For this case, the null hypothesis is rejected at 99.9%. On the other hand, the inertia axes show the same trends in this subsample as in the previous case using all the haloes.

To characterize the strength of the alignment of the angular momentum we have followed two approaches. We have used (as before) equation (4.4) and, secondly, we have compared our result with the theoretical prediction for this quantity from Lee (2004) within the framework of the TTT. The strength of the intrinsic galaxy alignment of the galaxies with local shear at the present epoch is expressed as the following quadratic relation (Lee & Pen 2002):

$$< L_i L_j >= \frac{1+c}{3}\delta_{ij} - c\widehat{T}_{ik}\widehat{T}_{kj}, \tag{4.5}$$

where $\mathbf{L}$ is the halo angular momentum (spin) vector and $\widehat{\mathbf{T}}$ is the rescaled traceless shear tensor $\mathbf{T}$ defined as $\widehat{T}_{ij}$=$\widetilde{T}_{ij}/|\widetilde{\mathbf{T}}|$ with $\widetilde{T}_{ij}\equiv T_{ij} - Tr(\mathbf{T})\delta_{ij}/3$, and c is a correlation parameter introduced to quantify the strength of the intrinsic shear-spin alignment in the range of [0,1]. To estimate c we have used the analytical approximation suggested in Lee, Kang & Jing (2005):

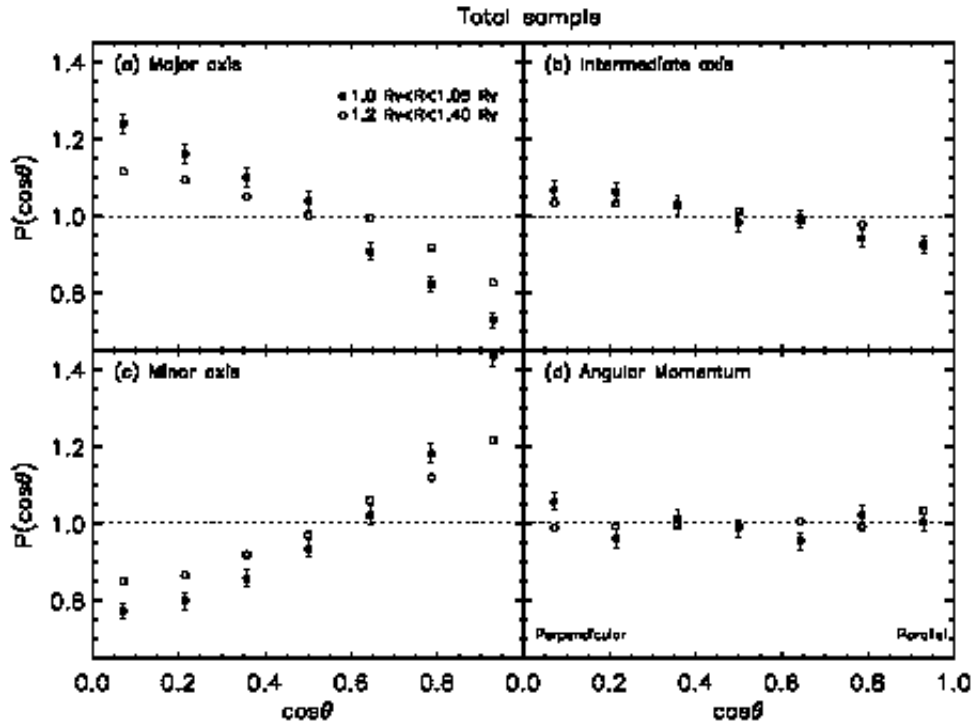


**Figure 4.5:** Probability density distribution of the cosine of the angles $\theta$ between the inertia axes (and angular momentum) and the vector joining the centre of the voids with the halo centres. The error bars on each bin is the Poissonian error and (to avoid confusion) are only plotted for the innermost shell bins. The null hypothesis (i.e. a sine distribution) is represented by the dashed line.

$$P(\mu) = \left(1 - \frac{3c}{4}\right) + \frac{9c}{8}(1 - \mu^2) \tag{4.6}$$

The values of the parameter c we obtain in the different shells are summarized in Table 4.1. When c=1 the strength of the galaxy alignment with the large-scale distribution is maximum, whereas c=0 implies galaxies are oriented randomly. In the inner shell, we measure in this case c=0.151$\pm$0.046. It is worth noting that the value of c measured in this work is a lower limit of the true value because it has been evaluated without any attempt to correct for the smoothing produced by the uncertainty in measuring the angular momentum vector of the haloes. Consequently, the strength (and statistical significance) of the observed alignment should be higher. To quantify this effect, we have re–estimated c again but this time using the theoretical prediction convolved with our error function in measuring the angular momentum. After fitting the convolved function to the data, we obtain c=0.158$\pm$0.045.

**Table 4.1:** The strength of the alignments on the different shells. To measure the alignment of the inertia axes we have used the parameter p (p=1 in the null case), and c (Lee 2004) in the case of the angular momentum (c=0 in the null case).

| Shell $R_{void}$ Units | Maj. A. p | Int. A. p | Min. A. p | A. M. p | A. M. c | Number of Haloes |
|---|---|---|---|---|---|---|
| | | | Total Sample | | | |
| 1.00 <R<1.05 | 1.218±0.012 | 1.061±0.011 | 0.778±0.008 | 1.007±0.010 | 0.004±0.026 | 13128 |
| 1.05 <R<1.10 | 1.165±0.014 | 1.060±0.013 | 0.800±0.010 | 0.994±0.012 | -0.014±0.032 | 8644 |
| 1.10 <R<1.20 | 1.150±0.009 | 1.057±0.008 | 0.820±0.007 | 0.992±0.008 | -0.020±0.020 | 21567 |
| 1.20 <R<1.40 | 1.111±0.005 | 1.040±0.005 | 0.863±0.004 | 0.989±0.005 | -0.033±0.012 | 60908 |
| 1.40 <R<1.80 | 1.070±0.003 | 1.021±0.003 | 0.914±0.002 | 0.989±0.003 | -0.027±0.007 | 200201 |
| 1.80 <R<2.60 | 1.030±0.001 | 1.011±0.001 | 0.959±0.001 | 0.995±0.001 | -0.014±0.004 | 707760 |
| 2.60 <R<3.20 | 1.011±0.001 | 1.003±0.001 | 0.985±0.001 | 0.998±0.001 | -0.004±0.002 | 1301720 |
| | | | Disc-Dominated subsample | | | |
| 1.00 <R<1.05 | 1.172±0.021 | 1.056±0.019 | 0.803±0.015 | 1.062±0.019 | 0.151±0.046 | 4212 |
| 1.05 <R<1.10 | 1.156±0.026 | 1.040±0.023 | 0.812±0.019 | 0.994±0.022 | 0.013±0.059 | 2587 |
| 1.10 <R<1.20 | 1.148±0.017 | 1.035±0.015 | 0.837±0.012 | 1.003±0.015 | 0.018±0.038 | 6366 |
| 1.20 <R<1.40 | 1.098±0.010 | 1.036±0.009 | 0.875±0.008 | 0.991±0.009 | -0.029±0.023 | 17553 |
| 1.40 <R<1.80 | 1.057±0.005 | 1.021±0.005 | 0.920±0.005 | 0.987±0.005 | -0.028±0.013 | 56883 |
| 1.80 <R<2.60 | 1.025±0.002 | 1.012±0.002 | 0.960±0.002 | 0.994±0.003 | -0.013±0.006 | 228198 |
| 2.60 <R<3.20 | 1.013±0.002 | 1.006±0.002 | 0.981±0.002 | 0.999±0.002 | -0.002±0.005 | 370409 |

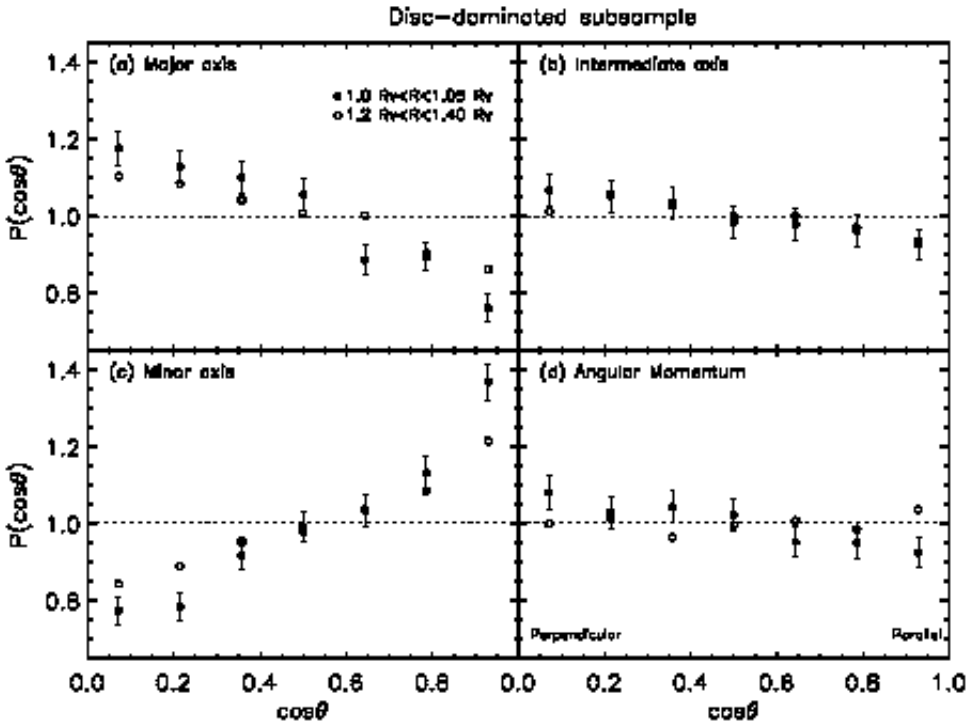


**Figure 4.6:** Same than in Fig. 4.5 but this time using only haloes which contain a disc–dominated galaxy at their centres. Note that using this halo subsample the angular momentum vector tends to lie parallel to the surface of the void.

## 4.5 Discussion

In this chapter, we have shown that when haloes are selected in order to contain a Milky–Way like disc galaxy at their centres the angular momentum of the dark matter halo is oriented preferentially parallel to the surface of the voids. Observationally, the same alignment is detected using the baryonic matter (Trujillo, Carretero & Patiri 2006). These two pieces of information are in agreement with the TTT prediction that both the dark and the baryonic matter component have conjointly acquired their angular momentum before the moment of the turnaround. Interestingly, the signal detected in the real observation c=$0.7^{+0.1}_{-0.2}$ is higher than the one found in the simulations c=0.151$\pm$0.046. This is to be expected taking into account that the signal in the dark matter haloes should be erased by non–linear effects such as exchange of angular momentum between the haloes. Future work, consequently, should explore the strength of the alignment of the haloes at the moment of turnaround. At that early epoch the strength of the signal should be as strong as the one measured using the baryonic component. Porciani, Dekel & Hoffman (2002b) shows hints that this should be the case by comparing the relation between the halo spin and the linear shear tensor at different redshifts from z=50 to z=0.

We have compared our work with previous analysis of the alignment of the inertia axes and angular momentum with their surrounding large–scale structure using different simulations. We concentrate first on the alignment of the angular momentum: using the void framework, neither Heymans *et al.* (2006) nor PA06 have found a signal of the alignment of the angular momentum within the shell of the voids. Their results are easily understood taking into account that no preselection of the haloes was done in either of these works and that they explored the signal in just one shell of width 4 $h^{-1}$ Mpc. In fact, if we mimic their analysis we find c=-0.014$\pm$0.012 (p=0.996$\pm$0.005), in agreement with their findings. In the same shell, selecting those haloes with 0<B/T<0.45 produces c=0.030$\pm$0.021 (p=1.012$\pm$0.008). This is a factor of 5 weaker than the signal we find in the closest shell to the void surface. As we have seen in this work, the signal is only significant at the void surface, consequently, taking a wide shell can mask it. In the particular case of Heymans *et al.* (2006) their mass resolution limit could be another source of concern, since it is a factor of $\sim$10 worse than the present

simulation.

Comparison with other work is more complicated since the analysis of the alignments is done using a different scheme. BS06 measure the alignment of the angular momentum along filaments. Interestingly, they found that the angular momentum of galaxy mass haloes shows a weak tendency to point along filaments, while those of group and cluster mass haloes show a very strong tendency to point perpendicular to the filaments. The significance and strength of their signal in terms of the c parameter is, however, not quantified. Consequently, the agreement between ours and their work can be done only qualitatively. Porciani, Dekel & Hoffman (2002b) explored the alignment of massive haloes (M>$10^{13}h^{-1}$M$_{\odot}$) between their $final$ spin and the $initial$ shear tensor at the halo position. They found c=0.07$\pm$0.04. The mass regime explored by these authors and their comparison between an initial and a final property of the haloes prevents us making a direct comparison between their and our measurements of the c parameter. Finally, in a recent paper, Aragon-Calvo *et al.* (2006), using galaxy mass haloes find that the strength of alignment of their spins in walls is c=0.13$\pm$0.02. This is in excellent agreement with the value reported in this chapter.

If we focus our attention on the alignment of the inertia axes, we find that our results are in good agreement with those of BS06, ACC06 and PA06. All these authors find that the tendency of the minor axis to lie perpendicular to large–scale filaments is the strongest of the alignments. It is interesting to note that the strength of these alignments seems to be dependent on the mass of the haloes, being stronger for the most massive (cluster–sized) ones. BS06 and ACC06 suggest that the different strength could be related to fact that most massive haloes receive a larger infall of matter from filaments. This could also help to explain the tendency of the angular momentum of the most massive haloes to be perpendicular to the filaments. In this sense, the cluster mass haloes would acquire most of their current angular momentum from major mergers along the filaments, whereas the angular momentum of the galaxy mass haloes will still have memory of the initial tidal fields.

The alignment of the haloes with their local large–scale structure is not only of interest to constrain models of galaxy formation, it could also be relevant to explain other observational features. For example, the tendency of satellite galaxies to avoid orbits

that are coplanar with their host spiral galaxies (know as the ”Holmberg effect”) found in observations (Holmberg 1969; Zaritsky *et al.* 1997; Sales & Lambas 2004, but see Agustsson & Brainerd 2006) and in simulations (Zentner *et al.* 2005; Libeskind *et al.* 2007). This could be due to the preferential accretion of satellites along filaments, that we have seen are preferentially aligned with the major axis of the host halo.

Finally, it is worth pointing out the potential importance of the alignments we have discussed here to strong and weak lensing studies. In particular, these alignments could contribute to the weak lensing signal producing a shear–ellipticity correlation (Hirata & Seljak 2004). The degree of contamination that these alignments will produce in the weak lensing surveys should be explored in future work.

Voids are one extremum of the range of large scale environments within which galaxies can reside. These environments range from underdense voids to highly overdense galaxy clusters which may contain many thousands of galaxies. In the next chapter we utilise large simulations covering several of such environments and attempt to quantify what effect this has on galaxy properties.

# Chapter 5

# Large Scale Structure environmental effects on galaxy formation

One of the main projects carried out by the Virgo Consortium in recent years has been the Millennium Simulation (Springel *et al.* 2005) in which a comoving volume of 500 $h^{-1}$Mpc has been evolved to present day (i.e. $z = 0$), employing of the order of $10^{10}$ tracers (particles) to model the gravitational evolution of the non-collisional DM component. In cosmological calculations of structure formation it is crucial to make sure that the simulated volume is large enough to allow fluctuations in the density field on the linear scale of the box to remain in the linear regime down to the time when the simulation is stopped. This requirement is met by the Millennium run, which is therefore able to follow the formation of cosmic structures spanning an enormous dynamical range (the gravitational softening, $\epsilon \sim 5h^{-1}$ kpc). This resulted in a very computationally intensive calculation and it wouldn't have been possible, due to computational resource limitation, to perform the same calculation both keeping the same accuracy in mass resolution and also accounting for the physics of the baryonic component. A trade-off has been adopted in the "Millennium with Gas" project, at the price of a coarser resolution for the baryonic component (Hartley *et al.* 2008, Gazzola, PhD thesis).

In order to overcome this limitation, *Semi-Analytical* techniques have been developed (White & Frenk (1991), Kauffmann, White & Guiderdoni (1993), Cole *et al.* (1994, 2000), Somerville & Primack (1999), Baugh (2006)): in this approach, the evolution

of baryons within DM halos are followed by means of analytical prescriptions. The formation history of DM halos (identified within the parent simulation) are organized so that the *merger trees* allow us to follow the hierarchical formation processes, driven by gravity, that result in present day DM halos. Semi-Analytical Models (hereafter SAMs) of galaxy formation can then use the DM halos merger trees generated from an N-body simulation and produce galaxy populations that can be then compared with observations.

Exploiting the Millennium Simulation, several authors have carried out Semi-Analytical studies of galaxy formation: for example, the SAMs used in Bower *et al.* (2006), Croton *et al.* (2006) and Font *et al.* (2008) produced galaxy populations in the MILLENNIUM volume. Also De Lucia *et al.* (2006) applied their SAM to same simulation results.

## 5.1 Sampling different environments in the LSS

Taking into account baryonic physical processes in large calculations of structure formation generates a demand for computational resources difficult to meet with present day facilities. It has been shown by Theuns *et al.* (1998) that resolving the Jeans Mass in the Intergalactic Medium (IGM) after the re-ionization epoch is a necessary requirement for numerical calculations to be able to model the high redshift $Ly-\alpha$ forest: this translates in a gas particle mass $\sim 10^6 M_{\odot} h^{-1}$ which is computationally unfeasible for large scale calculations such as the Millennium run. On the other hand, following a galaxy formation scenario in a box of linear size $L \lesssim 100 h^{-1}$ Mpc can not lead to predictions on $z = 0$ galaxy populations: density fluctuations on the scale of the box become non-linear long before the desired end of the calculation, therefore leading to non reliable results (see Bagla & Ray 2005; Gelb & Bertschinger 1994; Sirko 2005). The *re-simulation* technique has been developed in the past two decades in order to overcome these limitations: starting from a parent simulation of a large cosmological volume it is possible to identify regions of interest in the end state of the simulation (let's assume this is $z = 0$). Particles belonging to these regions can then be traced back to the initial conditions (hereafter ICs) and, allowing a padding zone for safety,

the Lagrangian region of interest in the ICs can be "zoomed" in. The number of particles in these regions is increased, while the resolution in the external volume can be degraded using a coarser sampling in mass of the continuum (see Tormen, Bouchet & White 1997, for example). Using the re-simulation technique and the MILLENNIUM run as a parent simulation, the Virgo Consortium started a project called *Galaxies-Intergalactic Medium Interaction Calculation* (GIMIC), aimed at re-simulating a series of five LSS environments including baryonic physics and with a resolution close to the *Jeans* mass in the IGM soon after the re–ionization epoch. The project is presented in Crain *et al.* (2009), where details of the calculations can be found. For the present work, we performed the gravity-only version of the GIMIC calculations at intermediate mass resolution. We then produced the *merger trees* for halos and substructures we identified in our simulations, passing these as inputs to the SAM by De Lucia *et al.* (2006); De Lucia & Blaizot (2007). We then analyzed the galaxy catalogues produced by the SAM, and the corresponding galaxy merger trees, in order to identify the effects (if any) of the LSS on the processes of galaxy formation.

### 5.1.1 Initial conditions and numerical calculations

In the GIMIC project, the LSS formed in the MILLENNIUM volume has been sampled in order to identify regions spanning a wide range of environments from underdense *voids* to rich *galaxy clusters*. This resulted in selecting five roughly spherical regions, whose overdensities at $z = 1.5$ are $(-2, -1, 0, +1, +2)$ times the root-mean-square deviation, $\sigma$, from the cosmic mean on a scale of $\sim 20h^{-1}$Mpc at $z = 1.5$. Four out of five spheres have a comoving radius of $18h^{-1}$ Mpc, while the $\sigma = +2$ regions was chosen to be centered on a rich cluster, thus requiring a spherical Lagrangian region of radius $25h^{-1}$Mpc to be followed during the calculation.

The corresponding Lagrangian regions in the ICs have then been resampled using a higher number of particles. In the original MILLENNIUM run, DM (*low resolution*) particles have a mass $m_{DM} = 8.6 \times 10^8 h^{-1} M_\odot$. Here two sets of ICs have been generated at *intermediate* mass resolution $m_{DM} = 6.46 \times 10^7 h^{-1} M_\odot$ and *high* mass resolution $m_{DM} = 8.08 \times 10^6 h^{-1} M_\odot$. Outside these *zoomed* regions, the MILLENNIUM volume has been resampled with a multi-mass particle distribution. Moving out

| Region | x [$h^{-1}$Mpc] | y [$h^{-1}$Mpc] | z [$h^{-1}$Mpc] | Comoving radius [$h^{-1}$Mpc] | $N$ (int. res) |
|---|---|---|---|---|---|
| $-2\sigma$ | 153.17 | 347.90 | 424.81 | 18 | $2.23 \times 10^7$ |
| $-1\sigma$ | 387.91 | 316.48 | 113.46 | 18 | $2.80 \times 10^7$ |
| $0\sigma$ | 271.94 | 108.29 | 107.45 | 18 | $3.44 \times 10^7$ |
| $+1\sigma$ | 179.51 | 379.22 | 196.64 | 18 | $4.30 \times 10^7$ |
| $+2\sigma$ | 233.10 | 139.30 | 387.38 | 25 | $1.24 \times 10^8$ |

**Table 5.1:** Parameters for the five GIMIC regions. Columns 2-5 give the location (in Millennium Simulation coordinates) and the nominal comoving radius of the regions at $z = 1.5$. The following column show the number of dark matter particles within the zoomed region of the simulation.Adapted from Crain *et al.* (2009).

of the high resolution region 8 different boundary layers have been defined and each of them has been populated with a smaller number of larger particles. In this way, the Lagrangian representation of the continuum becomes coarser and coarser moving away from the region of interest. It is not possible to follow the dynamics of such a system, but a good accuracy in its tidal force contribution to the high-resolution particles can be obtained, thus also dramatically reducing the overall computational requirements. This *zooming* technique, by introducing a larger amount of particles in the regions of interest, modifies (increase) the Nyquist frequency in the simulated box. It has then become necessary to take into account the extra power associated to higher modes. To do this, the same power spectrum used in the generation of the MILLENNIUM run ICs was adopted up to its characteristic Nyquist frequency while the power corresponding to the extra modes introduced in these calculation have been obtained by means of CMBFAST(Seljak & Zaldarriaga 1996). The Zel'dovich displacement field was then applied (see Power *et al.* 2003, as an example). A detailed discussion on the procedure used for the selection of the GIMIC regions and on the generation of the initial conditions can be found in Crain *et al.* (2009). It is worth noticing that this strategy allows the hi-resolution regions to be evolved down to $z = 0$ without worring about finite box size effects. Fluctuations on the scale of the MILLENNIUM volume are still described by linear theory and their contribution is taken into account in the GIMIC calculations.

The GIMIC simulations adopt the same cosmological parameters as the MILLENNIUM simulation: $\Omega_{\rm m} = 0.25$, $\Omega_\Lambda = 0.75$, $\Omega_{\rm b} = 0.045$, $n_{\rm s} = 1$, $\sigma_8 = 0.9$, $H_0 = 100\ h\ {\rm km\ s^{-1}\ Mpc^{-1}}$, $h = 0.73$, consistently with the WMAP-1st year data (Spergel *et al.* 2003), and with the *2dfGRS* (Colless *et al.* 2001) .

In our production runs we evolved the *intermediate* mass resolution ICs, limiting ourselves at following the non-collisional CDM component and neglecting baryonic processes. In our calculations, following Crain *et al.* (2009), we used a $1024^3$ mesh for the PM estimate of the gravitational potential and adopted a gravitational softening length initially fixed in comoving space, but becoming fixed in physical space at $z = 3$:

$$\epsilon_{\rm com}(a)' = \min(\epsilon_{\rm com}, \epsilon_{\rm phys}^{\rm max}/a) \tag{5.1}$$

The softening was chosen such that at $z = 3$, it was fixed at $\epsilon_{\rm phys}^{\rm max} = (1.0)h^{-1}$ kpc which is smaller then the limit indicated by Steinmetz & White (1997), in order to avoid spurious two body relaxation effects.

In carrying out the calculations presented here, we have used GADGET3, an updated version of the GADGET2 code presented in Springel (2005). The most relevant algorithmic update, in the scope of our non-collisional calculations, resides in GADGET3's newly implemented *domain decomposition* strategy. The new implementation is particularly suited for calculations with very clustered particle distributions, such as the GIMIC spheres, improving the load-balancing of the calculation on high performance computer architectures with a very large number of computational processing units (see Springel *et al.* 2008).

### 5.1.2 Post Processing Pipeline, and Merger Trees construction

With the goal of providing the SAM with high quality inputs, we designed a runtime strategy aiming at a very high time resolution: we saved the status of our system (hereafter a snapshot) on a series of $193$ output times, chosen to be logarithmically evenly spaced in the expansion factor. We identified CDM halos in the high resolution regions using the standard FOF algorithm (Davis *et al.* 1985), as implemented in the GADGET3 code. This algorithm identifies isodensity contours of $\delta \simeq 3/(2\pi b^3)$. We choose the standard value $b = 0.2$ for the linking length parameter, in units of the mean interparticle separation, leading to $\delta \simeq 60$. The FOF algorithm presents some limitations in the way groups of particles are identified: implementing only a geometrical criteria for grouping particles may introduce artifacts in the group detection such as abridging of independent self gravitating groups or spurious identification of small

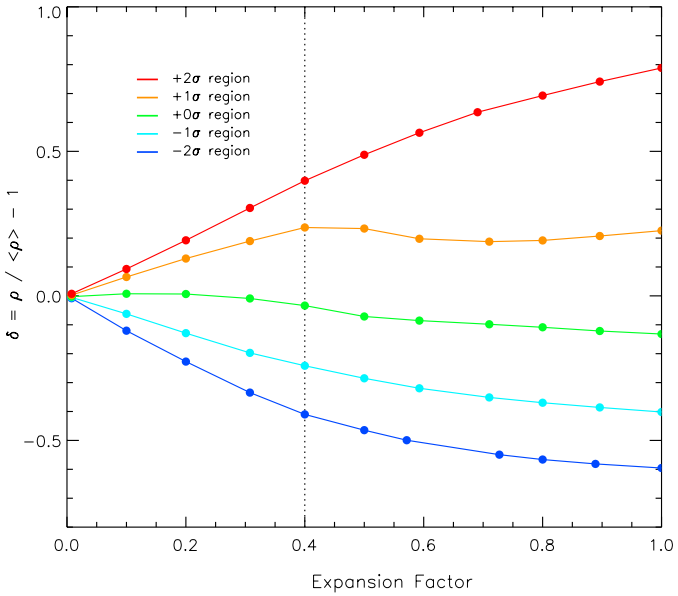


**Figure 5.1:** The overdensity evolution of the five spherical regions at intermediate resolution. The vertical dotted line denotes the epoch at which the regions were selected ($z = 1.5$). Notice the drop, after $z = 1.5$, in overdensity of the $+1\sigma$ region; this results from a massive halo with high peculiar velocity leaving the spherical region. Taken from Crain *et al.* (2009)

groups in the outskirts of much larger ones. Therefore, particle groups identified by the FoF algorithm are geometrically linked but not necessarily gravitationally self-bound. To overcome these limitations and to properly identify DM halos' substructures (DM halos within larger DM halos), we performed a gravitational unbinding procedure, as implemented in the code SUBFIND, inlined in GADGET3 (see Springel *et al.* 2001 for a detailed description of SUBFIND). This code is also able to identify gravitationally bound halos, contained in larger gravitationally bound halos (i.e. *subhalos* or *substructures*). We decided to consider only halos (or subhalos) retaining more than 30 high resolution DM particles, at each time (in each snapshot), this being on the safe side of the standard identification threshold (20 DM particles, as shown also by Knebe *et al.* (2011)).

This post-processing pipeline returned DM halo and subhalo catalogues, for the 5 GIMIC regions. Given the multi-mass particle distribution surrounding the high-resolution region, we discarded halos not exclusively formed by high resolution particles at all times (we discarded halos contaminated by *field* particles).

In the *hierarchical model* of structure formation small DM halos form first and then merge to form larger structures. After identifying DM structures at each time in our simulation, a further step is necessary in order to link corresponding, or merging, ha-

los across our time series of snapshots. This task has been performed using a software suite, namely:

- L-BASETREE: this code actually establishes the links (by means of pointers in complex data structures) between halos identified in different snapshots
- L-HALOTREE: using the catalogues produced by SUBFIND and links identified by L-BaseTree, this code builds the so called *merger trees*. These *trees* are rooted at DM halos (or subhalos) identified in the end-state of each simulation and, going back in time, all the available information on the halo's progenitors are stored in a tree structure.
- additional post-processing:
  L-ADDPOSTAB, L-ADDIDTAB, L-MAKEUNIQUEIDS and
  L-SELECTMAINBRANCHES are accessory post processing tools that modify the initial structure of the halos' *merger trees* in order to allow the SAMs to use them.

A visual impression of a halo merger tree is given in figure 5.2. Following Springel *et al.* (2005), the "first progenitor" of a given halo was simply defined as the most massive of its progenitors. This pointer was meant to efficiently track the *main* branch of a merger tree. This is obtained connecting, starting at $z = 0$, the FoF group under consideration with its most massive progenitor at the immediately preceding available time and iteratively linking all other most massive progenitors, going back in time.

Due to severe version *incompatibilities* between the version of GADGET3 available to us and the suite of post processing tools kindly shared with us by Klaus Dolag, a lot of code implementation work was necessary in order to produce the final version of the merger trees.
We arbitrarily choose to save the simulation outputs in the Hierarchical Data Format (HDF5) enabling an extreme portability of the data among different platforms. This also required a considerable amount of coding.

In Figure 5.3, we show the differential number density of haloes identified with the FoF algorithm, $dn(M)/dM$, multiplied by $M^2$ in order to reduce the dynamic range of the plot, and thus more clearly highlighting the differences between regions. In this

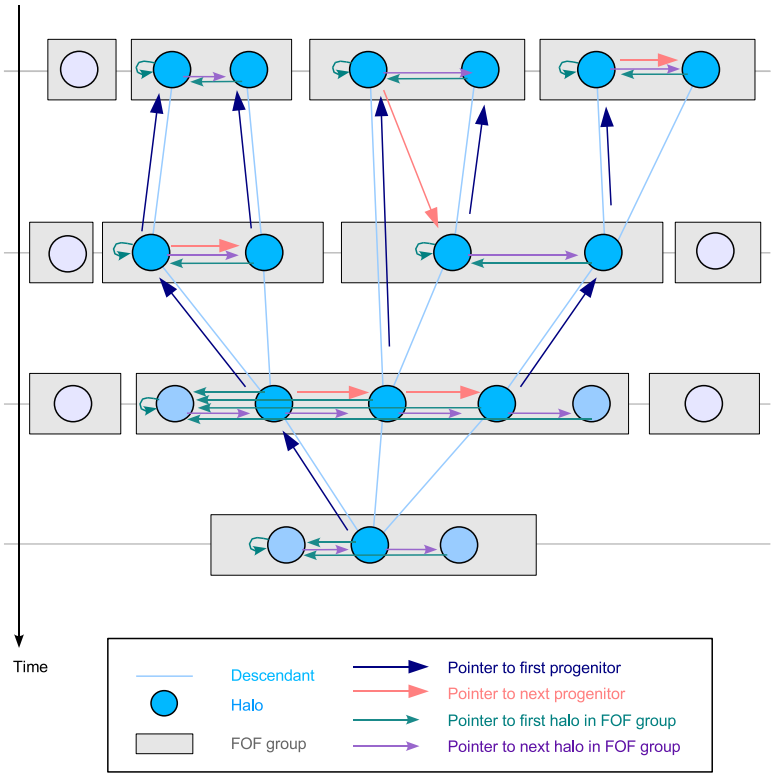


**Figure 5.2:** Schematic organisation of the merger tree in the Millennium Run. At each output time, FOF groups are identified which contain one or several (sub)halos. The merger tree connects these halos. The FOF groups play no direct role, except that the largest halo in a given FOF group is the one which may develop a cooling flow according to the physical model for galaxy formation implemented for the trees. To facilitate the latter, a number of pointers for each halo are defined. Each halo knows its descendant, and its most massive progenitor. Possible further progenitors can be retrieved by following the chain of 'next progenitors'. In a similar fashion, all halos in a given FOF group are linked together. Figure taken from Springel *et al.* 2005

plot, $dn(M)/dM$ is normalized by the total mass contained in each sphere. In this way we also have a measure of the *efficiency* of halo formation per unit mass. Starting from our data, we have reproduced Figure 2 (right panel) in Crain *et al.* (2009) as a validation of our runs. Comparing the two plots, a remarkable agreement is found, with differences due to a different binning in mass. It is worth noticing the original plot in Crain *et al.* (2009) has an incorrect normalization: the authors have erroneously normalized the masses in GADGET *internal* mass units (i.e. $10^{10}$ solar masses). We are using here the same normalization for consistency purposes only.

Following Crain *et al.* (2009) and looking at Figure 5.3, it is possible to appreciate the systematic variation from region to region at all masses. Haloes form more efficiently in the high-density regions because they are the most dynamically advanced and the most massive haloes form only in the most overdense regions.

These results agree with previous numerical and analytical studies of DM halo evolu-

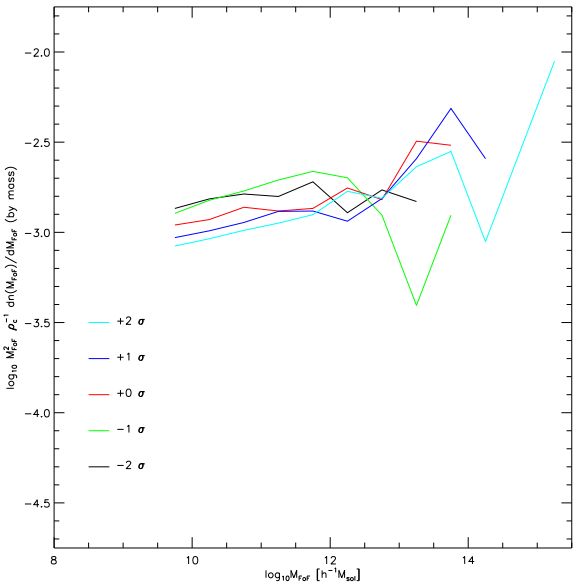


**Figure 5.3:** Differential number density of halos as a function of mass at $z = 0$, normalized by the total enclosed mass of each region and multiplied by $M^2$ to reduce the dynamic range of the plot.

tion (e.g. Frenk *et al.*, 1988; Mo & White, 1996; Sheth & Tormen, 2002).

Frenk *et al.* (1988),Cole (1997) and more recently Sheth & Tormen (2002), have shown that the rate at which a dark matter halo population evolves is fundamentally different between regions of varying overdensity. This has also been shown to be reflected in the clustering bias of haloes as a function of mass by Mo & White (1996).

## 5.2 Semi Analytical Modelling of Galaxy Formation

Starting from the DM halo (and subhalo) *merger trees*, we used the SAM described in De Lucia & Blaizot (2007) and De Lucia *et al.* (2006) to model galaxy formation processes in the different LSS environments simulated. Here we just summarize the main feature of such a model, referring the interested reader to the aforementioned works (and references therein) for a detailed presentation of the model itself.

### 5.2.1 Summary of physical processes included in the model

The SAM employed in this study, includes many relevant physical processes relevant to the production of accurate predictions for the properties of galaxy populations. While

we refer the reader to the detailed discussion available in the aforementioned papers, we give here a short summary:

- **Gas cooling**

  The model estimates the rate of gas cooling following White & Frenk (1991) with an implementation similar to that of Springel *et al.* (2001). The local cooling time is defined as the ratio between the specific thermal energy content of the gas and the cooling rate per unit volume:

  $$t_{\rm cool}(r) = \frac{3}{2}\frac{kT\rho_{\rm g}(r)}{\bar{\mu}m_{\rm p}n_{\rm e}^2(r)\Lambda(T,Z)} \tag{5.2}$$

  where, $\bar{\mu}m_{\rm p}$ is the mean particle mass, $n_{\rm e}(r)$ is the electron density, $k$ is the Boltzmann constant, and $\Lambda(T,Z)$ represents the cooling rate. The latter is strongly dependent on the virial temperature of the halo, and on the metallicity of the gas. In this model, these dependencies are accounted for by using the collisional ionization cooling curves by Sutherland & Dopita (1993). See also Croton *et al.* (2006) and De Lucia *et al.* (2010).

- **Star Formation (SF)** Gas cooled with the aforementioned scheme is modelled to form stars. Assuming the cold gas to be evenly distributed over the galactic disc, a critical mass is defined as

  $$m_{\rm crit} = 3.8\times10^9\left(\frac{V_{\rm vir}}{200\,{\rm km\,s^{-1}}}\right)\left(\frac{r_{\rm disk}}{10\,{\rm kpc}}\right){\rm M}_\odot\ , \tag{5.3}$$

  where the disk is assumed to have a scale length to $r_s = (\lambda/\sqrt{2})R_{\rm vir}$, and the outer disk radius is set to $r_{\rm disk} = 3r_s$, based on the properties of the Milky Way. Here $\lambda$ is the spin parameter of the dark halo in which the galaxy resides, as measured directly from the simulation at each time step. When the cold gas mass in the disk exceeds this critical value, the star formation rate is assumed to be

  $$\dot{m}_* = \alpha_{\rm SF}\left(m_{\rm cold} - m_{\rm crit}\right)t_{\rm dyn,disk}\ , \tag{5.4}$$

  with $\alpha_{\rm SF}$, being the efficiency parameter, typically set so that $5$ to $15$ percent of the gas is converted into stars in a disk dynamical time $t_{\rm dyn,disk}$. SF bursts driven by merger events are also taken into account, along with the resulting feedback contribution also needed to prevent gas-overcooling at early times (White &

Rees (1978); Cole (1991)). For a detailed discussion of the SF model implemented in this code, we refer the interested reader to De Lucia & Blaizot (2007); De Lucia *et al.* (2006); De Lucia, Kauffmann & White (2004); Croton *et al.* (2006)

- **Stellar Populations**

  Galaxy photometric properties are computed by the SAM model using the stellar population synthesis prescriptions from Bruzual & Charlot (2003) and using the method described in De Lucia, Kauffmann & White (2004). The model used for this study, adopts the stellar Initial Mass Function (IMF) introduced by Chabrier (2003) together with the Padova–1994 evolutionary tracks.

- **Feedback mechanisms: AGN, SNe**

  In order to suppress the onset of cooling flows the adopted SAM includes the feedback contribution by Active Galactic Nuclei (AGN) when active in the so called *radio mode*: this is a low–energy feedback scheme that accounts for the accretion of hot gas onto a Super Massive Black Hole (SMBH), once a static hot gas halo has formed around the galaxy hosting the SMBH. As SF proceeds, young massive stars rapidly reach their final evolutive stage and end their life as SNe. Such very energetic events heavily affect the surrounding diffuse gas by the injection of metal polluted hot gas along with a considerable amount of energy that partially reheats cold gas in the galactic disk and can also lead to the ejection of hot gas from the surrounding halo (SNe winds). Details on the inclusion of such properties in the model can be found in De Lucia & Blaizot (2007); Croton *et al.* (2006).

- **Attenuation by Dust**

  Light attenuation operated by dust in the ISM is included in the model: combining both the prescriptions by Devriendt, Guiderdoni & Sadat (1999) (for the homogenous ISM component) and by Charlot & Fall (2000) (for molecular clouds nesting star formation) the implemented model applies the dust correction to the resulting optical depth in the way described by Devriendt, Guiderdoni & Sadat (1999).

In the present study, we try to focus on the LSS environmental effects on galaxy formation, therefore we follow the merger history of SA galaxies forming in different environments. In the hierarchical paradigm of structure formation, large DM halos are formed by merging of smaller objects (that form first): the epoch and the rate of these merging events are expected to depend on the local density. Therefore, also for our samples of galaxies it is important to model the galaxy–galaxy mergers in an accurate way since the resulting galaxy properties might reflect the larger scale evolutionary patterns.

### 5.2.2 Galaxy Mergers

The cosmic merging histories of halos and their substructures is accurately traced by the DM merger trees produced. This allows to safely follow the motion of SAM galaxies lying at the centers of individual halos, with the main limitations imposed by stripping and truncation mechanisms due to tidal forces that lead, as an ultimate fate, to the disruption of the DM subhalo within a larger host DM structure. This happens, in our outputs, when the substructure is depleted of DM particles and falls below the detection threshold for the SUBFIND algorithm (in our case $\simeq 1.95 \times 10^9 M_\odot$). When a substructure is disrupted, the hosted galaxy is assumed to *survive* for a characteristic timescale, determined by dynamical friction, and to continue moving on its current orbit. After this time is elapsed, the *orphan* galaxy is assumed to merge on the central galaxy of her new parent halo. In general, this is the FoF main group halo but it can also be another surviving substructure within it.

When such a *galaxy merger* happens, a *collisional* starburst (Somerville, Primack & Faber 2001) is triggered:

considering two merging galaxies $\mathcal{G}_1$ and $\mathcal{G}_2$ (with $m_1 > m_2$) the SAM model assumes that all the gas from $\mathcal{G}_1$ and $\mathcal{G}_2$ is gathered in the disk component of the remnant galaxy $\mathcal{G}$ while its bulge component results by adding all the stars of $\mathcal{G}_2$ to the bulge stars of $\mathcal{G}_1$. Following also the evolution of the diffuse galactic gas, the model assumes that a fraction of the gas in $\mathcal{G}$ is instantaneously converted into stars, with this fraction depending on the baryonic mass ratio of the two merging galaxies:

$$m_{\rm star}^{\rm new} \;=\; 0.56 \times \left(\frac{m_2}{m_1}\right)^{0.7} \times m_{\rm gas}$$

In the limit of $m_2 << m_1$, no star formation is triggered by the collision, when $m_1 \simeq m_2$ about the $40\%$ of the gas is turned into stars and in the case of a major merger ($m_2/m_1 \geq 0.3$) there is not resulting disc component and all the stars are gathered in the bulge component of galaxy $\mathcal{G}$. This instantaneous burst of star formation, also drives a feedback model in which a fraction of the remaining cold gas is ejected (see also Croton *et al.* 2006).

## 5.3 Preliminary Results

We applied the SAM briefly described in previous section to the halos (and subhalos) merger trees obtained from the GIMIC calculations. At each of our 193 output times, individual galaxy properties were saved and, furthermore, for all galaxies at $z = 0$ we produced the galaxy merger trees (essentially, in the same way we produced DM halos merger trees).

Within the semi–analytical model of galaxy formation used in this study, three main galaxy types are defined:

- **Type0** (T0): these are galaxies that sit at the centre of a self-bound DM halo. All galaxies are born as T0. At each snapshot, T0 galaxies are found at the centers of DM *main* halos and not at the centers of DM halos that have been *accreted* by larger objects.

- **Type1** (T1): galaxies that are sitting at the centre of DM halos that merge onto larger DM halos (thus becoming *substructures* embedded in a larger halo) move from T0 to T1, at what is defined as the *infall* epoch.

- **Type2** (T2): as briefly outlined in the previous section, a DM substructure is progressively disrupted by stripping and truncation mechanisms due to tidal forces within the *parent* halo. When the substructure, hosting a T1 galaxy, falls below the detection threshold of SUBFIND the hosted galaxy becomes of Type2 and its dynamical evolution is followed as previously described.

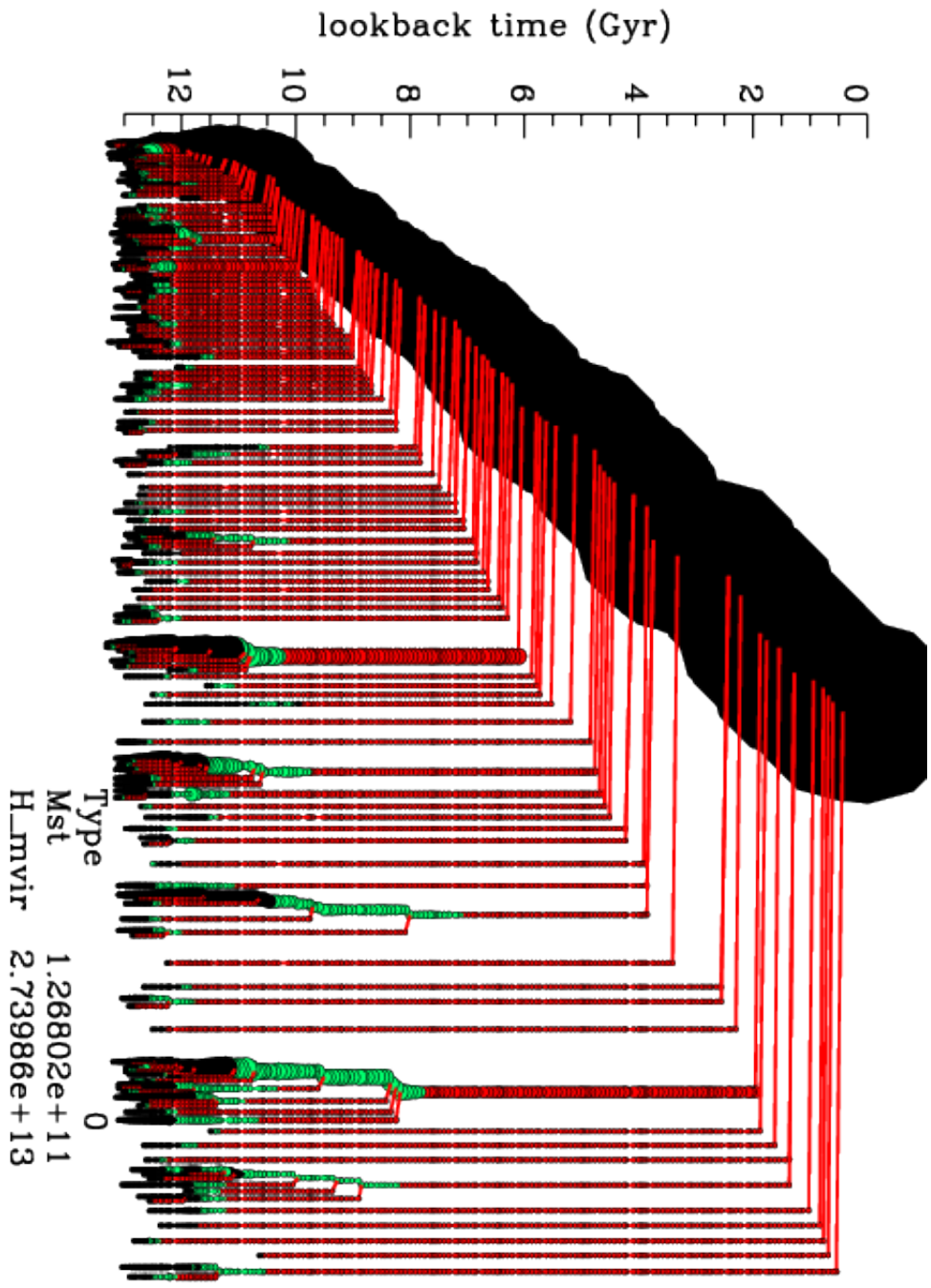


**Figure 5.4:** Galaxy merger tree.
In this example, the merger tree of a Galaxy of Type 0 is shown: at $z = 0$ its stellar content sums up to $\simeq 1.27 \times 10^{11} M_{\odot}$ and this galaxy is central in a DM halo of $\simeq 2.74 \times 10^{13} M_{\odot}$.
Colors: *black* is for T0 galaxies, *green* or T1 and *red* is for T2
Symbols: symbol size is proportional to the stellar content of the represented object.

In Figure 5.4 a visualization of a typical galaxy merger tree is shown. The $z = 0$ galaxy is shown at the top of the plot and all its progenitors, and their merging histories, are plotted going backwards in time recursively. The *main branch* is defined connecting the galaxy, at each epoch, to the progenitor with the largest stellar mass at the immediately preceding epoch (in Figure 5.4 the left-most branch is the *main branch*). In this plot, galaxy merger events are shown as lines, color coded with the Type of the galaxy merging on the main branch.

Following De Lucia & Blaizot (2007), we defined three characteristic epochs for Galaxy evolution:

- **Formation**: this is the epoch when the *total* stellar mass, cumulated on all the progenitors, reaches half the value ($50\%$) of the final stellar mass (at $z = 0$) of the galaxy under consideration
- **Assembly**: this characterizes the epoch in which the *main* progenitor of the galaxy under consideration has formed half ($50\%$) of the final stellar mass (at $z = 0$)
- **Infall**: consistently with the definition of T1 galaxies, this is defined as the epoch in which the DM halo hosting the galaxy under consideration is accreted by a larger halo. This epoch can only be defined for T1 and T2 galaxies (at $z = 0$).

Studying the cumulative distribution functions of these characteristic quantities, as *filtered* from the large scale structure (i.e. in the GIMIC sphere), and depending on the galaxy Types and on their merging histories may shed some light on the effect of different LSS environments on galaxy formation scenarios.

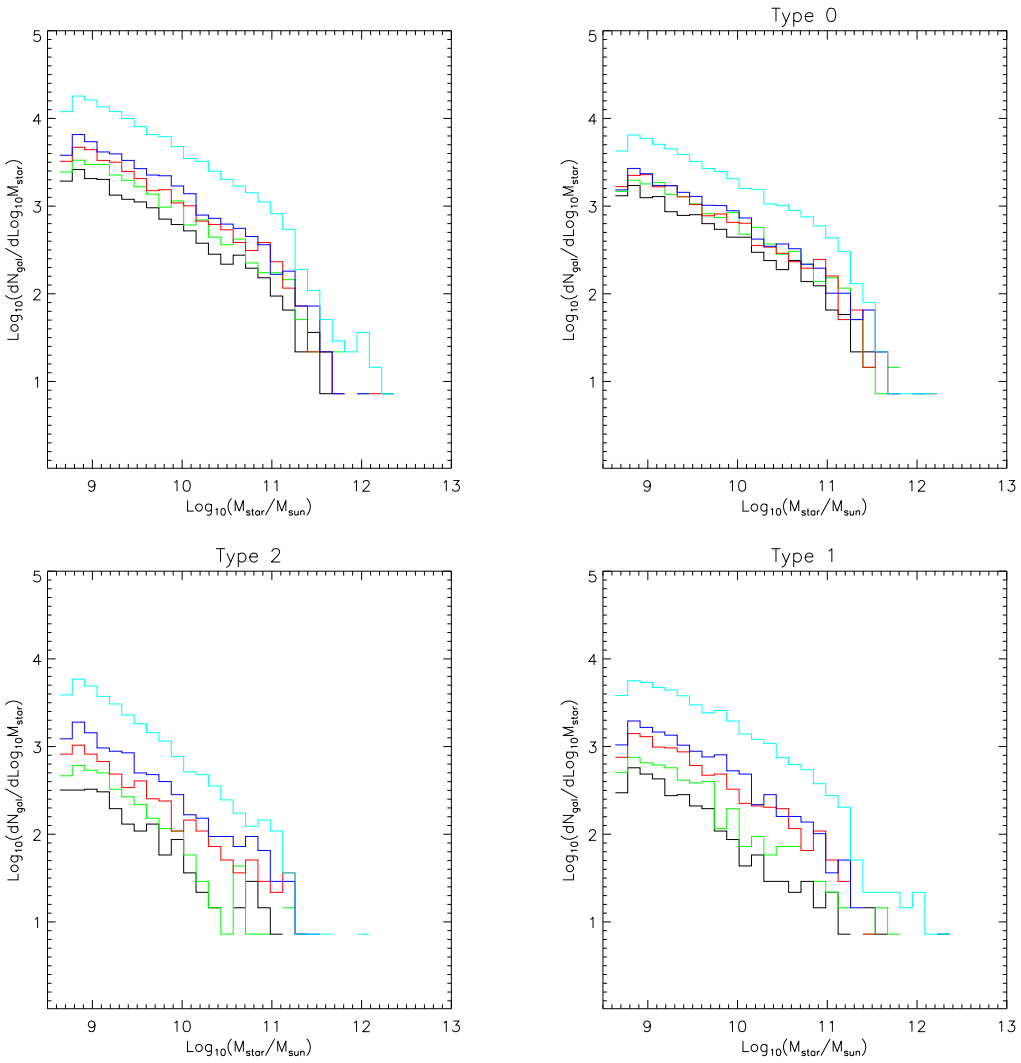


**Figure 5.5:** Stellar mass content differential distribution function at $z = 0$. Clockwise from top left, the overall sample of galaxies containing more than $5 \times 10^8 M_\odot$ in the stellar component, the Type 0, Type1 and Type2 corresponding distributions. Lines are color coded black to cyan for growing overdensities

In Figure 5.5 the differential mass distribution of all galaxies (with $M_{st}^{z=0} \gtrsim 5 \times 10^8 M_\odot$) is shown, color coded for the 5 GIMIC regions (black to cyan for growing overdensities). Given the logarithmic scales in the plot, is straightforward to see how these samples are heavily dominated by low mass galaxies, at $z = 0$. An excess for T1 galaxies in the $+2\sigma$ region at the very high mass end can be observed: in this region, a DM halo of mass $\simeq 2 \times 10^{15} M_\odot$ (one the most massive CDM halos in the MILLENNIUM volume) hosts a population of massive DM substructures, at whose centers are likely to sit massive T1 galaxies. An excess of galaxies with large stellar masses in the overdense regions has also been seen by Crain *et al.* (2009) (see their Figure 3, right panel). They interpret this as a result of the lack of AGN feedback in

their calculations (fully hydrodynamical). Overall the differential mass distributions shown above have a very similar shape, while it is possible to notice a systematic relative offset for the 5 GIMIC regions, for all galaxy types: in higher overdensities a higher number of galaxies of each Type forms across the whole mass range considered. The most massive galaxies preferentially form in the more overdense regions.

In what follows we focus on the stellar content of galaxies, this being the main proxy for overall galactic properties. It is therefore expected to be a sensitive indicator of possible environmental influences on galaxies' formation histories.

The following plots show the "cumulative" distribution functions (hereafter CDFs) of the three characteristic redshifts $z_{Formation}$, $z_{Assembly}$ and $z_{Infall}$ for different samples of our galaxy populations in the 5 GIMIC high resolution regions (usual color coding). The CDFs are normalized on the total number of galaxies in each corresponding sample and defined as:

$$CDF(z) = \frac{\sum_{z_i \geqslant z} dn(z_i)}{N_{TOT}} \tag{5.5}$$

In Figure 5.6, T1 galaxies (at $z = 0$) are shown to have *Infall* redshifts much lower than T2 galaxies (at $z = 0$). This happens by construction in the SAM used for this study: as already outlined in previous sections, after a DM halo (hosting a T0 galaxy) merges onto a larger DM halo (*Infall* epoch) the accreted T0 galaxy becomes a T1 object.

On a timescale driven by tidal stripping and tidal truncation mechanisms in the *parent* DM halo, the accreted DM substrucure hosting a T1 galaxy is disrupted and the hosted T1 galaxy becomes a T2 galaxy, whose evolution is followed by the model as outlined in section 5.2.2. Therefore, a T2 galaxy (at $z = 0$) must have been accreted earlier then a T1 galaxy (at $z = 0$).

Looking at the LSS environmental dependency of *Infall* redshifts in Figure 5.6, it can be noticed how (in particular for T2 galaxies) a clear trend emerges:

T2 galaxies (at $z = 0$) tend to show higher *Infall* redshifts in the overdense regions with respect to underdense ones. This behaviour reflects the hierarchical paradigm of structure formation adopted in this study ($\Lambda$CDM cosmology): structures tend to form earlier in overdense regions, where also the *rate* of merger events is higher than in

underdense regions.

In Figure 5.7, focusing on the *Formation* epoch (i.e. *left* column) it is possible to see that moving from T0 to T1 and to T2 galaxies, the average *Formation* epochs move backwards in time (i.e. at higher $z$). The same behaviour can be observed also for the average *Assembly* epoch (i.e. *right* column).

In the SAM used for this study, star formation processes stop being efficient in T1 galaxies shortly after $z_{Infall}$. Due to *Ram Pressure* stripping by the diffuse hot gas component of the *parent* halo and due to efficient SNe feedback, the newly accreted T1 galaxy is *instantaneously* depleted of its hot gas reservoir. Therefore, star formation within accreted galaxies (T1) is limited to the consumption of the residual gas in the *cold* phase.

Galaxies of Type 1 stop forming stars shortly after $z_{Infall}$, when they have consumed

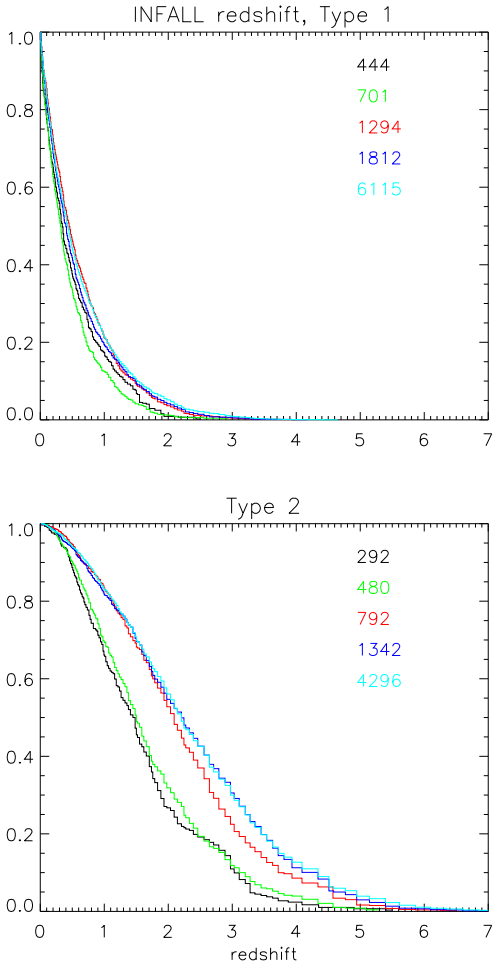


**Figure 5.6:** CDFs for the *Infall* redshift for all T1 and T2 galaxies with $M_{st}^{z=0} \gtrsim 5 \times 10^8 M_{\odot}$ in the 5 GIMIC high resolution regions

their remaining cold gas reservoir. As a consequence, unless a merger event happens, their final stellar mass is almost conserved down to $z = 0$.

In other words, as it can be observed comparing Figure 5.7 with Figure 5.6, T1 and T2

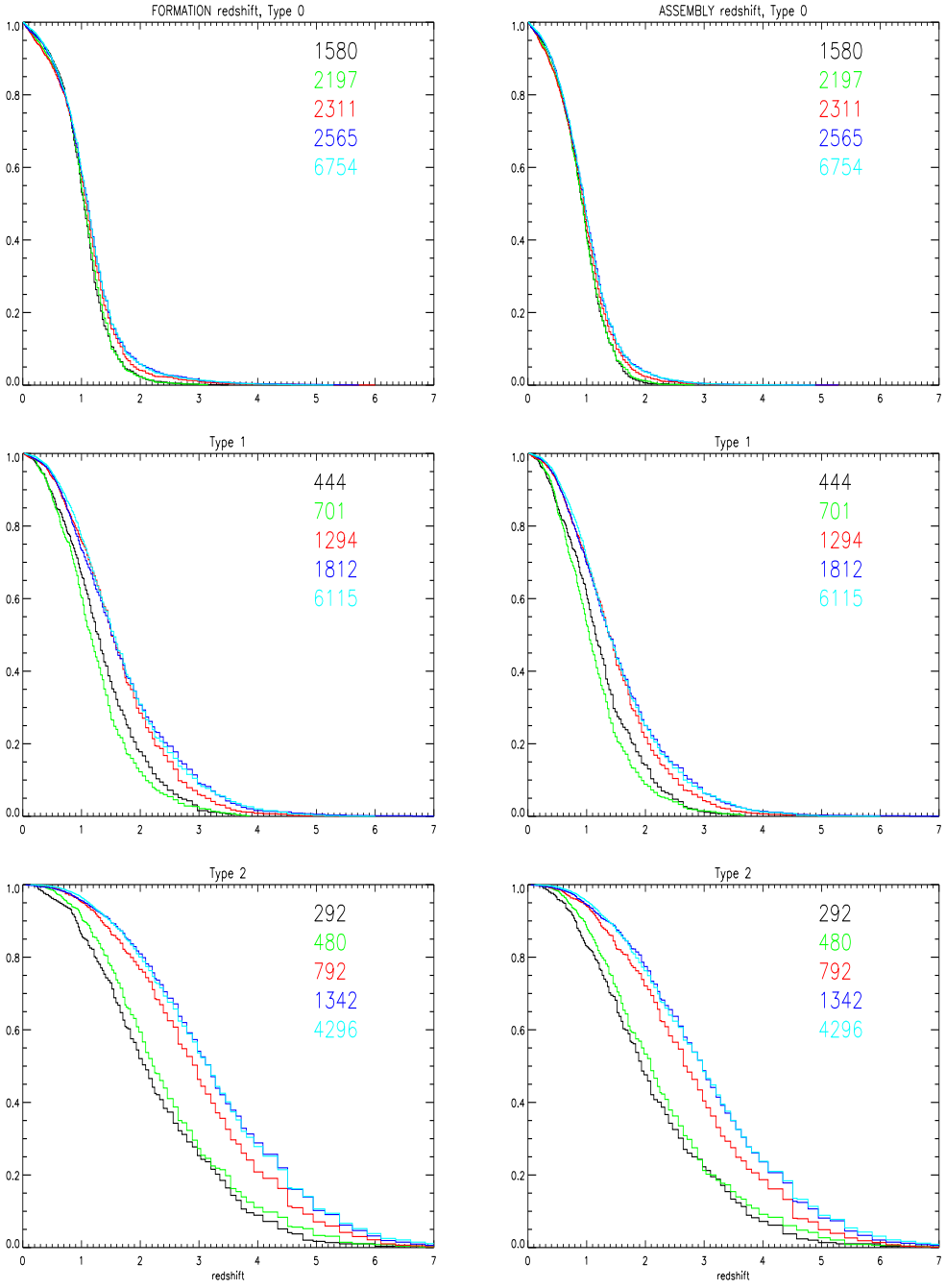


**Figure 5.7:** CDFs for *Formation* (left column) and *Assembly* (right column) redshifts, for the entire galaxy population (i.e. all galaxies with $M_{st}^{z=0} \gtrsim 5 \times 10^8 M_{\odot}$) in each high-resolution GIMIC region, considering the three galaxy types. For each GIMIC sphere, the corresponding number of galaxies is also indicated in the plot. Color coding as in Figure 5.3: *black* to *cyan* growing region overdensity

galaxies tend to have higher $z_{Assembly}$ and $z_{Formation}$ than $z_{Infall}$, by construction.
Always looking at T1 and T2 galaxies in Figure 5.7, it is then clear how the LSS environmental dependency (relative offset of colored lines in each panel) is largely driven by the corresponding dependency in the CDFs for $z_{Infall}$ observed above.
In order to outline the possible residual dependence on the LSS environment, galaxies with equal $z_{Infall}$ will be compared at a further stage.
Moving on to Type 0 galaxies and relatively comparing the two CDFs for $z_{Formation}$ and $z_{Assembly}$, it is possible to appreciate a weak tendency to have $z_{Formation} \gtrsim z_{Assembly}$. This is expected since T0s are expected to have (on average) a richer merging history, compared to T1 and T2 galaxies which exhibit $z_{Formation} \simeq z_{Assembly}$.
The CDFs for T0 galaxies are not dependent on $z_{Infall}$, therefore the observed dependency on the LSS environment is not to be expected *by construction*, with the meaning outlined above. Looking at the overall sample of T0 galaxies in Figure 5.7, a hint can be seen of a small offset between the CDFs of the different galaxy populations belonging to the 5 simulated LSS environments .

In Figure 5.8, in order to investigate the influence of different LSS structure environments, we subsampled the overall population of T0 galaxies in 3 bins for $M_{star}^{z=0}$, as indicated in the Figure.
In this figure it is easier to notice how galaxies in all three mass bins tend to have $z_{Formation} \gtrsim z_{Assembly}$, with a more marked difference for growing masses.
Most interestingly, a clearer dependency on the LSS structure environment can be observed in both the CDFs of $z_{Formation}$ and $z_{Assembly}$ for galaxies belonging to the intermediate and high mass bins: for $z \gtrsim 1$, and in particular for the intermediate mass bin, it is possible to notice a systematic tendency for galaxies belonging to the richest environments to both have higher $z_{Formation}$ and $z_{Assembly}$. It is not straightforward to link this behaviour with the dynamical state of the underlying CDM component (DM halos merger rates).
Focusing on the CDFs of $z_{Formation}$ for central galaxies with $M_{st}^{z=0} \gtrsim 5 \times 10^{10} M_{\odot}$, an overshoot of the CDFs for the overdense environments at $z \lesssim 0.9$ can be appreciated (blue and cyan). This is a hint that, in overdense environments, galaxies in this higher mass bin tend (on average) to be more efficient at forming stars at low redshifts, compared with massive galaxies in underdense regions. A less evident, but still present,

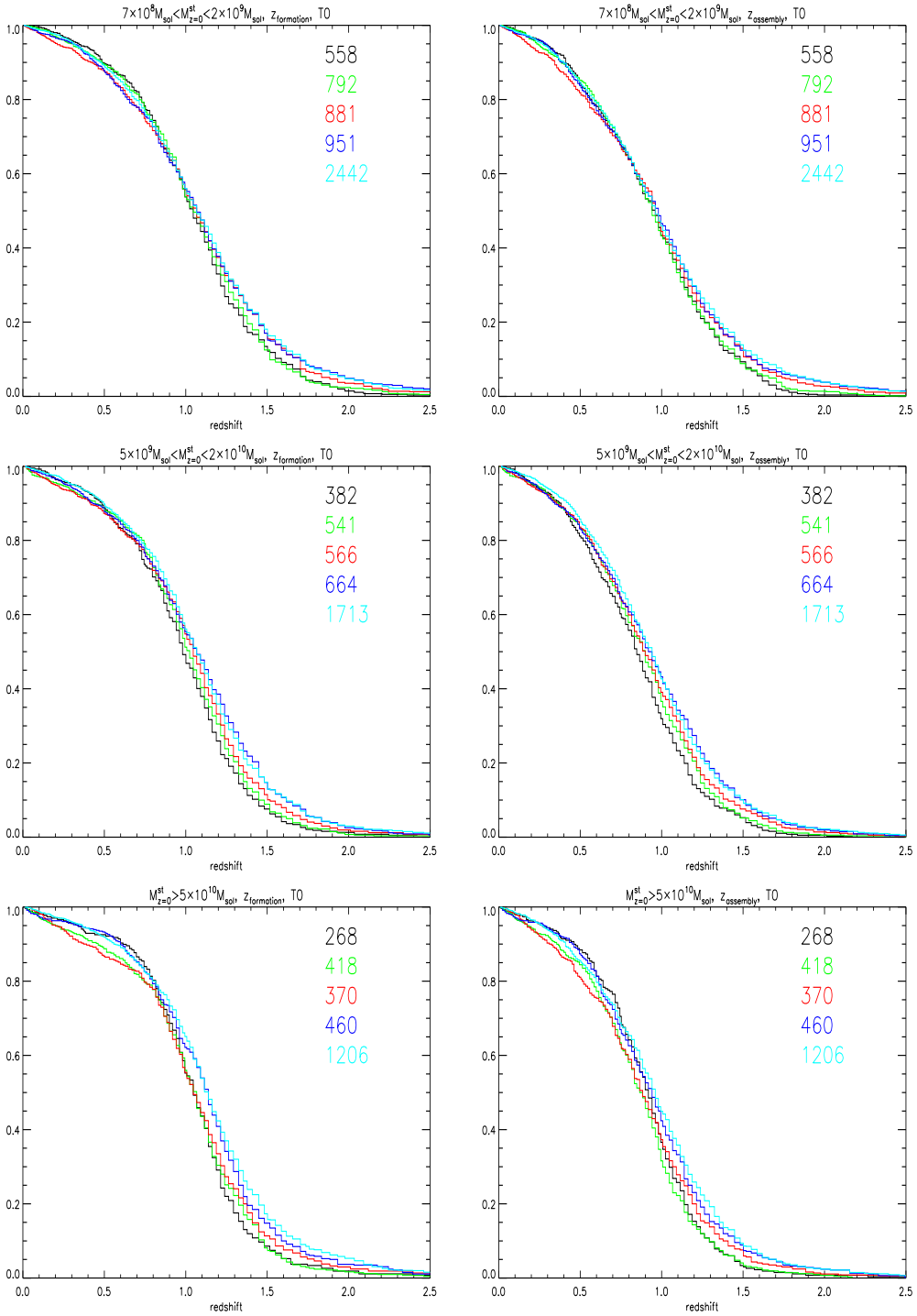


**Figure 5.8:** CDFs for *Formation* (left column) and *Assembly* (right column) redshifts for Type 0 galaxies in the 5 GIMIC regions. Here, the overall sample has been divided in three bins in $M_{st}^{z=0}$, as indicated in each panel. The color coding of the curves goes from black to cyan for growing overdensities. The number of objects in each subsample is also shown.

tendency can also be observed for the corresponding CDFs for $z_{Assembly}$.

## 5.4 Summary and Discussion

Figure 5.5, shows how the galaxy populations are dominated in number by low mass galaxies across all the LSS environments considered. Moreover, an excess of satellite (i.e. Type 1) galaxies at the high mass end in the $\sigma = +2$ volume has also been pointed out: Crain *et al.* (2009) also notice an excess of massive galaxies in the overdense regions and explain it by the lack of AGN feedback in their fully hydrodynamical calculations. The SAM used in this study includes feedback from AGN in the so called *low–energy radio* mode but potentially the same excess of massive galaxies pointed out by Crain *et al.* (2009) is seen. This will be matter of further investigation.

Satellite (i.e. Type 1 and Type 2) galaxies are shown to exhibit a tendency to form and assemble their stellar content at higher redshifts compared to central (i.e. Type 0) galaxies. It has been also shown how this happens by construction in our SAM, being SF processes quenched in satellite galaxies soon after the *Infall* epoch. Satellite galaxies of Type 2 have been accreted by their host CDM halo (at $z = 0$) much earlier then satellite of Type1 galaxies. This, again, happens by construction in the SAM model used for this study, a residual environmental dependency of the *Infall* epochs can be observed. This behaviour reflects the more advanced dynamical state of the underlying CDM structure formation processes in overdense regions (higher merger rates for CDM halos). In such environments, the tendency for CDM *substrucures* (hosting a galaxy) to fall into a larger CDM halo appears earlier in time than in underdense regions thus resulting in the offset in the CDFs for *Infall* epochs we previously pointed out.

Figure 5.8 shows that more massive central (Type 0) galaxies exhibit a clearer tendency to first form their stellar content and then assemble it at a later stage, with respect to lower mass T0 galaxies ($z_{Formation} \simeq z_{Assembly}$). This suggests a tendency for a large fraction of the $z = 0$ content of these central (Type 0) galaxies to be formed by their progenitors at higher redshifts and then assembled in the final object at a later stage. This was already pointed out by De Lucia & Blaizot (2007) to be the case for Bright Central Galaxies (BCGs) located at the center of Galaxy Clusters. Since those objects are very rare in our sample, there are hints that this might also happen for T0 galaxies belonging to Galaxy Groups, but further investigation is required.

Considering central galaxies with $5 \times 10^9 M_\odot \lesssim M_{st}^{z=0} \lesssim 2 \times 10^{10} M_\odot$, a residual dependency could be pointed out on the LSS structure environment on the CDFs of both $z_{Formation}$ and $z_{Assembly}$: in more overdense regions there is a clear tendency for central galaxies to have the 50% of their final stellar mass (at $z = 0$) formed earlier than galaxies located in less dense environments. The same trend is also observed for the *assembly* epochs of the same sample. Given the complex interplay of the physical processes pertaining to cosmic baryons, it is not straightforward to interpret this as a result of the relatively more advanced dynamical state of the underlying CDM structure formation processes in overdense regions, compared to the less dynamically evolved (lower merger rates of CDM halos) ones.

Numerical modelling of the star formation histories (SFH) of galaxies still struggles in reproducing observational data: this is certainly due to the complex interplay of physical mechanisms that can influence the efficiency of a single galaxy in giving birth to stars.

Moreover, it is also possible that physical processes triggered by the environment *beyond* the galaxy borders can influence the local SFH. Current galaxy surveys are designed to detect large number of galaxies, in wide portions of the sky, sampling well defined ranges in cosmic time: as examples consider the SDSS survey that aims at observing all the sky at $z \lesssim 0.3$ or the DEEP2 project that aims at probing a much smaller portion of the sky ($3.5 \ \ deg^2$) but out to $z \lesssim 1.4$ or the forthcoming EUCLID mission which aims at surveying the all sky out to $z \simeq 1$.

In order to link the baryonic properties of different galaxy catalogues in a coherent picture, numerical simulations such as the ones carried out in this study will play a fundamental role in unveiling the nature of the multi-scale phenomena that results in the *zoo* of the observed galactic properties.

# Chapter 6

# Conclusions and future work

The dynamical evolution of the matter content of the universe has been modelled throughout this study as that of Lagrangian fluids, considering both the non-collisional CDM component and the collisional baryonic one. As a numerical tool for carrying out these large and complex calculations we employed GADGET2 (see Springel 2005) and the more recent GADGET3 (see Springel *et al.* 2008): we describe the numerical solvers implemented in the code and test their behaviours in both gravitational and hydrodynamical setups of relevance for cosmological calculations (Tasker *et al.* 2008). We conclude that such a complex numerical tool cannot be properly used without a detailed comprehension of the inherent limits of the algorithmic approach. This is shown to be crucial for obtaining reliable physical results.

We also exploit the so called *Semi–Analytical* approach for the modelling of non–dynamical physical processes of relevance for galaxy formation such as star formation, feedback mechanisms and galaxy mergers, among others. Using the outputs of the MILLENNIUM simulation and the relative semi analytical galaxy catalogues produced by Croton *et al.* (2006), we developed an algorithm aimed at the identification of large spherical underdense regions in the simulated LSS structure, at $z = 0$. Focusing on this peculiar LSS environment, we found a confirmation in numerical simulations of the observations by Trujillo, Carretero & Patiri (2006): the Tidal Torque Theory can predict the distribution of the spatial orientations of both the angular momentum vector of Milky Way size galaxies located on the surface of large spherical *voids*, and of the spatial orientations of their host DM halos.

Targeting galaxy formation processes in a set of different LSS environments, we re–simulated the 5 GIMIC regions (Crain *et al.* 2009) following the gravitational evolution of the CDM component only. We have then applied a Semi Analytical Model of galaxy formation (De Lucia & Blaizot 2007 ) on the CDM halos' *merger trees*, thus obtaining the galaxy catalogues for the 5 different LSS environment simulated. It is not yet well understood if and how the LSS environment can influence the star formation history of galaxies. Starting from the stellar mass content of Semi–Analytical galaxies at $z = 0$, we defined characteristic epochs for the build up of their final stellar mass and, as a preliminary study, investigate how these distributes as function of LSS environment.

## 6.1 Testing hydrodynamical and gravitational solvers in GADGET2

In Chapter 3 we analyzed the behaviour of GADGET2 on a suite of tests

- **Sod**: this standard, purely hydrodynamical, *shock–tube* problem allowed us to contrast GADGET2 results with an analytical solution Sod (1978).
  The code's implementation of the SPH behaves as expected not showing any dependency of the solution on the spatial orientation of the propagating shock front. As an inherent feature within the SPH technique, GADGET2 cannot accurately reproduce sharp shock and contact discontinuities. This effect is shown to depend on the accuracy in sampling the fluid (i.e. on the number of particles) and on the choice of the parametrization for *artificial viscosity*.

- **Sedov**: the *point–like* explosion modelled in this test, allowed an assessment of GADGET2 capabilities in following the propagation, at high Mach number, of a very energetic shock front trough an unpertubed medium. In absence of gravity, we could contrast our results with an analytical solution (Sedov 1959). Using the individual hydrodynamical time stepping scheme commonly employed in cosmological calculation, forced us to apply a very low limit on the time step size in order to recover the analytical expectations. Nevertheless, a *plume* of over ener-

getic particles has been observed at the shock front at all evolutionary stages. As a result we identify and show a limitation of the *gather*-like (in the SPH sense) assignment scheme of the hydrodynamical timestep in GADGET2 and suggested a possible solution. We discussed this issue with GADGET2 developers and contributed to the identification of a *scatter*-like approach which has been shown to improve the results (private communication).

- **King halo** we created a distribution of CDM and SPH particles that resembles a *static* very concentrated ($c = 3$) King profile. The gravitational force trying to collapse the halo is compensated by the SPH hydrodynamical pressure force, therefore our setup is perfectly static. This enabled a verification of the accuracy of both the gravitational (TREE-PM) and the hydrodynamical solvers which are shown to reproduce the expected correct behaviour.

These tests were our contribution to the *code-comparison* project published in Tasker *et al.* (2008). Contrasting Lagrangian with Eulerian techniques, and with analytical solutions, we've shown that particle–based and mesh–based methods reproduce an analytical solution with the same accuracy when they place an equal number of resolution elements in the regions of interest. In light of our results, we also conclude that GADGET2 is definitely a valuable modelling tool, when used with awareness of the internal workings of the code. We also warned GADGET2 users of the production of spurious entropy in energetic shock fronts propagating in a low density homogeneous medium.

## 6.2 Spatial orientation of the angular momentum of halos around cosmic voids

In Chapter 4, we developed an algorithm for the identification of large underdense regions (i.e. *voids*) in the LSS matter distribution (for a validation of this algorithm see Colberg *et al.* 2008). We have shown that, selecting halos on voids' surfaces containing a Milky–Way like disc galaxy at their centres the, angular momentum of the dark matter halo is oriented preferentially parallel to the surface of the voids. Observationally, the same alignment is detected using the baryonic matter (Trujillo, Carretero

& Patiri 2006). These two pieces of information are in agreement with the TTT prediction that both the dark and the baryonic matter component have conjointly acquired their angular momentum before the moment of the turnaround. Interestingly, the signal detected in the real observation c=$0.7^{+0.1}_{-0.2}$ is higher than the one found in the simulations c=$0.151\pm0.046$. This is to be expected taking into account that the signal in the dark matter haloes should be erased by non–linear effects such as exchange of angular momentum between the haloes. This work has been published in a refereed paper (Brunino *et al.* 2007).

Future work, consequently, should explore the strength of the alignment of the haloes at the moment of *turnaround*. At that early epoch the strength of the signal should be as strong as the one measured using the baryonic component. Porciani, Dekel & Hoffman (2002b) show hints that this should be the case by comparing the relation between the halo spin and the linear shear tensor at different redshifts from z=50 to z=0.

## 6.3 GIMIC and SA galaxies

We performed a set of CDM–only cosmological calculations using the GADGET3 code (Springel *et al.* 2008) and following the dynamical evolution of 5 different LSS environments selected in the MILLENNIUM volume as quasi–spherical regions with radius $\simeq 20h^{-1}$ Mpc. This set of simulations is the gravity–only version of a project carried out by the *Virgo Consortium* under the acronym GIMIC (*Galaxies-Intergalactic Medium Interaction Calculation*) and presented in Crain *et al.* (2009).

We saved the status of our systems in a time series of 193 snapshots evenly spaced in the logarithm of the expansion factor.

We identified and extracted the CDM halos and their substructures from the raw snapshot data and organized them in the so called *halo merger trees* by means of the code SUBFIND and of a suite of post–processing tools.

Thanks to the accurate temporal resolution of our outputs and to the high mass resolution in our calculation, the obtained halo merger trees have been provided, as an high quality input, to the SAM by De Lucia & Blaizot (2007). This model follows the formation of galaxies in CDM halos, treating the complex baryonic physics by means of analytical prescriptions.

We then generated and analysed the galaxy catalogues and the relative merging histories, defining three characteristic epochs for galaxy formation:

- *formation*: when 50% of the stellar content of a galaxy at $z = 0$ have been formed (in the galaxy itself, or in its progenitors).
- *assembly*: when 50% of stellar content of a galaxy at $z = 0$ is present in the galaxy itself.
- *infall*: for satellite galaxies, this epoch represents the time when the CDM substructure, in which the galaxy was initially formed, merged onto a larger CDM halo.

As a preliminary study, we showed the Cumulative Distribution Functions (CDFs) of these quantities looking at their LSS potential environmental dependencies.

We observed that satellite galaxies tend to form and assemble their stellar content at higher redshifts compared to central galaxies. We also showed how this happens *by construction* in the SAM employed for this study, being SF processes quenched in satellite galaxies soon after their *Infall* epoch.

We also indicated how more massive central galaxies exhibit a clearer tendency to first form their stellar content and then assemble it at a later stage, with respect to central galaxies of lower mass (which tend to have $z_{Formation} \simeq z_{Assembly}$). This behaviour is to be interpreted as a tendency for a large fraction of the $z = 0$ stellar content of these central massive galaxies to be formed by their progenitors at higher redshifts and then assembled in the final object at a later stage.

Considering central galaxies with $5 \times 10^9 M_\odot \lesssim M_{st}^{z=0} \lesssim 2 \times 10^{10} M_\odot$, we also showed a residual dependency on the LSS structure environment on the CDFs of both $z_{Formation}$ and $z_{Assembly}$: we interpret this as a hint of a clear tendency for central galaxies in overdense regions to have the 50% of their final stellar mass (at $z = 0$) formed (and assembled) earlier then galaxies located in less dense environments.

## 6.4 Possible evolutions

A further, deeper, analysis is needed in order to better quantify and understand the preliminary results presented in Section 5.3 on the influences of the LSS environment on the galaxy formation processes modelled with the Semi-Analitical technique used in this study.

Several steps should be carried out, starting with a comparison of our galaxy catalogues and merger histories with those obtained by De Lucia *et al.* (2006) on the MILLENNIUM simulation. The GIMIC ICs were generated using the same power spectrum (amplitude and phases) as in the MILLENNIUM simulation (up to the its Nyquist Frequancy) so we should be able to compare the effect of our increased numerical resolution almost on a *per-galaxy* basis.A comparison with the results obtained by other SAMs on the MILLENNIUM outputs, will also help in further validating our results.

A comparison of the star formation histories of our Sami-Analytical galaxies with those of the galaxies formed in the original GIMIC hydrodynamical calculations by Crain *et al.* (2009) will also be instructive. Moreover, given the comoving volume of the GIMIC regions, and the mass resolution of our calculation, we should be also able to compare our populations of SA galaxies with those probed by the 2DFGRS (Colless *et al.* 2001) and by the SDSS (York *et al.* 2000).

# Appendices

# Appendix A

# SPH smoothing in GADGET2

As discussed in section 2.2, at the core of the SPH technique there is a smoothing of particles' physical quantities using a *window* or *kernel* function which is commonly denoted as $W(\vec{x}, h)$ (with $\vec{x}$ the particle position and $h$ the smoothing scale). This function, is asked to be normalized such that:

$$W(\vec{x}, h)\mathrm{d}\vec{x} = 1 \tag{A.1}$$

and

$$W(\vec{x}, h) \rightarrow \delta_{Dirac}(\vec{x}) \tag{A.2}$$

for $h \rightarrow 0$. Moreover, it is also necessary to choose this function such as it has a compact support:

$$W(\vec{x}, h) = 0 \tag{A.3}$$

when $|\vec{x}| > h$ such that the discretized equation of hydrodynamics can take the general form (2.32, 2.33, 2.34).

In GADGET2, the SPH kernel function takes the form:

$$W(r,h) = \frac{8}{\pi h^3} \begin{cases} 1 - 6\left(\frac{r}{h}\right)^2 + 6\left(\frac{r}{h}\right)^3 & 0 \leq \frac{r}{h} \leq \frac{1}{2} \\ 2\left(1 - \frac{r}{h}\right)^3 & \frac{1}{2} < \frac{r}{h} \leq 1 \\ 0 & \frac{r}{h} > 1 \end{cases} \tag{A.4}$$

with $r$ being the radial distance from the particle center, and $h$ being the characteristic distance for the kernel function cut-off. It is common to indicate $h$ as the *smoothing*

length: it determines the spherical region that contains all the neighbouring particles that contributes to (or are contributed by) the SPH estimation of physical quantities for the individual particle under consideration.

In GADGET2 implementation of SPH, smoothing lengths are individual to particles and defined such that their kernel volumes contain a constant mass for the estimated density:

$$\frac{4\pi}{3} h_i^3 \rho_i = N_{\rm sph} \overline{m} \tag{A.5}$$

where $N_{\rm sph}$ is the typical number of smoothing neighbours, and $\overline{m}$ is an average particle mass.

# Bibliography


Agertz O., Moore B., Stadel J., Potter D., Miniati F., Read J., Mayer L., Gawryszczak A., Kravtsov A., Nordlund Å., Pearce F., Quilis V., Rudd D., Springel V., Stone J., Tasker E., Teyssier R., Wadsley J., Walder R., 2007. MNRAS, **380**, 963. *Fundamental differences between SPH and grid methods*.

Agustsson I., Brainerd T. G., 2006. ApJ, **644**, L25. *The Orientation of Satellite Galaxies: Evidence of Elongation in the Direction of the Host*.

Altay G., Colberg J. M., Croft R. A. C., 2006. MNRAS, **370**, 1422. *The influence of large-scale structures on halo shapes and alignments*.

Aragon-Calvo M., van de Weygaert R., van der Hulst T., Szalay A., Araya P., 2006. *The Multiscale Morphology Filter*, In: *Bernard's Cosmic Stories: From Primordial Fluctuations to the Birth of Stars and Galaxies*.

Avni Y., Bahcall J. N., 1980. ApJ, **235**, 694. *On the simultaneous analysis of several complete samples - The V/Vmax and Ve/Va variables, with applications to quasars*.

Bagla J. S., Ray S., 2005. MNRAS, **358**, 1076. *Comments on the size of the simulation box in cosmological N-body simulations*.

Bailin J., Steinmetz M., 2005. ApJ, **627**, 647. *Internal and External Alignment of the Shapes and Angular Momenta of $\Lambda$CDM Halos*.

Balsara D. S., 1995. *Journal of Computational Physics*, **121**, 357. *von Neumann stability analysis of smooth particle hydrodynamics–suggestions for optimal algorithms*.

Barnes J., Efstathiou G., 1987. ApJ, **319**, 575. *Angular momentum from tidal torques*.

Barnes J., Hut P., 1986. Nature, **324**, 446. *A hierarchical O(N log N) force-calculation algorithm*.

Basilakos S., Plionis M., Yepes G., Gottlöber S., Turchaninov V., 2006. MNRAS, **365**, 539. *The shape-alignment relation in $\Lambda$ cold dark matter cosmic structures*.

Baugh C. M., 2006. *Reports on Progress in Physics*, **69**, 3101. *A primer on hierarchical galaxy formation: the semi-analytical approach*.

Benz W., 1987. *Applications of Smooth Particle Hydrodynamics (SPH) to astrophysical problems*, In: *Particle Methods in Fluid Dynamics and Plasma Physics*, 97.

Binggeli B., 1982. A&A, **107**, 338. *The shape and orientation of clusters of galaxies*.

Bond J. R., Kofman L., Pogosyan D., 1996. Nature, **380**, 603. *How filaments of galaxies are woven into the cosmic web*.

Bower R. G., Benson A. J., Malbon R., Helly J. C., Frenk C. S., Baugh C. M., Cole S., Lacey C. G., 2006. MNRAS, **370**, 645. *Breaking the hierarchy of galaxy formation*.

Brunino R., Trujillo I., Pearce F. R., Thomas P. A., 2007. MNRAS, **375**, 184. *The orientation of galaxy dark matter haloes around cosmic voids*.

Bruzual G., Charlot S., 2003. MNRAS, **344**, 1000. *Stellar population synthesis at the resolution of 2003*.

Bryan G. L., Norman M. L., 1997. *ArXiv Astrophysics e-prints*. *A Hybrid AMR Application for Cosmology and Astrophysics*.

Catelan P., Theuns T., 1996. MNRAS, **282**, 436. *Evolution of the angular momentum of protogalaxies from tidal torques: Zel'dovich approximation*.

Chabrier G., 2003. PASP, **115**, 763. *Galactic Stellar and Substellar Initial Mass Function*.

Charlot S., Fall S. M., 2000. ApJ, **539**, 718. *A Simple Model for the Absorption of Starlight by Dust in Galaxies*.

Colberg J. M., Pearce F., Foster C., Platen E., Brunino R., Neyrinck M., Basilakos S., Fairall A., Feldman H., Gottlöber S., Hahn O., Hoyle F., Müller V., Nelson L., Plionis M., Porciani C., Shandarin S., Vogeley M. S., van de Weygaert R., 2008. MNRAS, **387**, 933. *The Aspen-Amsterdam void finder comparison project*.

Cole S., Aragon-Salamanca A., Frenk C. S., Navarro J. F., Zepf S. E., 1994. MNRAS, **271**, 781. *A Recipe for Galaxy Formation*.

Cole S., Lacey C. G., Baugh C. M., Frenk C. S., 2000. MNRAS, **319**, 168. *Hierarchical galaxy formation*.

Cole S., 1991. ApJ, **367**, 45. *Modeling galaxy formation in evolving dark matter halos*.

Cole S., 1997. MNRAS, **286**, 38. *Adding Long-Wavelength Power to N-body simulations*.

Colless M., Dalton G., Maddox S., Sutherland W., Norberg P., Cole S., Bland-Hawthorn J., Bridges T., Cannon R., Collins C., Couch W., Cross N., Deeley K., De Propris R., Driver S. P., Efstathiou G., Ellis R. S., Frenk C. S., Glazebrook K., Jackson C., Lahav O., Lewis I., Lumsden S., Madgwick D., Peacock J. A., Peterson B. A., Price I., Seaborne M., Taylor K., 2001. MNRAS, **328**, 1039. *The 2dF Galaxy Redshift Survey: spectra and redshifts*.

Couchman H. M. P., Thomas P. A., Pearce F. R., 1995a. ApJ, **452**, 797. *Hydra: an Adaptive-Mesh Implementation of P 3M-SPH*.

Couchman H. M. P., Thomas P. A., Pearce F. R., 1995b. ApJ, **452**, 797. *Hydra: an Adaptive-Mesh Implementation of P 3M-SPH*.

Crain R. A., Theuns T., Dalla Vecchia C., Eke V. R., Frenk C. S., Jenkins A., Kay S. T., Peacock J. A., Pearce F. R., Schaye J., Springel V., Thomas P. A., White S. D. M., Wiersma R. P. C., 2009. MNRAS, **399**, 1773. *Galaxies-intergalactic medium interaction calculation - I. Galaxy formation as a function of large-scale environment*.

Croft R. A. C., Metzler C. A., 2000. ApJ, **545**, 561. *Weak-Lensing Surveys and the Intrinsic Correlation of Galaxy Ellipticities*.

Croton D. J., Springel V., White S. D. M., De Lucia G., Frenk C. S., Gao L., Jenkins A., Kauffmann G., Navarro J. F., Yoshida N., 2006. MNRAS, **365**, 11. *The many lives of active galactic nuclei: cooling flows, black holes and the luminosities and colours of galaxies*.

Davis M., Efstathiou G., Frenk C. S., White S. D. M., 1985. ApJ, **292**, 371. *The evolution of large-scale structure in a universe dominated by cold dark matter*.

De Lucia G., Blaizot J., 2007. MNRAS, **375**, 2. *The hierarchical formation of the brightest cluster galaxies*.

De Lucia G., Springel V., White S. D. M., Croton D., Kauffmann G., 2006. MNRAS, **366**, 499. *The formation history of elliptical galaxies*.

De Lucia G., Boylan-Kolchin M., Benson A. J., Fontanot F., Monaco P., 2010. MNRAS, **406**, 1533. *A semi-analytic model comparison - gas cooling and galaxy mergers*.

De Lucia G., Kauffmann G., White S. D. M., 2004. MNRAS, **349**, 1101. *Chemical enrichment of the intracluster and intergalactic medium in a hierarchical galaxy formation model*.

Debattista V. P., Sellwood J. A., 1999. ApJ, **513**, L107. *Warped Galaxies from Misaligned Angular Momenta*.

Devriendt J. E. G., Guiderdoni B., Sadat R., 1999. A&A, **350**, 381. *Galaxy modelling. I. Spectral energy distributions from far-UV to sub-mm wavelengths*.

Dolag K., Borgani S., Schindler S., Diaferio A., Bykov A. M., 2008. Space Sci. Rev., **134**, 229. *Simulation Techniques for Cosmological Simulations*.

Doroshkevich A. G., 1970. *Astrofizika*, **6**, 581. *The space structure of perturbations and the origin of rotation of galaxies in the theory of fluctuation.*

Durier F., Dalla Vecchia C., 2012. MNRAS, **419**, 465. *Implementation of feedback in smoothed particle hydrodynamics: towards concordance of methods*.

Fall S. M., Efstathiou G., 1980. MNRAS, **193**, 189. *Formation and rotation of disc galaxies with haloes*.

Faltenbacher A., Gottlöber S., Kerscher M., Müller V., 2002. A&A, **395**, 1. *Correlations in the orientations of galaxy clusters*.

Font A. S., Bower R. G., McCarthy I. G., Benson A. J., Frenk C. S., Helly J. C., Lacey C. G., Baugh C. M., Cole S., 2008. MNRAS, **389**, 1619. *The colours of satellite galaxies in groups and clusters*.

Frenk C. S., White S. D. M., Davis M., Efstathiou G., 1988. ApJ, **327**, 507. *The formation of dark halos in a universe dominated by cold dark matter*.

Frenk C. S., White S. D. M., Bode P., Bond J. R., Bryan G. L., Cen R., Couchman H. M. P., Evrard A. E., Gnedin N., Jenkins A., Khokhlov A. M., Klypin A., Navarro J. F., Norman M. L., Ostriker J. P., Owen J. M., Pearce F. R., Pen U.-L., Steinmetz M., Thomas P. A., Villumsen J. V., Wadsley J. W., Warren M. S., Xu G., Yepes G., 1999. ApJ, **525**, 554. *The Santa Barbara Cluster Comparison Project: A Comparison of Cosmological Hydrodynamics Solutions*.

Fryxell B., Olson K., Ricker P., Timmes F. X., Zingale M., Lamb D. Q., MacNeice P., Rosner R., Truran J. W., Tufo H., 2000. ApJS, **131**, 273. *FLASH: An Adaptive Mesh Hydrodynamics Code for Modeling Astrophysical Thermonuclear Flashes*.

Gelb J. M., Bertschinger E., 1994. ApJ, **436**, 467. *Cold dark matter. 1: The formation of dark halos*.

Gingold R. A., Monaghan J. J., 1983. MNRAS, **204**, 715. *On the fragmentation of differentially rotating clouds*.

Hartley W. G., Gazzola L., Pearce F. R., Kay S. T., Thomas P. A., 2008. MNRAS, **386**, 2015. *Nature versus nurture: the curved spine of the galaxy cluster X-ray luminosity-temperature relation*.

Heavens A., Peacock J., 1988. MNRAS, **232**, 339. *Tidal torques and local density maxima*.

Heavens A., Refregier A., Heymans C., 2000. MNRAS, **319**, 649. *Intrinsic correlation of galaxy shapes: implications for weak lensing measurements*.

Heitmann K., Lukić Z., Fasel P., Habib S., Warren M. S., White M., Ahrens J., Ankeny L., Armstrong R., O'Shea B., Ricker P. M., Springel V., Stadel J., Trac H., 2008. *Computational Science and Discovery*, **1(1)**, 015003. *The cosmic code comparison project*.

Hernquist L., Katz N., 1989. ApJS, **70**, 419. *TREESPH - A unification of SPH with the hierarchical tree method*.

Hernquist L., 1993. ApJ, **404**, 717. *Some cautionary remarks about smoothed particle hydrodynamics*.

Heymans C., White M., Heavens A., Vale C., van Waerbeke L., 2006. MNRAS, **371**, 750. *Potential sources of contamination to weak lensing measurements: constraints from N-body simulations*.

Hirata C. M., Seljak U., 2004. Phys. Rev. D, **70(6)**, 063526. *Intrinsic alignment-lensing interference as a contaminant of cosmic shear*.

Holmberg E., 1969. *Arkiv for Astronomi*, **5**, 305. *A study of physical groups of galaxies*.

Hopkins P. F., Bahcall N. A., Bode P., 2005. ApJ, **618**, 1. *Cluster Alignments and Ellipticities in ΛCDM Cosmology*.

Hoyle F., 1951. *The Origin of the Rotations of the Galaxies*, In: *Problems of Cosmical Aerodynamics*, 195.

Kasun S. F., Evrard A. E., 2005. ApJ, **629**, 781. *Shapes and Alignments of Galaxy Cluster Halos*.

Kauffmann G., White S. D. M., Guiderdoni B., 1993. MNRAS, **264**, 201. *The Formation and Evolution of Galaxies Within Merging Dark Matter Haloes*.

King I. R., 1966. AJ, **71**, 64. *The structure of star clusters. III. Some simple dynamical models*.

Knebe A., Knollmann S. R., Muldrew S. I., Pearce F. R., Aragon-Calvo M. A., Ascasibar Y., Behroozi P. S., Ceverino D., Colombi S., Diemand J., Dolag K., Falck B. L., Fasel P., Gardner J., Gottlöber S., Hsu C.-H., Iannuzzi F., Klypin A., Lukić Z., Maciejewski M., McBride C., Neyrinck M. C., Planelles S., Potter D., Quilis V., Rasera Y., Read J. I., Ricker P. M., Roy F., Springel V., Stadel J., Stinson G., Sutter P. M., Turchaninov V., Tweed D., Yepes G., Zemp M., 2011. MNRAS, **415**, 2293. *Haloes gone MAD: The Halo-Finder Comparison Project*.

Lee J., Pen U.-L., 2000. ApJ, **532**, L5. *Cosmic Shear from Galaxy Spins*.

Lee J., Pen U.-L., 2002. ApJ, **567**, L111. *Detection of Galaxy Spin Alignments in the Point Source Catalog Redshift Survey Shear Field*.

Lee J., Kang X., Jing Y. P., 2005. ApJ, **629**, L5. *The Intrinsic Alignment of Dark Halo Substructures*.

Lee J., 2004. ApJ, **614**, L1. *The Intrinsic Inclination of Galaxies Embedded in Cosmic Sheets and Its Cosmological Implications: An Analytic Calculation*.

Libeskind N. I., Cole S., Frenk C. S., Okamoto T., Jenkins A., 2007. MNRAS, **374**, 16. *Satellite systems around galaxies in hydrodynamic simulations*.

López-Corredoira M., Betancort-Rijo J., Beckman J. E., 2002. A&A, **386**, 169. *Generation of galactic disc warps due to intergalactic accretion flows onto the disc*.

Lucy L. B., 1977. AJ, **82**, 1013. *A numerical approach to the testing of the fission hypothesis*.

Mo H. J., White S. D. M., 1996. MNRAS, **282**, 347. *An analytic model for the spatial clustering of dark matter haloes*.

Monaghan J. J., Lattanzio J. C., 1985. A&A, **149**, 135. *A refined particle method for astrophysical problems*.

Monaghan J. J., 1992. ARA&A, **30**, 543. *Smoothed particle hydrodynamics*.

Monaghan J. J., 1997. *Journal of Computational Physics*, **136**, 298. *SPH and Riemann Solvers*.

Navarro J. F., Abadi M. G., Steinmetz M., 2004. ApJ, **613**, L41. *Tidal Torques and the Orientation of Nearby Disk Galaxies*.

Onuora L. I., Thomas P. A., 2000. MNRAS, **319**, 614. *The alignment of clusters using large-scale simulations*.

O'Shea B. W., Bryan G., Bordner J., Norman M. L., Abel T., Harkness R., Kritsuk A., 2004. *ArXiv Astrophysics e-prints*. *Introducing Enzo, an AMR Cosmology Application*.

Ostriker E. C., Binney J. J., 1989. MNRAS, **237**, 785. *Warped and tilted galactic discs*.

Patiri S. G., Betancort-Rijo J. E., Prada F., Klypin A., Gottlöber S., 2006a. MNRAS, **369**, 335. *Statistics of voids in the two-degree Field Galaxy Redshift Survey*.

Patiri S. G., Cuesta A. J., Prada F., Betancort-Rijo J., Klypin A., 2006b. ApJ, **652**, L75. *The Alignment of Dark Matter Halos with the Cosmic Web*.

Pearce F. R., Couchman H. M. P., 1997. , **2**, 411. *Hydra: a parallel adaptive grid code*.

Peebles P. J. E., 1969. ApJ, **155**, 393. *Origin of the Angular Momentum of Galaxies*.

Porciani C., Dekel A., Hoffman Y., 2002a. MNRAS, **332**, 325. *Testing tidal-torque theory - I. Spin amplitude and direction*.

Porciani C., Dekel A., Hoffman Y., 2002b. MNRAS, **332**, 339. *Testing tidal-torque theory - II. Alignment of inertia and shear and the characteristics of protohaloes*.

Power C., Navarro J. F., Jenkins A., Frenk C. S., White S. D. M., Springel V., Stadel J., Quinn T., 2003. MNRAS, **338**, 14. *The inner structure of $\Lambda$CDM haloes - I. A numerical convergence study*.

Quinn T., Katz N., Stadel J., Lake G., 1997. *ArXiv Astrophysics e-prints*. *Time stepping N-body simulations*.

Sackett P. D., 1999. *The Shape of Dark Matter Halos*, In: *Galaxy Dynamics - A Rutgers Symposium*, 393, ed. D. R. Merritt, M. Valluri, & J. A. Sellwood.

Saitoh T. R., Makino J., 2009. ApJ, **697**, L99. *A Necessary Condition for Individual Time Steps in SPH Simulations*.

Sales L., Lambas D. G., 2004. MNRAS, **348**, 1236. *Anisotropy in the distribution of satellites around primary galaxies in the 2dF Galaxy Redshift Survey: the Holmberg effect*.

Scannapieco C., Wadepuhl M., Parry O. H., Navarro J. F., Jenkins A., Springel V., Teyssier R., Carlson E., Couchman H. M. P., Crain R. A., Dalla Vecchia C., Frenk C. S., Kobayashi C., Monaco P., Murante G., Okamoto T., Quinn T., Schaye J., Stinson G. S., Theuns T., Wadsley J., White S. D. M., Woods R., 2011. *ArXiv e-prints*. *The Aquila comparison Project: The Effects of Feedback and Numerical Methods on Simulations of Galaxy Formation*.

Sedov L. I., 1959. *Similarity and Dimensional Methods in Mechanics*.

Seljak U., Zaldarriaga M., 1996. ApJ, **469**, 437. *A Line-of-Sight Integration Approach to Cosmic Microwave Background Anisotropies*.

Sheth R. K., Tormen G., 2002. MNRAS, **329**, 61. *An excursion set model of hierarchical clustering: ellipsoidal collapse and the moving barrier*.

Sirko E., 2005. ApJ, **634**, 728. *Initial Conditions to Cosmological N-Body Simulations, or, How to Run an Ensemble of Simulations*.

Sod G. A., 1978. *Journal of Computational Physics*, **27**, 1. *A survey of several finite difference methods for systems of nonlinear hyperbolic conservation laws*.

Somerville R. S., Primack J. R., 1999. MNRAS, **310**, 1087. *Semi-analytic modelling of galaxy formation: the local Universe*.

Somerville R. S., Primack J. R., Faber S. M., 2001. MNRAS, **320**, 504. *The nature of high-redshift galaxies*.

Spergel D. N., Verde L., Peiris H. V., Komatsu E., Nolta M. R., Bennett C. L., Halpern M., Hinshaw G., Jarosik N., Kogut A., Limon M., Meyer S. S., Page L., Tucker G. S., Weiland J. L., Wollack E., Wright E. L., 2003. ApJS, **148**, 175. *First-Year Wilkinson Microwave Anisotropy Probe (WMAP) Observations: Determination of Cosmological Parameters*.

Splinter R. J., Melott A. L., Linn A. M., Buck C., Tinker J., 1997. ApJ, **479**, 632. *The Ellipticity and Orientation of Clusters of Galaxies in N-Body Experiments*.

Springel V., Hernquist L., 2002. MNRAS, **333**, 649. *Cosmological smoothed particle hydrodynamics simulations: the entropy equation*.

Springel V., White S. D. M., Tormen G., Kauffmann G., 2001. MNRAS, **328**, 726. *Populating a cluster of galaxies - I. Results at [formmu2]z=0*.

Springel V., White S. D. M., Jenkins A., Frenk C. S., Yoshida N., Gao L., Navarro J., Thacker R., Croton D., Helly J., Peacock J. A., Cole S., Thomas P., Couchman H., Evrard A., Colberg J., Pearce F., 2005. Nature, **435**, 629. *Simulations of the formation, evolution and clustering of galaxies and quasars*.

Springel V., Wang J., Vogelsberger M., Ludlow A., Jenkins A., Helmi A., Navarro J. F., Frenk C. S., White S. D. M., 2008. MNRAS, **391**, 1685. *The Aquarius Project: the subhaloes of galactic haloes*.

Springel V., 2005. MNRAS, **364**, 1105. *The cosmological simulation code GADGET-2*.

Steinmetz M., White S. D. M., 1997. MNRAS, **288**, 545. *Two-body heating in numerical galaxy formation experiments*.

Sugerman B., Summers F. J., Kamionkowski M., 2000. MNRAS, **311**, 762. *Testing linear-theory predictions of galaxy formation*.

Sutherland R. S., Dopita M. A., 1993. ApJS, **88**, 253. *Cooling functions for low-density astrophysical plasmas*.

Tasker E. J., Brunino R., Mitchell N. L., Michielsen D., Hopton S., Pearce F. R., Bryan G. L., Theuns T., 2008. MNRAS, **390**, 1267. *A test suite for quantitative comparison of hydrodynamic codes in astrophysics*.

Theuns T., Leonard A., Efstathiou G., Pearce F. R., Thomas P. A., 1998. MNRAS, **301**, 478. *P^3M-SPH simulations of the Lyalpha forest*.

Thomas P. A., Colberg J. M., Couchman H. M. P., Efstathiou G. P., Frenk C. S., Jenkins A. R., Nelson A. H., Hutchings R. M., Peacock J. A., Pearce F. R., White S. D. M., 1998. MNRAS, **296**, 1061. *The structure of galaxy clusters in various cosmologies*.

Tormen G., Bouchet F. R., White S. D. M., 1997. MNRAS, **286**, 865. *The structure and dynamical evolution of dark matter haloes*.

Trujillo I., Carretero C., Patiri S. G., 2006. ApJ, **640**, L111. *Detection of the Effect of Cosmological Large-Scale Structure on the Orientation of Galaxies*.

van Haarlem M., van de Weygaert R., 1993. ApJ, **418**, 544. *Velocity Fields and Alignments of Clusters in Gravitational Instability Scenarios*.

White S. D. M., Frenk C. S., 1991. ApJ, **379**, 52. *Galaxy formation through hierarchical clustering*.

White S. D. M., Rees M. J., 1978. MNRAS, **183**, 341. *Core condensation in heavy halos - A two-stage theory for galaxy formation and clustering*.

White S. D. M., 1984. ApJ, **286**, 38. *Angular momentum growth in protogalaxies*.

White S. D. M., 1996. *Formation and Evolution of Galaxies*, In: *Cosmology and Large Scale Structure*, 349, ed. R. Schaeffer, J. Silk, M. Spiro, & J. Zinn-Justin.

Yang X., van den Bosch F. C., Mo H. J., Mao S., Kang X., Weinmann S. M., Guo Y., Jing Y. P., 2006. MNRAS, **369**, 1293. *The alignment between the distribution of satellites and the orientation of their central galaxy*.

York D. G., Adelman J., Anderson, Jr. J. E., Anderson S. F., Annis J., Bahcall N. A., Bakken J. A., Barkhouser R., Bastian S., Berman E., Boroski W. N., Bracker S., Briegel C., Briggs J. W., Brinkmann J., Brunner R., Burles S., Carey L., Carr M. A., Castander F. J., Chen B., Colestock P. L., Connolly A. J., Crocker J. H., Csabai I., Czarapata P. C., Davis J. E., Doi M., Dombeck T., Eisenstein D., Ellman N., Elms B. R., Evans M. L., Fan X., Federwitz G. R., Fiscelli L., Friedman S., Frieman J. A., Fukugita M., Gillespie B., Gunn J. E., Gurbani V. K., de Haas E., Haldeman M.,

Harris F. H., Hayes J., Heckman T. M., Hennessy G. S., Hindsley R. B., Holm S., Holmgren D. J., Huang C.-h., Hull C., Husby D., Ichikawa S.-I., Ichikawa T., Ivezić Ž., Kent S., Kim R. S. J., Kinney E., Klaene M., Kleinman A. N., Kleinman S., Knapp G. R., Korienek J., Kron R. G., Kunszt P. Z., Lamb D. Q., Lee B., Leger R. F., Limmongkol S., Lindenmeyer C., Long D. C., Loomis C., Loveday J., Lucinio R., Lupton R. H., MacKinnon B., Mannery E. J., Mantsch P. M., Margon B., McGehee P., McKay T. A., Meiksin A., Merelli A., Monet D. G., Munn J. A., Narayanan V. K., Nash T., Neilsen E., Neswold R., Newberg H. J., Nichol R. C., Nicinski T., Nonino M., Okada N., Okamura S., Ostriker J. P., Owen R., Pauls A. G., Peoples J., Peterson R. L., Petravick D., Pier J. R., Pope A., Pordes R., Prosapio A., Rechenmacher R., Quinn T. R., Richards G. T., Richmond M. W., Rivetta C. H., Rockosi C. M., Ruthmansdorfer K., Sandford D., Schlegel D. J., Schneider D. P., Sekiguchi M., Sergey G., Shimasaku K., Siegmund W. A., Smee S., Smith J. A., Snedden S., Stone R., Stoughton C., Strauss M. A., Stubbs C., SubbaRao M., Szalay A. S., Szapudi I., Szokoly G. P., Thakar A. R., Tremonti C., Tucker D. L., Uomoto A., Vanden Berk D., Vogeley M. S., Waddell P., Wang S.-i., Watanabe M., Weinberg D. H., Yanny B., Yasuda N., SDSS Collaboration, 2000. AJ, **120**, 1579. *The Sloan Digital Sky Survey: Technical Summary*.

Zaritsky D., Smith R., Frenk C. S., White S. D. M., 1997. ApJ, **478**, L53. *Anisotropies in the Distribution of Satellite Galaxies*.

Zentner A. R., Kravtsov A. V., Gnedin O. Y., Klypin A. A., 2005. ApJ, **629**, 219. *The Anisotropic Distribution of Galactic Satellites*.